Examining Changes in Autophagic Flux and Metabolism of Human CLN7-/- Neural Progenitor Cells (NPCs), Derived from Induced Pluripotent Stem Cells (iPSCs)

Rhys Alexander Smith

Master of Science (by Research)

Department of Life Sciences

A thesis submitted in fulfilment of the requirements of Manchester Metropolitan University for the degree of Master of Science (by Research)

2018

Abstract

Neuronal ceroid lipofuscinoses make up the most common group of neurodegenerative diseases amongst children. Classified into 13 distinct variants (CLN1-13), extensive research has been undertaken in the previous decade in order to understand the pathogenesis of the variations of the disease, however, very little is still known about the variant, CLN7. The aim of this project was to utilise existing techniques in neural differentiation in order to deduce any differences in metabolism and autophagic flux between neural progenitor cells and further differentiated CLN7 patient cells compared to those of control. A stepwise neural differentiation protocol was implemented in order to differentiate human induced pluripotent stem cells to NPCs and subsequently neurons. A range of qPCR targets relating to pluripotency, metabolism and inflammation were selected in order to deduce changes in gene expression in both NPCs and iPSCs. Quantitative analysis provided insight and demonstrated a clear metabolic shift toward glycolysis in NPCs of CLN7, whereas controls favoured oxidative phosphorylation, evident by an increase in oxidative stress, a consequence of OXPHOS due to increased ROS production, indicating mitochondrial dysfunction. An upregulation in the inflammatory pathway, NFkB1 was evident, indicating an increase in inflammation in CLN7 NPCs. Western blot analysis provided insight into an impairment of autophagy through accumulation of p62 as well as activation of p70, a downstream target of the mTORC1 pathway. The results obtained during the project provide a new insight into the pathogenesis of the CLN7 and potentially the pathways relating to the disease resulting in neurodegeneration.

Table of Contents

List of Figures

List of Tables

List of Abbreviations

ADP	**Adenosine diphosphate**
ATG	Autophagy-related Gene
BSA	Bovine serum albumin
CcO	Cytochrome c oxidase
cDNA	Complement Deoxyribonucleic acid
CLN7	Ceroid Lipofuscinosis variant 7
CLP	Curvilinear Profiles
CNS	Central nervous system
Ct	Cycle threshold
DMEM	Dulbecco's modified eagle media
EB	Embryoid Body
EBNA1	Epstein-Barr nuclear antigen 1
ECAR	Extracellular acidification rate
ER	Endoplasmic Reticulum
ESCs	Embryonic stem cells
ETC	Electron Transport Chain
EUCOMM	European Conditional Mouse Mutagenesis
FCCP	Carbonyl cyanide-4 (trifluoromethoxy) phenylhydrazone
FPP	Fingerprint Profile
GLUT1	Glucose transporter 1
GROD	Granular Osmiophilic Deposit
HDF	Human dermal fibroblasts
HEK293	Human embryonic kidney 293 cells
hESC	Human embryonic stem cell
hiPSC	Human Induced Pluripotent Stem cells
HK2	Hexokinase 2
HO-1	Heme oxygenase 1
ICC	Immunocytochemistry
IL-1	Interleukin 1
iPSCs	Induced pluripotent stem cells
IVF	In vitro fertilisation
KEAP1	Kelch-like ECH-associated protein 1
KLF4	Kruppel-like factor 4
LAMP1	Lysosomal associated membrane protein 1
LC3-II	Microtubule-associated protein-light chain II
LDHA	Lactate dehydrogenase A
LSD	Lysosomal storage disease
MEFs	Mouse embryonic fibroblasts
mESCs	Mouse embryonic stem cells
MFS	Major facilitator superfamily
miR	microRNA
MnSOD	Manganese Superoxide Dismutase
mRNA	Messenger RNA

mTORC1	Mammalian target of rapamycin complex 1
mTORC2	Mammalian target of rapamycin complex 2
NADH-dehydrogenase	Nicotinamide adenine dinucleotide dehydrogenase
NCL	Neuronal Ceroid Lipofuscinosis
NEM	Neural expansion media
NFκB	Nuclear factor kappa-light-chain-enhancer of activated B cells
NIM	Neural induction media
NMM	Neural maintenance media
NPCs	Neural progenitor cells
NSCs	Neural Stem Cells
OCR	Oxygen Consumption Rate
Oct4	Octamer-binding transcription factor 4
OXPHOS	Oxidative phosphorylation
PBS	Phosphate buffered saline
PB1	Phox and Bem1 domain
PEP	Phosphoenolpyruvate
PFA	Paraformaldehyde
PI3K	Phosphoinositide 3-kinase related kinase family
PKM1	Pyruvate kinase isozyme 1
PKM2	Pyruvate kinase isozyme 2
PPT1	Palmitoyl protein thioesterase
qPCR	Quantitative polymerase chain reaction
RLP	Rectilinear profiles
ROS	Reactive oxygen species
RT-PCR	Reverse-Transcriptase polymerase chain reaction
P62/SQSTM1	Protein 62, sequesterome
SEM	Standard error of mean
SIRT1	Sirtulin 1
SOX2	SRY-box 2
TNFα	Tumour necrosis factor alpha
TRAF6	TNF receptor associated factor 6
UCP2	Uncoupling protein 2
ULK1/2	Unc-51 like autophagy activating kinase
ZZ	Zinc finger
2DG	2-Deoxy-glucose

1.0 Introduction

1.1 Neuronal Ceroid Lipofuscinosis

The Neuronal Ceroid Lipofuscinoses (NCLs), commonly referred to as Batten Disease, are classified as lysosomal storage disorders (LSDs) and constitute the most common autosomally recessive group of inherited neurodegenerative disorders among children (Cárcel-Trullols, Kovács and Pearce, 2015), with current estimates suggesting an incidence of 1-4 in 100,000 live births worldwide (Rakheja and Bennett, 2018). Current research has demonstrated mutations in distinct genes, CLN1-8 and CLN9-14. Of these various associated proteins, most of them have been localised within lysosomes (CLN1, CLN2, CLN3, CLN5, CLN7, CLN10, CLN12 and CLN13), however CLN6 and CLN8 have been established to localise within the Endoplasmic reticulum, whilst it has been proposed CLN3, CLN7 and CLN12 are lysosomal transmembrane proteins (Kollmann *et al.*, 2013) (see table 1).

Table 1: Comprehensive list of varying NCL disorders, related protein, subcellular localisation and their function (Cárcel-Trullols, Kovács and Pearce, 2015).

NCL	Chromosome	Protein	Subcellular localisation	Function
CLN1	1p32	Palmitoyl protein thioesterase 1 (PPT1), soluble protein composed of 306 amino acids.	Lysosomal matrix, Endoplasmic reticulum, extralysosomal vesicles and presynaptic areas within neurons.	Associated to endo and exocytosis in recycling of synaptic vesicles. Also has role during apoptosis.
CLN2	11p15	TPP1	Endoplasmic reticulum and lysosomal matrix.	Linked to macroautophagy, endocytosis and TNF-α-induced apoptosis.
CLN3	16p12	Lysosomal transmembrane protein	Endosomal/lysosomal membrane	Unknown.
CLN4	20q13.33	Cysteine string protein	Cytosolic, associated to synaptic vesicles in neurons, vesicular membranes and secretory granules in exo/endo/neurocrine cells.	Function is fully rescued by α-synuclein, involved in presynaptic endo and exocytosis.
CLN5	13q22	Soluble lysosomal protein	Matrix of the lysosome.	Unknown

CLN6	15q21	Transmembrane protein of ER	Endoplasmic reticulum membrane.	Unknown.
CLN7	**4q28**	***MFSD8,* lysosomal membrane protein**	**Lysosomal membrane.**	**Unknown.**
CLN8	8q23	Transmembrane protein of ER	Endoplasmic reticulum/ER-Golgi intermediate compartment membrane.	Unknown.
CLN9		Unknown protein	Currently unknown.	Unknown.
CLN10	11p15	Cathepsin D	Lysosomal matrix and extracellular.	
CLN11		Progranulin/Proepithelin/ Acrogranin	Extracellular.	Unknown.
CLN12		ATPase13A2/KRPPD/PARK9/ HSA9947/RP-37C10.4	Lysosomal membrane and multivesicular bodies.	Unknown.
CLN13		Cathepsin F	Matrix of the lysosome.	Unknown
CLN14		Potassium channel tetramerization domain-containing protein 7 (KCTD7)	Cytosolic and also partially associated to the plasma membrane.	Unknown.

Prior to the improvement of genetic technologies and thus the discovery of the NCL associated causative genes, NCL disorders were classified vis-à-vis age of onset and ultrastructural abnormalities.

NCLs are defined as lysosomal storage disorders (LSDs), with the accumulation of this material attributed to impaired autophagy (Getty and Pearce, 2011). The storage material has been analysed immunohistochemically, in which a few extremely hydrophobic proteins were detected within the storage material consisting of subunit c of mitochondrial ATP synthase or sphingolipid activator proteins A and D (Kousi *et al.*, 2009) (Rakheja and Bennett, 2018). This storage material accumulates in lysosomes within the cytosol of neurons as well as non-neuronal cells such as skin adnexal epithelial cells and endothelial cells, characterised by a heterogenous origin (Cárcel-Trullols, Kovács and Pearce, 2015) . Commonly, this accumulated material is autofluorescent and is positive for; Luxol fast blue (stains lipoproteins in the myelin sheath), periodic acid-Schiff (stains

polysaccharides, glycoproteins and glycolipids), Ziehl-Neelsen acid-fast stain (stains mycolic acids) and Sudan black (stains neutral triglycerides and lipoproteins) (Cárcel-Trullols, Kovács and Pearce, 2015). It has been hypothesised that the accumulation mechanistic nature of the ceroid lipopigments in NCLs may be the result of an ancillary process, yet this would not elucidate the nature and functions of the NCL-causing gene products (Geraets *et al.*, 2016) (Cárcel-Trullols, Kovács and Pearce, 2015).

Ultrastructural analysis has been a key feature in the diagnostic procedure for NCL affected patients. It has been apparent that the accumulated storage inclusions occur not only in the central nervous system (CNS), but also within the peripheral nervous system. Indeed, it has been shown that the accumulation occurs within; Schwann cells, fibroblasts, conjunctival epithelial cells, smooth muscle cells, skeletal muscle cells, endothelial cells, trophoblastic cells, peripheral blood lymphocytes and eccrine sweat gland epithelial cells (Rakheja and Bennett, 2018). The inclusions within the two latter cell types are especially poignant as they allow for the least invasive procedure in order to carry out ultrastructural examination. The presence of storage material in trophoblasts has allowed for prenatal diagnosis within the first trimester of biopsies from chorionic villi. When observed using transmission electron microscopy, this storage material is observed as cytosomes – cytoplasmic storage bodies which may be membrane-enclosed, implicating lysosomal storage (Anderson *et al.*, 2006). The implication of lysosomal storage has been enforced by the activity of lysosomal acid phosphatase with the associated storage material.

Four ultrastructural morphological patterns correlate with the various types of NCL disorders, including; granular osmiophilic deposits (GRODs) relating to INCL, curvilinear profiles (CLPs) relating to LINCL, fingerprint profiles (FPPs) relating to JNCL and finally rectilinear profiles (RLPs) (Aberg *et al.*, 1998). Biochemical analysis has been performed on each of these morphological patterns, the results show that GRODs are associated with an accumulation of sphingolipid activator proteins A or saposins A, whereas CLPs, FPPs and RLPs are all associated with an accumulation of subunit C of mitochondrial ATP synthase (Rakheja and Bennett, 2018). It has been established that GRODs are homogenous, membrane-enclosed or finely granular rounded bodies, measuring up to 0.5 microns in diameter and often form aggregates that measure up to 5 microns in diameter (Bennett and Rakheja, 2013). CLPs are membrane-enclosed and have the appearance of C- or S-shaped dark and light alternating lines that exist electron densely, freely within the

cytoplasmic matrix, measuring 1.9-2.4nm in thickness. FPPs are bound, compact, usually membrane-enclosed, stacks of paired parallel dark lines, often resembling fingerprints. It has been shown that each pair of these dark line's measures approximately 7.6-9.6nm in thickness, with each adjacent pair separated by a distance of 3-4nm. Each dark line within these pairs are separated from one another by a lucent zone of 1-3nm (Anderson *et al.*, 2006). RLPs are generally stacks alternating light and dark lines measuring 2.8-3.8nm in thickness. It has been noted that mixed patterns of FPPs with CLPs or RLPs can occur within the same cytosome (Rakheja and Bennett, 2018). Each variant of neuronal ceroid lipofuscinosis produces a distinct morphological abnormality, with several variants displaying overlapping abnormalities (see table 2) and plays a role in determination of NCL variant along with genetic testing (Bennett and Rakheja, 2013).

Table 2: Table 2: The Ultrastructural morphological abnormalities of storage material in the different NCL variants (Rakheja and Bennett, 2018)

Ultrastructural Abnormality	NCL Variant
Rectilinear profiles (RLP)	**CLN5, CLN6, CLN7**
Curvilinear Profiles (CLP)	**CLN2, CLN5, CLN6, CLN7, CLN8, CLN9**
Fingerprint Profile (FPP)	**CLN3, CLN4A, CLN5, CLN6, CLN7, CLN9**
Granular Osmiophilic Deposit (GROD)	**CLN1, CLN4B, CLN9, CLN10**

Presently, no cure has been developed for any variant of the NCLs, with current therapies aimed at improvement in quality of life for patients rather than viable treatment. Enzyme replacement therapy whereby a recombinant human tripeptidyl peptidase-1 cerliponase alpha (Brineura®) has been approved in CLN2 patients who have reached the ages of three years old and older by the Food and Drug Administration in the USA (Geraets *et al.*, 2016). This treatment has also been approved for CLN2 patients of all ages by the European Union. Other than this experimental therapy, drugs that dissipate symptoms such as epileptic seizures and mental health disorder are readily available, providing an insight into the importance in the understanding of the disease and progression of viable therapies (Geraets *et al.*, 2016).

1.2 CLN7 Disease

CLN7 disease is an autosomally recessive neurodegenerative disorder with onset during late infancy, caused by a mutation in the *MFSD8* gene (Kousi *et al.*, 2009). The *MFSD8* gene encodes for a polytopic lysosomal membrane glycoprotein, CLN7, of unknown function, in which patients of variant infantile neuronal ceroid lipofuscinosis are deficient (Sharifi *et al.*, 2010). CLN7 disease begins to exhibit symptoms of mental and motor regression, seizures, ataxia and myoclonus, which lead to premature death within the first two decades of life, with patients becoming symptomatic between the ages of 1.5 and 5 years old (Kousi *et al.*, 2009). Various independent studies using methods such as proteomic analysis of purified human and rat tritosomes, immunoblotting of mouse liver tritosomes and co-localisation studies in hippocampal neurons have been performed to show the localisation of the endogenous protein, with several independent studies showing the glycoprotein localises in lysosomal membranes (Sharifi *et al.*, 2010).

CLN7 is relatively unknown but has been shown to share sequence homologies with the drug: H^+ antiporter family DHA1 of the major facilitator superfamily (MFS) of transporter proteins (Danyukova *et al.*, 2018)(Sharifi *et al.*, 2010). MFS transporters are the largest superfamily of secondary transporters found within the biosphere. They have been found to be distributed ubiquitously throughout almost all organismal phyla in current research (Quistgaard *et al.*, 2016). The presence of these transporters has been found within bacteria, playing a vital role in the uptake of nutrients and removal of damaging compounds. Human models of MFS transporters demonstrate similar functions to those found in bacteria, such as nutrient absorption within the gastrointestinal tract and clearance of deleterious products within the renal and hepatic systems (Quistgaard *et al.*, 2016). This suggests that MFS transporters are evolutionary conserved throughout most currently recognised life-forms, from single cell organisms to complex biological systems found in humans. However, there have been evolutionary features found in human superfamily transporters unseen in other organisms that aid in the transport of nutrients, metabolites, signalling molecules and interactions of substrates between cells and between intracellular substrates (Saier *et al.*, 1999). These additional features within humans have led to their implications in the mechanisms of diseases such as cancer and metabolic disorders; thus, leading to MFS transporters becoming potential targets for future drug therapies. Within current literature there are three recognised variants of MFS transporters including; uniporters, symporters and antiporters. Uniporters are

unique in the fact they require no external energy; however, they can only transport single substrates, which are generally transported down their concentration gradient (Quistgaard *et al.*, 2016). Symporters are able to transport ion coupled substrates across a membrane in a single direction, whereas antiporters are able to sequentially transport two different substrates across a membrane in opposing directions. Symporters and antiporters are diametrically opposed to uniporters as they are able to utilize the energy stored within the concentration gradient of their ion coupled substrate and co-substrate, respectively, allowing for the transport of substrates against their concentration gradients (Quistgaard *et al.*, 2016).

RT-PCR has shown that *Mfsd8* mRNA had a 12 and 6.4-fold change in abundancy in neurons than in astrocytes and microglial cells respectively, during analysis of rat cultures. It was found that *Mfsd8* transcripts were more abundant in the hippocampus than in the cortex and midbrain by a factor of 2.4 and 5 times respectively, within the same study (Cárcel-Trullols, Kovács and Pearce, 2015). It has been shown through extensive biochemical studies that CLN7 colocalises with various lysosomal markers. Siintola et al. proved in transfected COS-1 cells, that HA-tagged wild type and mutant CLN7 colocalises with the Lysosomal-associated membrane protein 1 (LAMP1) (Siintola *et al.*, 2007). The results of this study were reinforced by the work of Shariffi et al. as it was shown that endogenously expressed CLN7 and LAMP1 colocalised within the hippocampal neurons of mice (Sharifi *et al.*, 2010). In CLN7 disease, 30 or more missense, nonsense and frameshift mutations in the *MFSD8* gene have been identified which result in a relative uniform manifestation of variant late-infantile NCL, with only two exceptions. The nature of these mutations has been discussed at length, however the NCL phenotype resulting from the various mutations has been associated with a complete loss in function of the CLN7 protein (Mohammed *et al.*, 2017). An extensive study by Brandenstein et al. showed that a deletion of *Cln7/Mfsd8* exon 2 leads to a complete loss of the CLN7 encoded glycoprotein.

An in vivo study was undertaken in which *Cln7* KO mice, carrying the European Conditional Mouse Mutagenesis (EUCOMM) *tm1d* allele were generated via Cre-mediated recombination of the floxed exon 2 of the murine *Cln7/Mfsd8* gene (Brandenstein *et al.*, 2016). Genotyping the homozygous *Cln7* KO mice and validation of

the loss of exon 2 was carried out, with both triplex polymerase chain reaction (PCR) and quantitative real-time PCR establishing the absence of exon 2 within the *Cln7* KO mice. Sequence analysis of cDNA derived from the brain, kidney and liver of the *Cln7* KO mice revealed that a loss of exon 2 culminated in the complete loss of nucleotides 67-115 in the coding sequence of the *Cln7* mRNA (Brandenstein *et al.*, 2016).

The mammalian target of rapamycin 1 pathway, mTORC1, is known to regulate cell metabolism in response to amino acid stimuli. A study by Danyukova et al. sought out to show whether the loss of Cln7 in KO mice leads to an inactivation/activation of the mTORC1 pathway (Danyukova *et al.*, 2018). The phosphorylation downstream target of mTORC1, S6 ribosomal protein (hereafter referred to as S6) was monitored in response to protracted starvation conditions in wild-type and Cln7 KO MEFs (Danyukova *et al.*, 2018) (Xiao *et al.*, 2009). It was found that both cell types exhibited similar responses to starvation, with complete inhibition of S6 observed at 2h followed by recovery of S6 phosphorylation occurring at 4h with gradual increase following. However, it was found that at time points of 8h and 12h the levels of phosphorylated S6 was markedly decreased in Cln7 KO MEFs in comparison to their wild-type counterparts, indicating impairment of mTORC1 activation during extended starvation (Danyukova *et al.*, 2018). The same study found that loss of Cln7 did not affect autophagic flux. Both Cln7 KO MEFs and their wildtype counterparts were exposed to bafilomycin A1, an inhibitor of lysosomal acidification and thus lysosomal degradation of cellular products. Western blot analysis of both LC3-II and p62 demonstrated comparable levels of both autophagic markers in both cell types (Danyukova *et al.*, 2018).

1.3 Induced Pluripotent Stem Cells (iPSCs)

The term 'stem cells' encompasses a subset of cells that possess the ability of self-renewal, referring to the cells ability to perform multiple divisions whilst able to maintain an undifferentiated state, whilst also possessing the capability to differentiate along different cell lineages (Drozd *et al.*, 2015). Stem cells are generally categorised into two main groups based on their capacity for self-renewal and plasticity (often referred to as the cells potency); "embryonic stem cells" and "non-embryonic stem cells"- also referred to as adult/somatic stem cells (Menon *et al.*, 2016). Before the introduction of induced pluripotent stem cells, embryonic stem cells (ESCs) were studied intensively for their ability to differentiate into any cell type in the body. ESCs extracted from the early embryos of mice (mESCs), were the first cell type isolated which displayed pluripotent properties. In 1981, Evans and Kaufman and Gail R. Martin, independently described the first successful formation of mESCs cultures deriving from mouse blastocysts, as reviewed by Menon et al in 2016. (Menon *et al.*, 2016). In 1998, Thomson and his colleagues progressed with their research into ESCs and successfully cultured human ESCs from blastocysts of human embryos, produced via *in vitro* fertilisation (IVF) as reviewed by Malik and Rao in 2013. (Malik and Rao, 2013).

ESCs possess the unique characteristic of self-renewal, the ability to perpetually divide, whilst continuing to maintain an undifferentiated state, however they retain the capacity to differentiate into all three germ layers (ectoderm, mesoderm and endoderm), with this ability termed as totipotent (Sridharan and Plath, 2008). Following fertilisation, totipotent cells mature into pluripotent cells, more specialised cells that maintain the ability to self-renew and differentiate into all germ layers down various cell lineages (figure 1). The pluripotent cells are responsible for tissue repair, growth and maintenance (Hu, 2014).

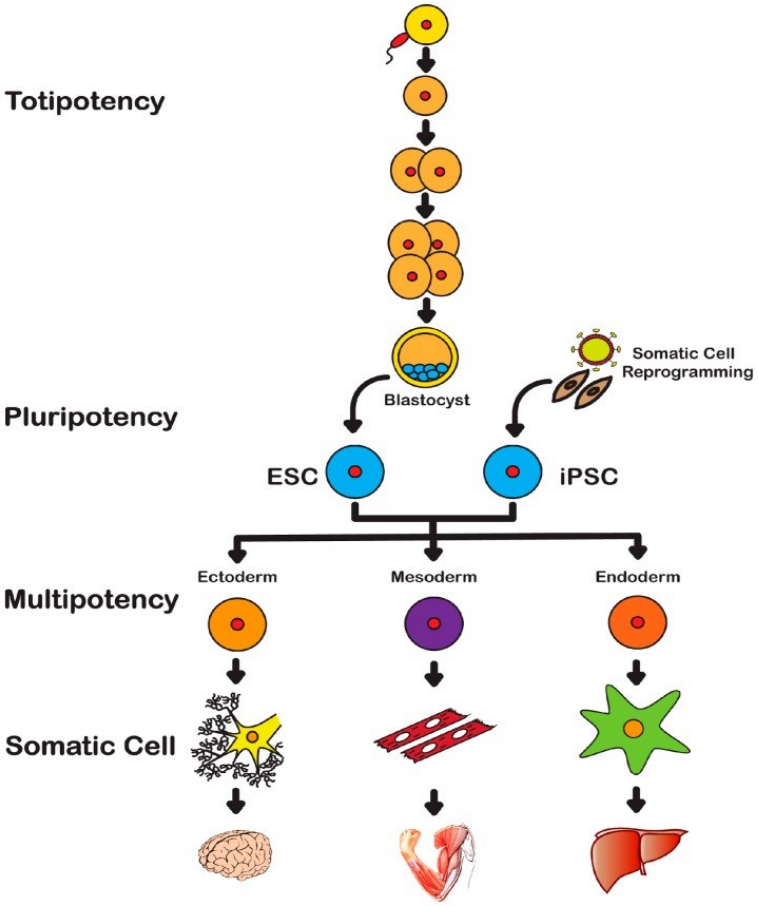

Figure 1: Cell fate of pluripotent stem cells

Figure 1: Following successful fertilisation, ESCs enter a totipotent state, retaining the ability to develop all three germ layers along with cells of the placenta and embryonic tissues. Pluripotent cells maintain self-renewal and are able to differentiate through to the three germ layers and thus various cell lineages. These cells are more specialised within the blastocyst stage. Prior to differentiation into somatic cell types, multipotent cells are undifferentiated and found within postnatal tissues with a limited ability for self-renewal and are committed in to cell lineages dependent on the germ layer (Menon *et al.*, 2016).

Non-embryonic adult/somatic cells are found within postnatal tissues and exist in an undifferentiated, multipotent state with a more specialised nature of their cell types. Their ability to self-renew is limited and also vary in the degree of their plasticity potential, with these cell types committed to specific lineage differentiation (Malik and Rao, 2013).

Research laboratories have implemented the use of human and mouse embryonic stem cells in disease modelling and for the potential use in therapeutic approaches. Though they provide researchers with an unprecedented ability for in vivo disease modelling in vitro, the ethical issues surrounding embryonic stem cells has been an ever present and increasing obstacle for medical progression. However, the recent advancement in induced pluripotent stem cell generation and use may provide a solution to the many ethical and moral considerations of embryonic stem cells.

In 1958, a study carried out by Gurdon et al. demonstrated a cell's ability to re-instate pluripotency during end stage development via nuclear transcription. This technique was originally developed by Briggs and King, demonstrating successful nuclear reprogramming via the transplantation of nuclei of epithelial cells of the intestines from feeding tadpoles into enucleated eggs, which progressed into the development of healthy tadpoles, as reviewed by Sridharan and Plath in 2008 and later in 2016 by Menon at al.(Menon *et al.*, 2016) (Sridharan and Plath, 2008). This initial somatic cell nuclear transfer implied the presence of key factors responsible for induction and/or maintenance of pluripotency, producing the scaffold for the future breakthroughs in cellular reprogramming. In 2006, Takahashi and Yamanaka demonstrated the successful reprogramming of differentiated human somatic cells into a state of pluripotency through the retrovirus-mediated transfection of the transcription factors Oct3/4, Sox2, c-Myc and Klf4 (see figure 2) (Takahashi *et al.*, 2007). The generation of iPSCs using these factors, coined the "Yamanaka Factors", paved the way for a new era of translational and regenerative medicine, earning Takahashi and Yamanaka Nobel prize recognition.

The mouse iPSCs produced via the cellular reprogramming technique were indistinguishable from mouse embryonic stem cells in proliferation, morphology, teratoma formation and gene expression. Takahashi and Yamanaka also established the iPSCs ability to form germline transmission competent, adult chimeras produced by the transplantation of iPSCs into blastocysts. Since the discovery of the induction of pluripotent stem cells from somatic cells, there has been abundant number of studies and research papers published with the task of refining the technique. Initial generation of iPSCs implemented the use of viral vectors, the method integrated both the vector backbone and transgenes into the genome permanently (Takahashi *et al.*, 2014). Although this method was shown to successfully produce iPSCs, these vectors also produced insertional mutations which interfered with normal iPSC function whilst the

residual transgene expression was shown to influence differentiation into varying cell lineages and could even result in tumorigenesis (Drozd *et al.*, 2015). In order to combat this, efforts have been made in order to develop vector integration-free mouse iPSCs, with resulting cells obtained through derivation of liver cells with adenoviral vectors and embryonic fibroblasts. Although seen as an adequate replacement, the low frequencies obtained show the limitations in practicality for this approach vis-à-vis human cells, which require enhanced exposure to reprogramming factors (Hu, 2014).

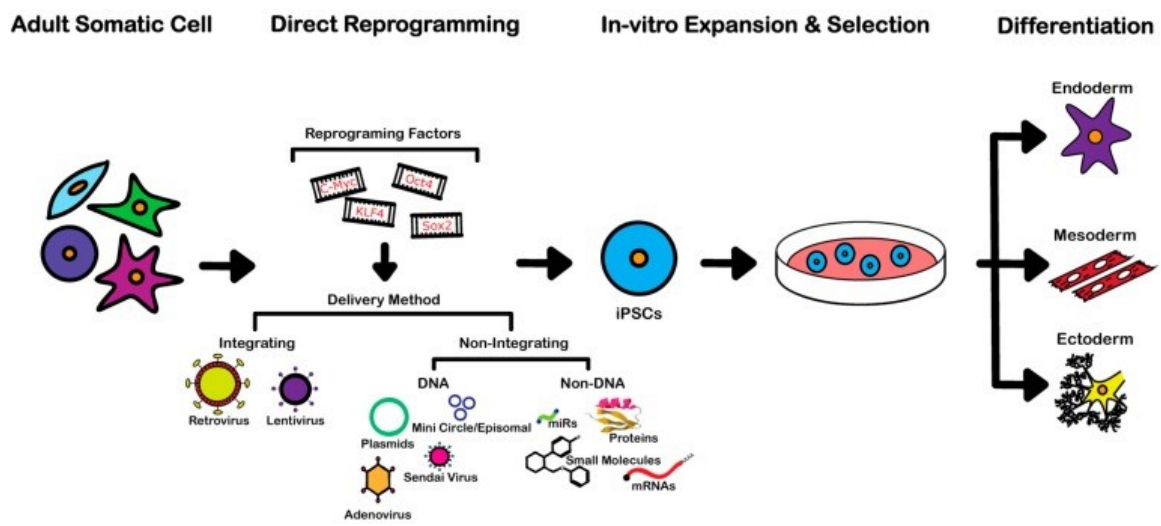

Figure 2: Somatic cell reprogramming

Figure 2: Figure above depicts the stages of reprogramming somatic cells to iPSCs through the ectopic expression of the transcription factors; Oct4, Sox2, C-Myc and Klf4. Initially the integration of these factors was achieved through lentiviral or retroviral vectors, however more recently progress has been made through the utility of plasmids and episomal adenovirus along with non-DNA beased techniques such as miRs and mRNAs. Once induced into the pluripotent state, iPSCs are able to differentiate into all three germ layers that can be utilised in disease modelling, cell therapy and drug discovery. (Menon *et al.*, 2016)

More recently, the development of inducible pluripotent stem cells derived from the single transfection of the episomal virus, oriP/EBNA1 (Epstein-Barr nuclear antigen-1) has become the forefront of somatic cell reprogramming to iPSCs (Drozd *et al.*, 2015). The oriP/EBNA1 vectors are ideal for cellular reprogramming of human somatic cells, theses plasmids allow for the transfection whilst relinquishing the need for viral packaging, thus are able to be removed from cell types via cell culture in drug absent conditions.

oriP/EBNA1 vectors within mammalian cells possess a stable, extrachromosomal replication and thus requires only trans-acting EBNA1 gene along with a cis-acting oriP element. These oriP/EBNA1 vectors have a replication frequency of once per cycle and have been shown to establish stable episomes in ~1% of the initial transfected cells under drug selecting conditions. Conversely, the removal of these conditions have demonstrated the loss of these stable episomes at ~5% per cell generation due to defects in partitioning and plasmid synthesis. (Junying *et al.*, 2009)

1.3.1 Neural Stem Cells (NSCs) and their Differentiation

The central nervous system (CNS), is generated from a small number of neural stem cells (NSCs) lining the neural tube, during development (Zhao and Moore, 2018). Studies in adult brains have demonstrated a reduction in NSCs in specific brain regions. Continued neurogenesis in hippocampus was confirmed in the 1990's, which, at the time, contradicted the prevailing dogma that neurogenesis did not occur within a fully developed human brain, whilst hinting at the possibility of utilising these NSCs for neural repair in disease (Zhao and Moore, 2018).

NSCs are multipotent stem cells with the capacity to self-renew and give rise to the three major cell types which make up the CNS in a defined sequence; firstly, neurons, followed by astrocytes and then oligodendrocytes (Han *et al.*, 2017).

Current research utilises hESCs and hiPSCs as cellular based platforms for differentiating into cell lines of interest. Research into neurodegenerative diseases has been hampered due to difficulties in obtaining neuronal cells and successfully culturing *in vitro,* however, the introduction of iPSC technology has revolutionised the field of research (D'Aiuto *et al.*, 2014). Various studies have demonstrated that iPSC-based models have the capacity to model selected aspects of neurological and neurodegenerative disorders (Zhao and Moore, 2018). Such platforms require cost effective, efficient and replicable protocols in order to generate uniform cultures of neurons in ample numbers for high throughput screening (D'Aiuto *et al.*, 2014). Currently, neuronal differentiation techniques first derive NSCs/NPCs from hESCs or iPSCs. Many techniques currently initiate neural differentiation through the use of Noggin, a bone morphogenesis protein (BMP) inhibitor, a crucial neural-inducing factor in mammalian cells (Han *et al.*, 2017). Different techniques are employed, however the most prevalent is the generation of embryoid bodies (EBs) followed by differentiation to neural rosettes (Tang, Yu and Cheng, 2017). These EBs are

3-dimensional, spherical aggregates that mirror a variety of key traits from early embryogenesis (D'Aiuto *et al.*, 2014). When cultured in specific selective culture media and growth factors, these aggregates generated from human iPSC or ESCs will differentiate into neural rosettes efficiently, however, factors such as their initial size can have an impact on their differentiation outcome (D'Aiuto *et al.*, 2014). Microwell arrays have been developed, these allow for a more efficient homogenous and uniform differentiation of EBs. The neural rosettes formed (representing a distinct class of NSCs), are isolated mechanically and transferred into low attachment plates where they form neurospheres (spherical cell aggregates), that can be propagated as 3-dimensional structures or expanded as a monolayer culture of NSCs/NPCs (D'Aiuto *et al.*, 2014). Generally, monolayer cultures are favoured as neurospheres are not ideal for high-throughput production of neurons due to technical difficulties in loading uniform numbers of spheres with identical size into multiple wells (D'Aiuto *et al.*, 2014). Many terminal differentiation steps from NSCs to neurons involve the induction of a different selective media with other growth factors on adherent culture systems previously coated with attachment factors (AFs) such as poly-L-ornithine (Ge *et al.*, 2016). Various studies have shown the advantages of using poly-L-ornithine opposed to other AFs, however, one study demonstrated that NSCs had a preferred neuronal differentiation via the ERK signalling pathway (Ge *et al.*, 2015).

1.4 Cellular Metabolism

Metabolism in human stem cells is tightly regulated in order to maintain the cells ability to self-renew and maintain pluripotency, with evidence showing a metabolic shift during differentiation (Ito and Suda, 2014). Studies have shown that differing stem cells, including those of iPSCs and neural stem cells (NSCs), exist within a hypoxic niche. Evidence suggests that the low oxygen tensions formed through hypoxia aid in the maintenance of an undifferentiated state and influence cell-fate and proliferation (Simsek *et al.*, 2010). Dormant human stem cells (HSCs) reside in a hypoxic niche located within the bone marrow cavity, indeed studies have shown that the oxygen saturation within the bone marrow is low with an oxygen tension of 10-30mm Hg (1.3-4.2%), obtained via the integration of two-photon intravital imaging (Ito and Suda, 2014). Due to stem cells existing in this hypoxic environment, a reliance on anaerobic glycolysis opposed to

mitochondrial oxidative phosphorylation (OXPHOS) has been observed for ATP production (Koopman *et al.*, 2013). Metabolic analyses of HSCs have shown the metabolic profile of these stem cells differ significantly than those of committed progenitors. It was shown that HSCs possess increasing levels of fructose-1,6-bisphosphate accompanied with an increase in pyruvate kinase activity, indicative of active glycolysis (Lunt and Vander Heiden, 2011). Studies have further supported the notion of HSCs favouring glycolysis as it has been shown there is decrease in the level of phosphoenolpyruvate whilst also showing an increase in pyruvate production, the substrate and product, respectively, of the final step in glycolysis (Simsek *et al.*, 2010)(Gu *et al.*, 2016).

Glycolysis is the process in which a molecule of glucose is metabolised to three-carbon pyruvate through ten steps. The glycolytic pathway enables the phosphorylation of glucose in order to produce glucose-6-phosphate, which is then converted to fructose-6-phosohate which is subsequently phosphorylated in order to produce fructose-1,6-biphosphate (Takubo *et al.*, 2013). During this two-step process of phosphorylation, two molecules of ATP are consumed. Dihydroxyacetone phosphate and glyceraldehyde 3-phospahte are produced through the degradation of fructose-1,6-biphosphate, with glyceraldehyde 3-phospahte is oxidised and further phosphorylated in order to form 1,3-biphosphoglycerate via inorganic phosphate during the glycolytic payoff phase (Lunt and Vander Heiden, 2011). Subsequently, the latter is then converted to produce the molecule, 3-phosphoglycerate thus producing a molecule of ATP due to substrate-level phosphorylation. The consequent 3-phosphoglycerate is isomerised yielding 2-phosphoglycerate which is dehydrated resulting in the formation of phosphoenolpyruvate (Lunt and Vander Heiden, 2011). As a result, the phosphoenolpyruvate is converted to pyruvate with the conversion producing another molecule of ATP. Four molecules of ATP are produced through two steps of substrate-level phosphorylation as two molecules of 3-phosphoglycerate are converted to two molecules of pyruvate through oxidation (Gu *et al.*, 2016). Per molecule of glucose oxidised, there is a net yield of molecules of ATP as two molecules are utilised during the glycolytic preparatory phase. Due to hypoxia, pyruvate is able to be reduced in order to from lactate in hypoxic conditions, alternatively it is able to be oxidised in order to yield acetyl-coenzyme A (Acetyl-CoA) when exposed to aerobic conditions and is also able to be completely oxidised to form CO_2 through the induction of the citric acid cycle (Takubo *et al.*, 2013)

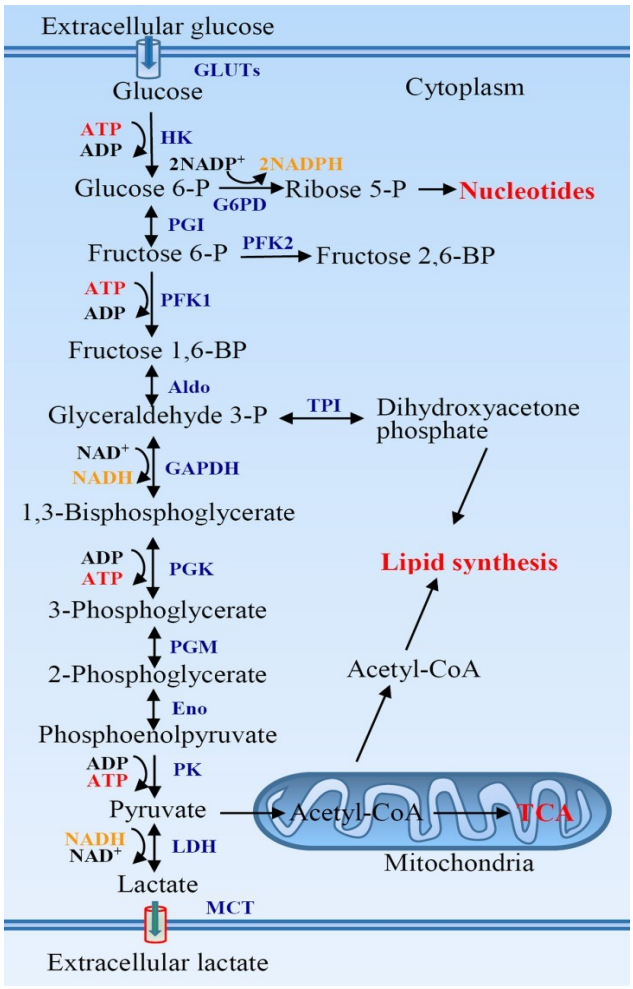

Figure 3: The glycolytic pathway

Figure 3. Figure depicts the glycolytic pathway along with its integration and association with other metabolic pathways (Takubo *et al.*, 2013).

Although iPSCs and NSCs maintain metabolic homeostasis through glycolysis, neurons require an increased amount of ATP for cellular respiration due to a lack of glycogen and high cellular demands, with energy requirements met via oxidative phosphorylation (OXPHOS) (Koopman *et al.*, 2013). It has been demonstrated through a variety of studies that mitochondrial OXPHOS dysfunction leads to wide array of neurological disorders, especially observed in neurodegenerative diseases (Ivanov *et al.*, 2014). Observations have shown the disappearance of HK2 and LDHA coupled with PKM2 splicing to form PKM1 initiates the metabolic shift from aerobic glycolysis to OXPHOS in neural differentiation of NPCs to neurons (Hüttemann *et al.*, 2007). The disappearance of these markers has been shown to signal differentiation towards neurons, however constitutive expression of HK2 and LDHA results in neuron death, indicative of the importance of

inhibition of glycolysis in neural differentiation (Ito and Suda, 2014). Although it is widely regarded that neurons require OXPHOS for cell maintenance, the mechanisms by which the pathway is favoured is largely unknown.

Mitochondrial oxidative phosphorylation (OXPHOS) is plays a crucial role in cellular energy metabolism and sustains organelle function. The OXPHOS system utilises the electron transport chain combined with cell respiration and ATP synthesis in order to generate the majority of cellular energy, whilst also being involved in free radical production and apoptosis (Ivanov *et al.*, 2014). The electron transport, a key element of the OXPHOS system, comprises NADH-dehydrogenase (complex I), succinate dehydrogenase (complex II), ubiquinone bc_1 complex (complex III) and cytochrome *c* (Cyt *c*) with cytochrome *c* oxidase (CcO- complex IV) (Hüttemann *et al.*, 2007). Electrons transferred via the electron transport chain are mainly derived through NADH and are able to infiltrate the chain through complex I. Additionally, electrons are also able to be fed directly into the ubiquinone/ubiquinol pool via complex II. The electrons are able to transfer through the electron transport chain to oxygen, whilst the movement of protons across the inner membrane of the mitochondria generates the mitochondrial membrane potential. This proton gradient is used by ATP synthase (complex V), coupling the backflow of the protons which had previously been transported by the electron transport chain in order to produce ATP (Hüttemann *et al.*, 2007).

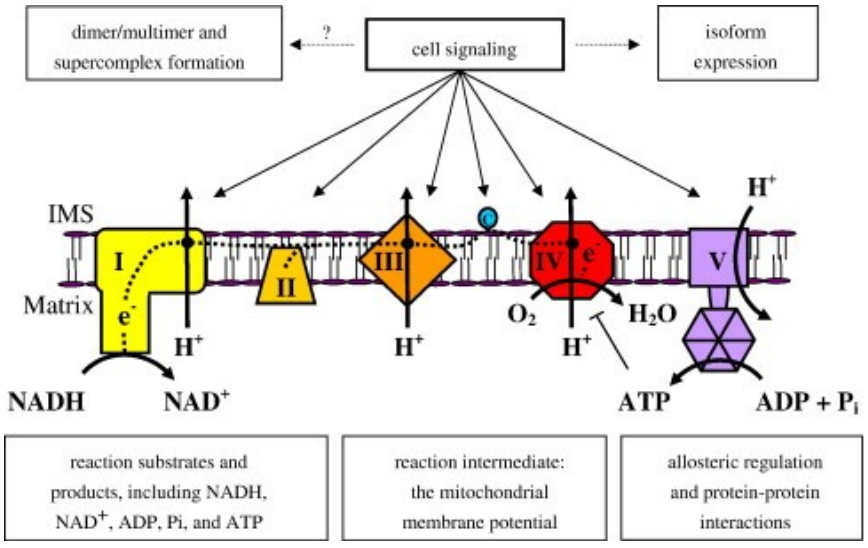

Figure 4: OXPHOS Pathway in mammalian cells

Figure 4. Figure depicts the regulation of OXPHOS within mammalian cells. Functionally, OXPHOS is tightly regulated via a hierarchy of regulatory mechanisms; tissue-specific isozymes are expressed by organs, signals from outside of the cell are mediated to mitochondria through signalling cascaded and allosteric regulation results in the alteration of energy production within the intermembrane space (Hüttemann *et al.*, 2007).

1.5 Autophagy

Over the past decade, investigation into macroautophagy (hereafter referred to as autophagy) and its biological mechanisms has been a staple in molecular biology due to its vital role in physiological and disease processes. Autophagy is an evolutionary conserved catabolic pathway, vital for its necessity in physiological processes, at the forefront is in which long-lived proteins and damaged organelles are delivered to lysosomes for degradation in order to maintain energy homeostasis (Johansen and Lamark, 2011). Autophagy arises when the sequestered proteins and organelles forming an autophagasome fuse with a lysosome in order to degrade the cargo. Autophagy proceeds in sequential steps in order to form mature autophagosomes; (i) de novo formation of a phagophore, a small membrane cistern eventually sealing itself into a double-membrane bound structure, (ii) elongation of this lipid-based membrane, before (iii) encapsulation of intracellular cargo to form a mature autophagosome (Thelen *et al.*, 2012). This autophagasome fuses itself with the endocytic system so that it may deliver its contents to lysosomes in order for degradation to occur. Once classed as a type of programmed cell death, autophagy is widely viewed as a basic cell survival mechanism, which has been found to be critical in the circumvention of nutrient stress and starvation, initially found in the study of yeast cells, of which the first genes relating to autophagy were discovered (Chen *et al.*, 2014). Subsequently, various studies highlighting the importance of autophagy in mammalian cell counterparts have been carried out, displaying the importance of this catabolic pathway in cell maintenance and normal development.

The group of hereditary neurodegenerative diseases, NCLs, are attributed to a loss or impairment of autophagy, with the autophagy-lysosome pathway enabling the degradation of damaged organelles, long-lived proteins and the clearance of intracellular pathogens and toxic protein aggregates (Ganley *et al.*, 2011). Various studies have found that an impairment of these autophagic pathways results in the accumulation of

ubiquitin-positive aggregates within the cytoplasm, leading to neurodegeneration in NCL patients. (Katsuragi, Ichimura and Komatsu, 2015)

The complete cellular pathway of autophagy occurs in sequential steps (figure 5); initiation, phagophore expansion, autophagasome maturation, fusion with the vacuole/lysosomes, cargo degradation in the lysosome and efflux (Thelen *et al.*, 2012). The nature of the various steps makes it vital to assess autophagic activity at each step or to monitor flux. Currently in most mouse models, many of the 'core' *ATG* genes ae knocked out in order to observe and understand the physiological role of autophagy in mammals (Wang *et al.*, 2013).

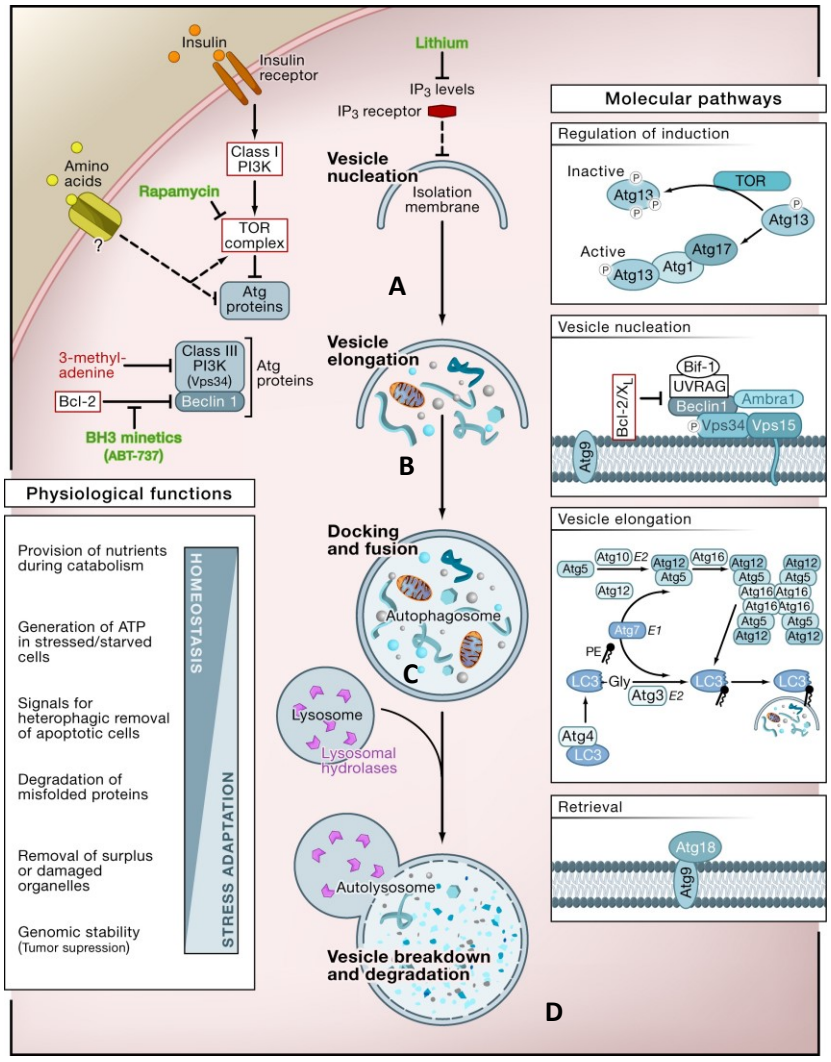

Figure 5: Autophagic Cellular pathways

Figure 5: The cellular pathways during autophagy follow distinct, sequential steps: (**A**) vesicle nucleation (the formation of the isolation membrane/phagophore), (**B**) vesicle elongation (growth and closure), (**C**) fusion of the double-membraned autophagosome along with lysosomes in order to form an autolysosome and (**D**) finally the lysis of the autophagosome inner membrane leading to the breakdown of its contents within the autolysosome. Here are shown the complexes identified in mammalian cells, excluding Atg13 and Atg17- found only in yeast cells. Autophagic inhibitors and activators are shown above in red and green, respectively (Levine and Kroemer, 2008).

2.0 Aims

The overall aim of the project is to utilise existing techniques from within the McKay lab as well as current literature, in order to successfully differentiate CLN7 patient and control induced pluripotent stem cells to neural progenitor cells and subsequently neurons. In order to achieve this, a stepwise protocol, allowing for the minimization of induction of a variety of exogenous growth factors, thus encouraging differentiation of neuroectoderm will be implemented. Through successful differentiation of CLN7 iPSCs and controls, analysis utilising techniques such as qPCR, western blot analysis and immunocytochemistry will be implemented in order to deduce any phenotypic differences between the two cell types. Targets relating to metabolism, inflammation, potency and autophagic flux will be interrogated in order for this deduction. Currently, very little information is given for CLN7, however, there has been extensive research directed towards neuronal ceroid lipofuscinosis in the last decade with each variant sharing an impairment in autophagy. Due to this common trait amongst the varying NCL variants, we hypothesize that there will be a decrease in autophagic flux in CLN7 cell types when compared to control counterparts, with an increase in lysosomal storage material expected. We also hypothesise a change in metabolic shift expected due to intrinsic links between regulation of cell homeostasis and metabolism. Although we expect to see differences, previous research within the McKay lab has shown that CLN7 iPSCs display little to know difference in phenotype, this leads us to believe that any changes observed will occur as iPSCs differentiate towards neuronal progenitor cells and thus neural cells.

3.0 Materials and Methods

3.1 Materials

Table 3: Cell culture reagents

Reagent	Company	Catalogue Number
DMEM	Sigma	D6546
MEM Non-essential amino acids (NEAA)	Life Technologies	1140050
L-glutamine	Sigma	G7513
Penicillin/Streptomycin (Pen/Strep)	Sigma	P0781
Dulbecco's Phosphate buffered saline	Sigma	D8662
DMEM F12	Gibco, Life technologies	31331093
B-mercaptoethanol	Life Technologies	31350-010
Mitomycin C	Sigma Aldrich	M4287
TrypLE express	Gibco, Life Technologies	12605028
bFGF	R&D Systems	233-FB-025
Laminin	Millipore	CC095
Gelatin from porcine skin	Sigma	G1890
Rock Inhibitor (Y-27632)	Sigma	Y0503-1mg
Dimethyl sulfoxide	Sigma	BP231-100
N2 supplement	Life Technologies	17502048
B27 supplement	Life Technologies	12587010
Heparin	Sigma	12587010
Matrigel	BD Bioscience	H3149
MTeSR™	Stemcell Technologies	05851/05852
Neurobasal media	Thermo Scientific	21103049
Sodium Pyruvate	Sigma Aldrich	P2256

Table 4: Materials

Materials	Company	Catalogue Number
RIPA buffer	Thermo Scientific	89900
Bradford Reagent	BioRad	500-0006
Acrylamide/bis-acrylamide 30%	Sigma	A7802
TEMED	Sigma	T9281
Tween 20	Sigma	19379
Pageruler Prestained protein ladder	Thermo Scientific	26616
Marvel Original dried skimmed milk	Supermarket	n/a
Protease inhibitor cocktail	Sigma Aldrich	P8340
Phosphate buffered saline tablets	Sigma	P4417
Immobilon Western Chemiluminescent HRP substrate	Merck	WBKLS0500
APS	Sigma	215589-100G
Blot absorbent filter paper	BioRad	1703932
Methanol	Fisher Scientific	10667032
Glycine	Sigma	G8898-500G
Tris base	Fisher Scientific	BP152-1
Sodium dodecyl sulphate	VWR International	27926.238
RNeasy mini kit	Qiagen	74104
RQ1 RNase-free DNase kit	Promega	M6101
dNTPs	Promega	PRU1240
M-MLV reverse transcriptase	Promega	M1701
RNasin plus inhibitor	Promega	N2611
Random primers	Promega	C1181
KAPA SYBR FAST universal 2x qPCR master mix	KAPA Biosystmes	K4601
GelRed nucleic acid stain	VWR International	41003.
Agarose	Sigma	A5093
O'Generuler ladder mix	Fisher Scientific	1188393

Isopropanol	Sigma	190764
4% Paraformaldehyde	Sigma	15812
Triton X-100	Sigma	T8532
Bovine Serum Albumin (BSA)	Sigma	05479

Table 5: Neural Induction Media (NIM)

Component	Volume
DMEM/F12 1:1	48.5 mL
NEAA	0.5 mL (1x)
N2	0.5 mL (1x)
bFGF	10 µL (20ng/mL)
Heparin	50 µL (2µg/mL)
Pen/Strep	0.5 mL (1x)
Plasmocin	50 µL

Table 6: Neural Expansion Media (NEM)

Component	Volume
DMEM/F12 (1:1)	48.5 mL
NEAA	0.5 mL (1x)
N2	0.5 mL (1x)
B27	1 mL (1x)
bFGF	10 µL (20ng/mL)
Heparin	50 µL (2µg/mL)
Pen/Strep	0.5 mL (1x)
Plasmocin	50 µL

Table 7: Neural Maturation Media (NM)

Component	Volume
DMEM/F12 (1:1)	48.5 mL
Horse Serum	0.5 mL (1%)
B27	1 mL (1x)
Pen/Strep	0.5 mL (1x)
Plasmocin	50 µL

Table 8: Complete DMEM

Component	Volume
DMEM	435 mL
FBS	50 mL
L-Glutamine (200mM)	10 mL (4mM)
Pen/Strep	0.5 mL (1x)

3.1 Cell Culture

Induced pluripotent stem cells (CLN7 466, 474 as well as control) originally cultured on mouse embryonic fibroblasts (MEFs) in complete DMEM media (see table 7) until desired confluency. Following maturation of iPSCs, cells were transferred onto Matrigel covered plates and cultured in feeder free stem cell culture media, mTESR, supplemented with Plasmocin antibiotics. The commercially available human embryonic stem cell (hESCs) line, Shef3, was purchased from the UK stem cell bank. These cells were cultured under feeder free conditions in mTESR, supplemented with Plasmocin antibiotics, incubated at 37^{o}C and 5% CO_2. CLN7 HDFs and nHDFs, as well as HEK293 cells were cultured in complete DMEM prior to reprograming in 6-well plate format, supplemented with Plasmocin antibitoics. All cells were incubated at 37^{o}C and 5% CO_2

3.2. Neural Differentiation

72 hours prior to neural differentiation, neural induction media containing Poly Vinyl Alcohol (PVA) was prepared. PVA at a concentration of 4mg/mL (i.e. 200mg in 50mL) was added to DMEM/F12 and shaken vigorously for one hour followed by placing media on a roller for 72 hours at 4^{o}C in order to completely dissolve PVA. The media was then filtered through a 0.22µm PES syringe driven filter in order to sterilise. Subsequent media was supplemented with factors listed in table 4.

Feeder free iPSCs were enzymatically disrupted using TrypLE in order to obtain a single cell suspension, cell containing suspension was centrifuged at 1080g (1200rpm) for 5 minutes. Pellet formed was resuspended in NIM, in a 96 V bottom well plate at a seeding density of 7,500 cels/well (100µL media containing cells/well). 24 hours post seeding, neuroepithelial cell clusters formed in the suspension. Media was replaced every day for the following five days. On day 6, aggregates were re-seeded onto laminin coated dishes (20µg/mL) to allow for the formation of neural rosettes (2-3 days). Once rosettes had formed, rosette clusters were picked using a 21-gauge sterile needle. Cell clusters were centrifuged at 200g for 3 minutes and resuspended in Neural Expansion Media (see table 5). Subsequent media can be cultured on low attachment plates in order to promote the proliferation of Neural Stem Cells (NSCs), however, during the project, Neural progenitor cells were cultured as a monolayer on laminin coated dishes (20µg/mL). Following

protracted culture, the NPCs were enzymatically disrupted using TrypLE and centrifuged at 800g for 8 minutes, pellet was then resuspended in Neural Maturation Media (see table 6) and reseeded onto laminin coated dishes of a 6 well plate at a seeding density of 50,000 cells/well. Half media changes were performed every 3 days in order to prevent cell overexposure to surrounding air. Cells were continually cultured until visual formation of axons of the neuronal cells.

3.3 Bradford assay:

Cell types of interest that were utilised for western blot analysis were initially lysed through the use of RIPA buffer augmented with 1µL: 100µL of protease inhibitor cocktail. The subsequent lysates were then stored in the -80^{O}C freezer until required.

Prior to the implementation of Western Blot analysis, total protein was quantified utilising a Bradford assay, the preferred colorimetric assay for quantifying total protein concentration. Initially, Bradford reagent was diluted at a 1:5 ratio (v/v) with deionised H_2O. 195µL of the diluted Bradford reagent was then added in triplicate to wells of a nucleon delta surface, transparent 96-well plate. 5µL protein standards were then added to wells containing diluted Bradford reagent in increasing concentrations from 0.5µg - 8µg/µL. Prior to the addition of experimental lysates to wells containing Bradford reagent, the lysates were diluted 1:10 in deionised water in order to minimise the effects of RIPA buffer on Bradford reagent when estimating protein quantification. The consequent standard and sample containing, 96-well plate was then analysed by the Synergy HT microplate spectrophotometer at an absorbance of 630nm.

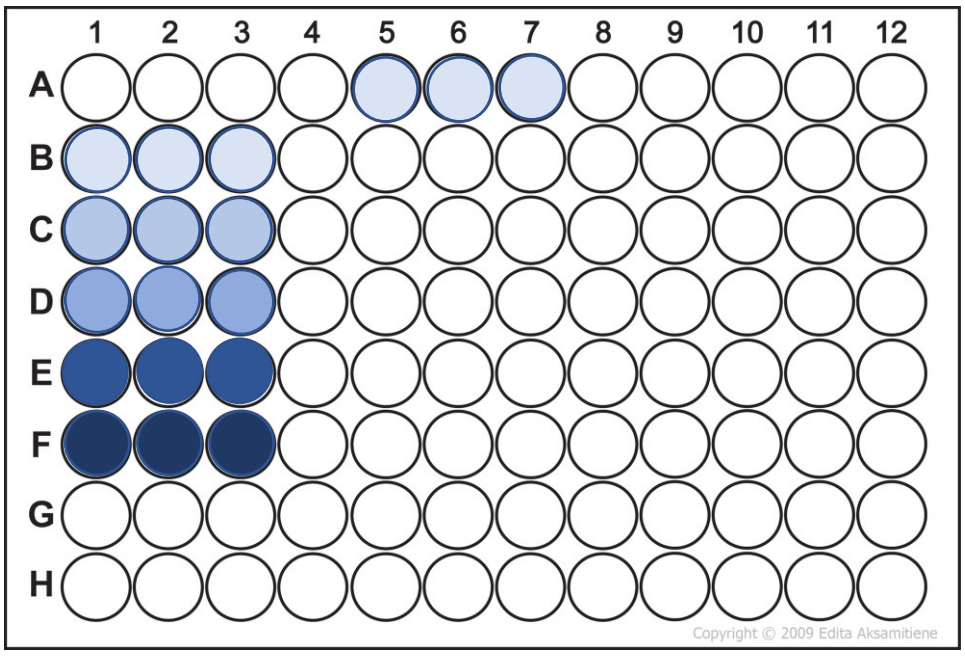

Figure 6: Typical Bradford Assay Set-up

Figure 6: Typical representation of a Bradford assay plate prior to spectrophotometric analysis. Columns A-F (rows 1-3) represent the triplicate standards of increasing protein concentration from 0µg/5µL (A) - 8µg/5µL (F). Column A (rows 5-7) represent example of loaded lysate samples for quantification determination. A standard curve is then produced via spectrophotometer analysis of standards, from which the protein lysate can be quantified.

3.4 Polyacrylamide Gel Electrophoresis

Table 9: 10% Acrylamide Gel

Separation gel:	**Stacking gel:**
3.33mL (3:1) acrylamide : ddH_2O	0.67mL 3:1 acrylamide:ddH_2O
4.17mL ddH_2O	2.3mL ddH_2O
2.5mL Solution A	1mL solution B
10µL Temed	5µL Temed
50µL APS	30µL APS

Table 10: 15% Acrylamide Gel

Separation gel	**Stacking Gel**
5 mL (3:1) acrylamide : ddH_20	0.67mL 3:1 acrylamide:ddH_2O
2.4 mL ddH_20	2.3mL ddH_2O
2.5 mL Solution A	1mL solution B
10 µL Temed	5µL Temed
100 µL APS	30µL APS

Table 11: Solution A- pH adjusted to 8.8

Component	Concentration
Tris-HCL	1.5M
SDS	0.4%

Table 12: Solution B- pH adjusted to 6.8

Component	Concentration
Tris-HCL	0.5M
SDS	0.4%

SDS-PAGE gels can be imported pre-cast; however, in the McKay Lab we opted to produce our own gels in order to alter the percentage of the acrylamide depending on the size of the target protein. Prior to manufacturing the gels, the glass plates (1.0mm used throughout) are placed in the clamp and tested for leakages using ddH_2O or 70% ethanol. During the project various percentage gels were produced in relation to the size of the protein of interest. For the production of a 10% gel, the following was carried out for separation gel; 1mL ddH_2O added to 3mL 30% acrylamide, 3.33mL of the mixture was transferred into a new falcon tube (A), leaving 0.67mL in remaining tube (B). Followed by the addition of 4.17mL ddH_2O added to tube A. A volume of 2.5mL of solution A (see table 9) is then added to tube A. Immediately before pouring mixture into 1.0mm plates, 50µL of APS and 10µL TEMED is added to tube A causing mixture to polymerise and solidify after approximately 20 minutes. When producing the stacking gel, the following was performed; 2.3mL ddH_2O was added to tube B followed by the addition of 1mL of solution B (see table 7). Immediately before pouring mixture into 1.0mm plates, 30µL APS and 5µL TEMED was added to cause polymerisation of gel. Formula for the separation gel of differing percentage gels was altered accordingly (refer to tables 9 and 10). Gels produced are able to be stored for ~1 week in PBST buffer stored at 4°C.

3.5 Western Blot Analysis

Table 13: 10X Running Buffer

Component	**Concentration**
Tris base	250mM
Glycine	1.9M
SDS	1%

***Components are dissolved in 1 litre of ddH_2O**

***This is then diluted 1:10 in ddH_2O for final use**

Table 14: 1x Blotting Buffer

Component	Concentration
Tris base	25mM
Glycine	190mM
Methanol	20%

***Components are dissolved in 1 litre of ddH_2O**

Once total protein quantity of cells of interest was established, immunoblotting vis-a-vis Western blot was implemented. Throughout the project a protein quantity of 20µg was loaded per well as previous work found this to be the optimal quantity. Laemmli buffer was added to the protein sample at a dilution of 1:5 and incubated at $95^{O}C$ for 5 minutes, this allows for the degradation of disulphide bridges in the proteins, allowing for the adoption of random coil conformation thus allowing for better separation along the SDS-PAGE gels. Whilst this is occurring the gels were loaded into the tank, which was filled with 1x Running Buffer (see table 9). Once the proteins had been incubated for 5 minutes, they were loaded into the wells of the SDS-PAGE gel alongside the PageRuler Prestained protein ladder; image below demonstrates the SDS-PAGE band profile of the PageRuler Prestained protein ladder:

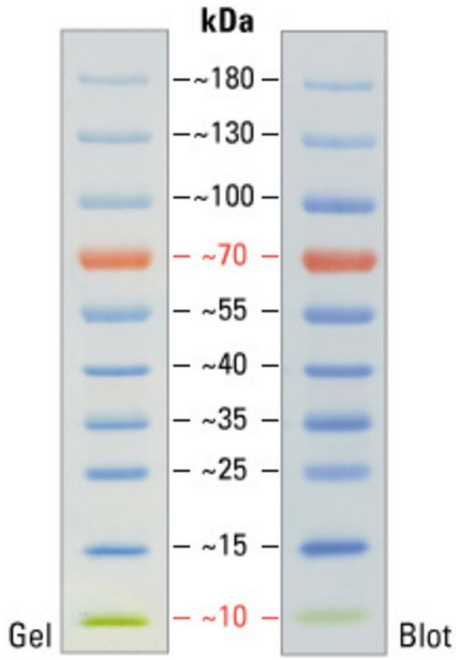

Figure 7: PageRuler Prestained Protein Ladder Used throughout Western Blot Analysis

Figure 7: representation of the SDS-PAGE band profile of the Page Ruler Prestained protein ladder used throughout western blot analysis.

The gels were then run at 90V until the proteins had passed through the stacking gel and had entered the separation gel, following this the voltage was increased to 120V and was run for a further 1.5-2 hours. Following the completion of the run, four pieces of blotting paper, as well as a nitrocellulose membrane were soaked in 1x blotting buffer (see table 10). The gel cast was transferred onto a nitrocellulose membrane with two pieces of blotting paper above and below the nitrocellulose and was run on the blotter for one hour at 15V. Following the transfer, the membrane was blocked for a minimum of one hour using block solutions relative to the target antibody, throughout the project milk block (5% w/v non-fat milk powder in PBS + 0.01% Tween 20) and BSA block (5% w/v bovine serum albumin in PBS + 0.01% Tween 20). The block was then removed and incubated with primary antibody of interest, which was dilute in corresponding block at the dilution recommended by the data sheet from the company from which they were bought. The primary antibody was incubated overnight at $4^{O}C$. The primary antibody was then removed and the membrane was washed with PBS + 0.01% Tween 20 three times for ten minutes per wash. Following this, the secondary antibody was then diluted in either milk block or BSA block at appropriate dilution, the membrane was then incubated in the secondary containing block at room temperature for one hour. The membrane was then washed using PBS + 0.01% Tween 20 three times for ten minutes per wash. The membrane was then incubated with ECL for one minute. All images produced were visualised on the Biorad Chemidoc touch gel dock transilluminator using western gel settings.

Table 15: Antibodies Utilised in Western Blot Analysis

Antibody	Dilution	Secondary	Company	Catalogue Number
P62	**1:2000**	**Mouse**	**Abcam**	**Ab86416**
P70	**1:1000**	**Rabbit**	**Cell Signalling**	**2708S**
p-p70	**1:1000**	**Rabbit**	**Cell Signalling**	**9205S**
β-actin	**1:10,000**	**Mouse**	**Sigma Aldrich**	**A2228**

3.6 RNA Extraction

Prior to RT-PCR, RNA was extracted from desired cells once they reached appropriate confluency, with no more than 1 x 10^7 cells harvested. The cells were enzymatically disrupted using TrypLE express and washed with PBS; the cells were centrifuged at a speed of 1080g for 5 minutes until a pellet formed. The supernatant was then removed and was re-suspended in 350 µL of Buffer RLT (acts as a lysis buffer for RNA isolation), the sample was then immediately taken to the -80 freezer where it was left overnight. Following the lysis of the cells, the samples were thawed and homogenised via pipetting through 25G needle and syringe. Following this, the RNA was isolated from the sample using the RNeasy mini kit and subsequent protocol provided by Qiagen. Following this, one volume (350µL) of 70% ethanol is added to the lysate and is well pipetted in order for the ethanol to sufficiently mix with the lysate. Up to 700µL of the sample, including any precipitate, was then transferred to an RNeasy Mini spin column in a 2mL collection tube (both supplied by Qiagen) and was centrifuged for 15 seconds at ≥8000g, the subsequent flow through was discarded. Subsequently the mixture then undergoes DNase digestion in order to remove any genomic contaminant from the sample. To begin, 350µL Buffer RW1 was added to the RNeasy column and centrifuged at ≥8000g for 15 seconds, with the flow through discarded. From here, 10µL of DNase I stock solution was added to 70µL of Buffer RDD (63µl RNase free ddH_2O + 7µL 10x DNase buffer) and mixed by gently inverting the tube and briefly centrifuging. The DNase I incubation mix (80µL) was added directly to the RNeasy column membrane and was incubated at room temperature for 15 minutes. Following the DNase digest, 350µL of Buffer RW1 was added to the RNeasy

column and was then centrifuged at ≥8000g for 15 seconds with the flow through being discarded. Next, 500µL of Buffer RPE was added onto the column and centrifuged at ≥8000g for 15 seconds, the flow through was then discarded. Again, 500µL of Buffer RPE was added directly onto the mini spin column; however, it was centrifuged for 2 minutes at ≥8000g. The flow through was once again discarded and the spin column containing no other buffer was centrifuged at ≥8000g for 1 minute in order to dry the membrane. Once the following step had occurred, the RNeasy spin column was transferred into a new 1.5mL collection tube (supplied by Qiagen) and 30µL of RNase free water was added onto the spin column and left to stand for 5 minutes before it was centrifuged for 1 minute at ≥8000g. The remaining 30µL sample in the 1.5mL collection tube contained the total RNA content of the desired cells. Once the RNA had been successfully isolated, the amount of RNA in the sample was quantified by loading 1µL of the sample onto the NanoDrop Microvolume Spectrophotometer and Fluorometer.

3.7 Reverse Transcrption

Once RNA extraction had been successfully completed, cDNA was produced in order to perform Reverse-Transcriptase Polymerase Chain Reaction (RT-PCR). One microgram of the RNA product was suspended in RNase free water up to 12.4µL, 1µL of random primers was then added and the complete mixture was incubated at 70°C for five minutes. Whilst the sample incubated, the following was made up per reaction:

- 5µL of M-MLV 5x reaction buffer
- 5µL of dNTPs – the monomeric substrates for the polymerization reaction, the DNA polymerase covalently link the free –OH group on the 3’ carbon of a growing chain of nucleotides to the α-phosphate on the 5’carbon of the next dNTP.
- 0.6µL RNasin- a ribonuclease inhibitor.
- 1µL M-MLV RT- a recombinant DNA polymerase that synthesizes a complementary DNA strand from single stranded RNA.

Once the previously stated components were added to the mixture post 70°C incubation, the subsequent mixture was incubated at 37°C for one hour. Once the previous steps have been completed the mixture was incubated at 95°C for five minutes, following this RT-PCR was carried out, alternatively the mixture could be frozen in order to stop the reaction and thus RT-PCR can be conducted at a later date.

3.8 Reverse-Transcriptase Polymerase Chain Reaction (RT-PCR)

Following the successful generation of cDNA from RNA, RT-PCR was carried out in order to qualitatively demonstrate the expression of various endogenous genes (see table 12) in two different CLN7 iPSC patient lines and in controls as well as in CLN7 474 and Control NPCs produced through neural differentiation. Per reaction, the following solution was made:

Table 16: Components and their corresponding volumes during RT-PCR reactions.

Component	Volume
5x Q5 Reaction Buffer	5µL
10mM dNTPs	0.5µL
10mM Primers (forward + reverse)	2.5µL
Q5 DNA polymerase	0.25µL
DNase/RNase free ddH_2O	15.75µL
cDNA	1µL

The samples were then taken to the Agilent sure cycler 8800 thermocycler in order to perform the polymerase chain reaction, during the project the following cycling parameters were carried out:

- 98°C x 5 minutes
- 98°C x 30 seconds
- 55°C x 30 seconds
- 72°C x 60 seconds

x28 cycles

- 72°C x 5 minutes

The subsequent PCR products were ran along a 1-2% agarose gel supplemented with GelRed nucleic acid gel stain. All images produced were visualised on the Biorad Chemidoc touch gel dock transilluminator using GelRed nucleic acids settings.

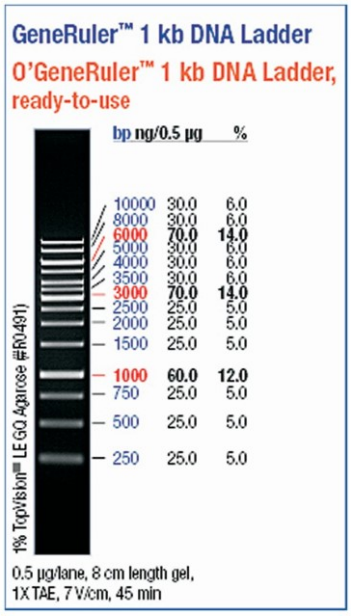

Figure 8: O'generuler 1kb ladder used in RT-PCR analysis

For primer information see appendix.

3.9 Quantitative Polymerase Chain Reaction (qPCR)

Following RNA extraction and in turn cDNA production, subsequent cDNA was diluted 1 in two in DNase/RNase free ddH_2O. The following master mix was produced per reaction:

- 5µL SYBR green
- 3.6µL DNase/RNase free water
- 0.4µL Primer (forward and reverse)
- 1 µL cDNA

9µL of master mix (excluding cDNA) was added in triplicate into a semi-skirted 96-well plate with the addition of 1µL of cDNA following. Following the addition of cDNA samples to subsequent master mix, the 96-well plate was covered using a plastic PCR film supplied from Thermofisher in order to prevent evaporation of samples. The plate was taken to the AB Step One Plus Real Time Thermocycler and was ran using standard SYBR settings including melt curves with 40 cycles. The data produced from the reaction was then exported into an Excel file, from which data analysis was undertaken in order to calculate relative expression with statistical analysis implementing the use of an independent T-Test.

3.10 Immunofluorescent Cell Staining

Cultured cells of interest had media removed before being washed with phosphate buffered saline (PBS) five times, however cells with surface adhesion issues were washed three times in order to compensate for their low adhesion. Cells were then fixed in paraformaldehyde diluted in PBS to a final concentration of 4% for 15 minutes. The fixed cells were then washed three or five times depending on the cell type, before the permeabilization step in which the cells are immersed in PBS containing 0.3% Triton-X100 for ten minutes at room temperature. The cells were then washed again 3-5 times depending on cell type, before being blocked in PBS containing 2% bovine serum albumin (BSA) and 0.1% Tween 20 for a minimum of 30 minutes. The block was then removed, and the primary antibody was diluted at the appropriate dilution factor (see table 17 for dilution factor details) in the BSA and Tween 20 containing PBS block, the cells were then immersed in the suspension and left overnight at 4^{O}C. The block containing the primary antibody was then removed and washed a further 3-5 times before the secondary antibody (see table 17 for details) was diluted in the PBS containing BSA and Tween 20 block. The dilution factor of the secondary antibodies was dependent on the company from which they were purchased; Northern lights from R&D systems had a dilution factor of 1:400, whereas Alexa fluor from Invitrogen was 1:500. The cells were incubated in the block containing secondary antibody for one hour at room temperature in the dark due to the photosensitivity of the secondary antibodies. The block containing secondary antibody was removed before a final wash with PBS 3-5 times, the cells were then immersed in PBS and taken for viewing. All images produced for immunofluorescent staining were captured using the Leica CTR 600 live cell-imaging microscope.

Table 17: Primary ICC Antibodies

Antibody	Species	Dilution	Company	Catalogue Number
Oct4	Goat	1:200	Abcam	Ab27985
Sox2	Goat	1:100	R&D Systems	AF2018
Tra-1-81	Mouse	1:200	R&D Systems	MAB8495
Lamp1	Rabbit	1:200	Abcam	AB24170
β-III-tubulin	Mouse	1:200	Abcam	Ab7751

Table 18: Secondary ICC Antibodies

Antibody	Dilution	Absorption (nm)	Emission (nm)	Company	Catalogue number
Donkey anti-Goat IgG, Alexa Fluor 568	1:500	578	600	Thermo Fisher	A11057
Goat anti-Mouse IgG, Alexa Fluor 488 (Green)	1:500	495	518	Thermo Fisher	A10684
Goat anti-Mouse IgG, Alexa Fluor 568 (Red)	1:500	579	601	Thermo Fisher	A11004
Goat anti-Rabbit IgG, Alexa Fluor 488	1:500	495	519	Abcam	Ab150077
DAPI	1:1000	348	453	Thermo Fisher	D1306
Mitotracker Red (Organelle Stain)	!mM Solution	581	644	Thermo Fisher	M22425

3.11 Statistical Analysis

Statistical analysis on qPCR data collected from iPSC and HDF analysis was performed using the one-way analysis of variance (ANOVA) with posy-hoc, Tukey analysis. Whereas analysis comparing data sets between patient NPCs and healthy controls was performed using Independent Samples t-tests. All data is expressed as the standard error of mean values (±SEM) of experiments with an n=3, performed in triplicate. Values of $p < 0.05$ was considered statistically significant. All statistical analyses were performed using the software SPSS (Version 22.0, 2013, IBM Corp., Armonk, NY, USA; SPSS Inc,. Chicago, IL, USA).

4.0 Results

The use of induced pluripotent stem cells has become an ever more prevalent and effective tool in disease modelling in vitro and for the generation of therapies. Indeed, previous studies have demonstrated the generation of various cell line via iPSCs through various differentiation protocols. In this study I sought to validate iPSCs available within the McKay lab from CLN7 patients, with the intention of performing neural differentiation in order to characterize the phenotypic changes occurring throughout neural differentiation.

4.1 iPSC Production

Induced pluripotent stem cell (iPSCs) lines for CLN7 patient cells and controls were provided by the McKay lab throughout the project, which were produced through somatic cell reprogramming. Firstly, HDFs of both patient and control cell lines underwent nucleofection through the use of the Amaxa Nucleofector 2b, thus supplying cells with episomal plasmid-based reprogramming factors; SOX2, OCT4, KLF4, I-Myc and shp53, necessary for induction of pluripotency. Furthermore, in order to improve efficiency, additional EBNA1 expression plasmid was added. The schematic below depicts the McKay lab protocol for iPSC production via somatic cell reprogramming.

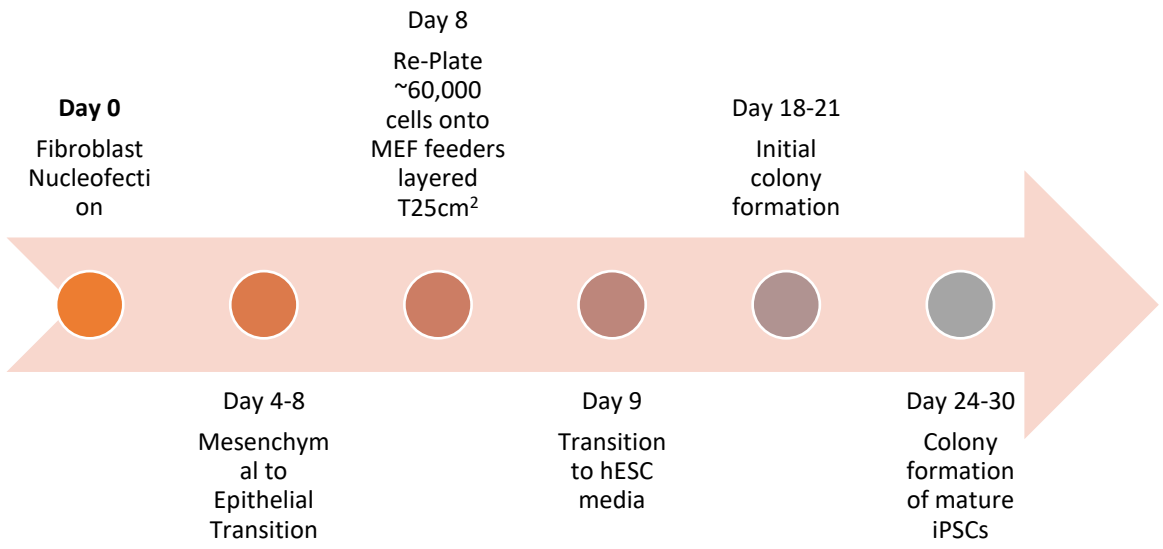

Figure 9: Initiation and Production of iPSCs

Figure 9: Figure depicts the initiation and production of induced pluripotent stem cells from fibroblasts at each stage. Prior to initiation of stepwise protocol of iPSC production, HDFs first undergo nucleofection.

4.2 CLN7 and Control iPSCs Display Pluripotent Characteristics

Following somatic cell reprogramming, subsequent induced pluripotent stem cells were validated using reverse transcriptase PCR (RT-PCR) in order to qualitatively assess the cells pluripotency targeting the gene expression of Oct4, Lin28 and Nanog. Following successful assessment through RT-PCR, qPCR analysis was implemented in order to quantitatively assess pluripotency markers Lin28A and SOX2. Finally, immunocytochemistry was performed in order to definitively display CLN7 and controls pluripotency characteristics by staining for; Oct4, SOX2 and Tra-1-81.

The targets; Oct4, Lin28 and Nanog, known to be expressed in pluripotent stem cells, were assessed. The transcription factor, Oct4, encoded by the *Pou5f1* gene, belongs to the DNA binding-protein family POU (Pit, Oct, Unc) (Zeineddine *et al.*, 2014). This family is known to be involved in the regulation of target genes via binding of the octamer motif, ATGCAAAT within their enhancer or promoter regions. Various studies have shown the importance of Oct4 in the maintenance of pluripotency, with a knockdown of Oct4 in mouse embryonic stem cells shown to result in the upregulation of endoderm associated genes such as *α-fetoprotein* and *Gata6* as well as an upregulation of trophoblast differentiation such as *Cdx2* (Zeineddine *et al.*, 2014). Additionally, Oct4 acts as a repressor of the expression of human ES cell placental marker, hCG (human chorionic gonadotropin). In addition to this, the three transcription factors; Oct4, SOX2 and Nanog, have been shown to co-operate in order to maintain pluripotency and self-renewal. Indeed, these transcription factors bind to the promoter of their own genes allow for their activation. In accordance with this, the transcription genes involved in ESC self-renewal; *Dppa4, Tdgf1, Oct4, Nanog and Lefty2,* are all positively regulated by Oct4, SOX2 and Nanog leading to the preferential expression in ESCs (Zeineddine *et al.*, 2014) (Zhang, 2014). The central role these transcription factors play in pluripotency maintenance makes them a specific target of interest in order to validate CLN7 and control iPSCs. Furthermore, monitoring the expression of these transcription factors, the expression of epitopes recognized via the monoclonal antibody, Tra-1-81 has been used frequently in the assessment of pluripotency status of ESCs and iPSCs (Natunen *et al.*, 2011). Although it has been proven that epitopes that are recognized by Tra-1-81, are carbohydrates, the molecular identity of these epitopes is still a mystery (Natunen *et al.*, 2011). Moreover, even though the exact molecular identity of this epitope is yet to be elucidated, it has been shown that Tra-1-81 recognizes the minimal epitope; Galβ1-3GlcNAcβ1-3Galβ1-4GlcNAc, present within human embryonic stem cells as part of the mucin-type-*O*-glycan structure. This demonstrates the validity of assessing the expression of Tra-1-81, however as the marker is recognized by cell surface antigens on pluripotent stem cells, the marker is only able to be

assessed through immunocytochemistry (Natunen *et al.*, 2011). As well as these pluripotent markers, the RNA binding protein, LIN28A was assessed due to its function in maintaining cell pluripotency. LIN28A and LIN28B loci have been shown facilitate the conversion from naïve cells to pluripotent in murine cells whilst their importance in maximal reprogramming efficiency has been previously stated. In human fibroblasts, LIN28B is activated early within reprogramming, whilst LIN28A is activated in the latter stages of reprogramming in transition to induced pluripotent stem cells (Zhang *et al.*, 2016).

Throughout validation using RT-PCR and qPCR analysis of pluripotency, neural specific and metabolic markers, CLN7 iPSCs and control iPSCs, Shef3 ESCs and human embryonic kidney 293 cells (HEK293) were also exposed to targets used. Shef3 cells were used in order to establish a positive control from which our iPSCs could be compared against, whilst HEK293s were used primarily as a negative control. HEK293 cells are one of the most widely used cell type in biological research. Despite this extensive use in research, the phenotype and karyotype still remain poorly understood (Stepanenko and Dmitrenko, 2015).

4.2.1 RT-PCR Analysis of iPSCs Demonstrate Pluripotent Properties

Initially, RT-PCR was performed in order to qualitatively assess the production of these pluripotent stem cell lineages. Once cells had reached the desired confluency (0.96-1.1 x 10^6 cells or 80-90% confluency of one well of a 6-well plate), they were dissociated using TrypLE express, cells were then lysed using Buffer RLT prior to RNA extraction and purification. Throughout the validation of the iPSCs, two CLN7 cell lines were used via the reprogramming of somatic cells from two different NCL patients provided to the McKay lab through external collaborators denoted at CLN7 466 and CLN7 474. Figure 9 (below) demonstrates the expression of pluripotent markers; OCT4, LIN28 and Nanog in CLN7 466, 474 iPSC in comparison to control iPSC as well as HEK293 and Shef3 cells. The results demonstrate the expression of pluripotency markers via RT-PCR analysis and gel electrophoresis, comparable to control counterpart, indicative of successful reprogramming to induced pluripotent state.

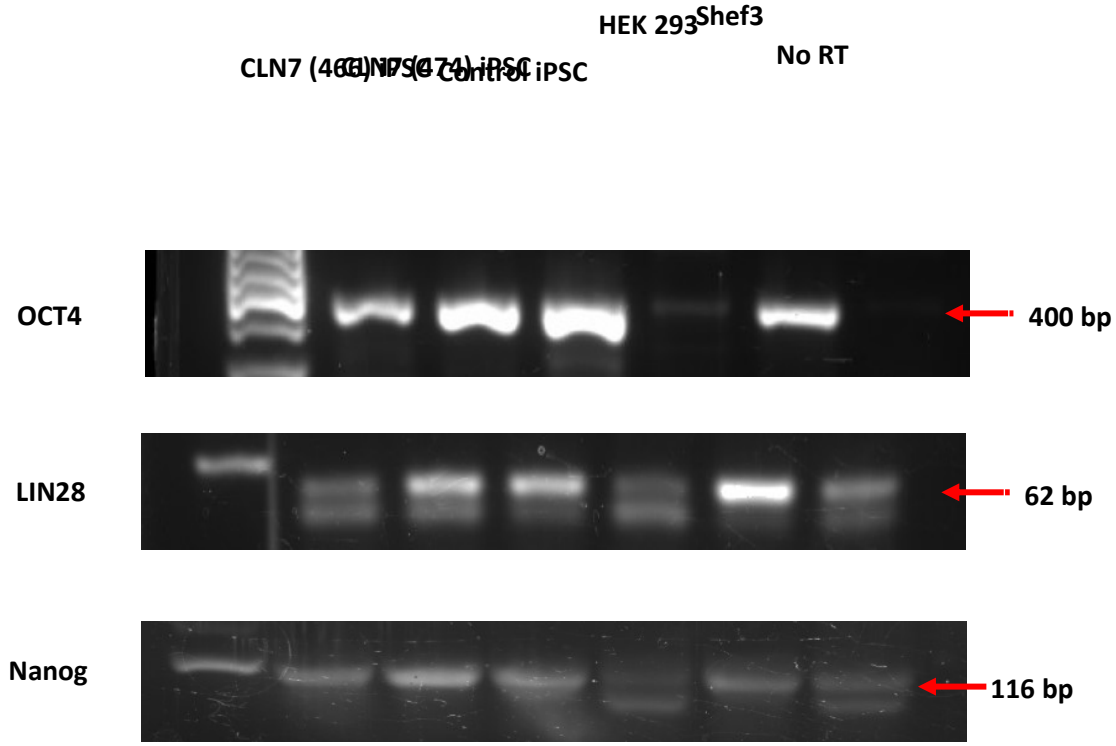

Figure 10: RT-Analysis of Pluripotency Markers in iPSCs

Figure 10. Figure depicts RT-PCR products separated by agarose gel electrophoresis (2%) supplemented with GelRed at 15V for 1 hour for qualitative analysis of Oct4, Lin28 and Nanog pluripotency markers, respectively. PCR products from two CLN7 lines as well as control were compared against that of control iPSCs and embryonic stem cells (Shef3) and HEK293 cells and No reverse transcriptase negative control (No RT).

4.2.2 Confirmation of Pluripotent Properties of CLN7 iPSCs Via Immunocytochemistry

Following RT-PCR analysis, CLN7 474 iPSC and control iPSCs were immunostained for the potency markers; SOX2, OCT4 and Tra-1-81 in order to verify our RT analysis. Pluripotent stem cells from different stages post reprogramming were fixed and stained to assess any differences in maintaining pluripotency. CLN7 474 and controls cultured on MEFs were stained for the stated potency factors as well as feeder free iPSCs of the same cell lines, this was to ensure CLN7 iPSCs were able to maintain in an undifferentiated state comparable to controls. All cells were imaged using the Leica CTR 6000 Live Cell imaging microscope. Figure 11 shows positive staining results of pluripotency markers; SOX2, Tra-1-81 and OCT4 in CLN7 iPSC compared against controls on MEFs. Images show immunocytochemistry results of CLN7 iPSCs comparable to that of controls, further indicating pluripotent properties displayed in RT-PCR results in figure 10. Furthermore, as iPSCs continued to develop towards feeder free, CLN7 and controls were stained for previously stated pluripotency markers to confirm retained pluripotency. Results display positive immunocytochemistry staining for SOX2, Tra-1-81 and OCT4 in the CLN7 474 iPSCs and control counterparts.

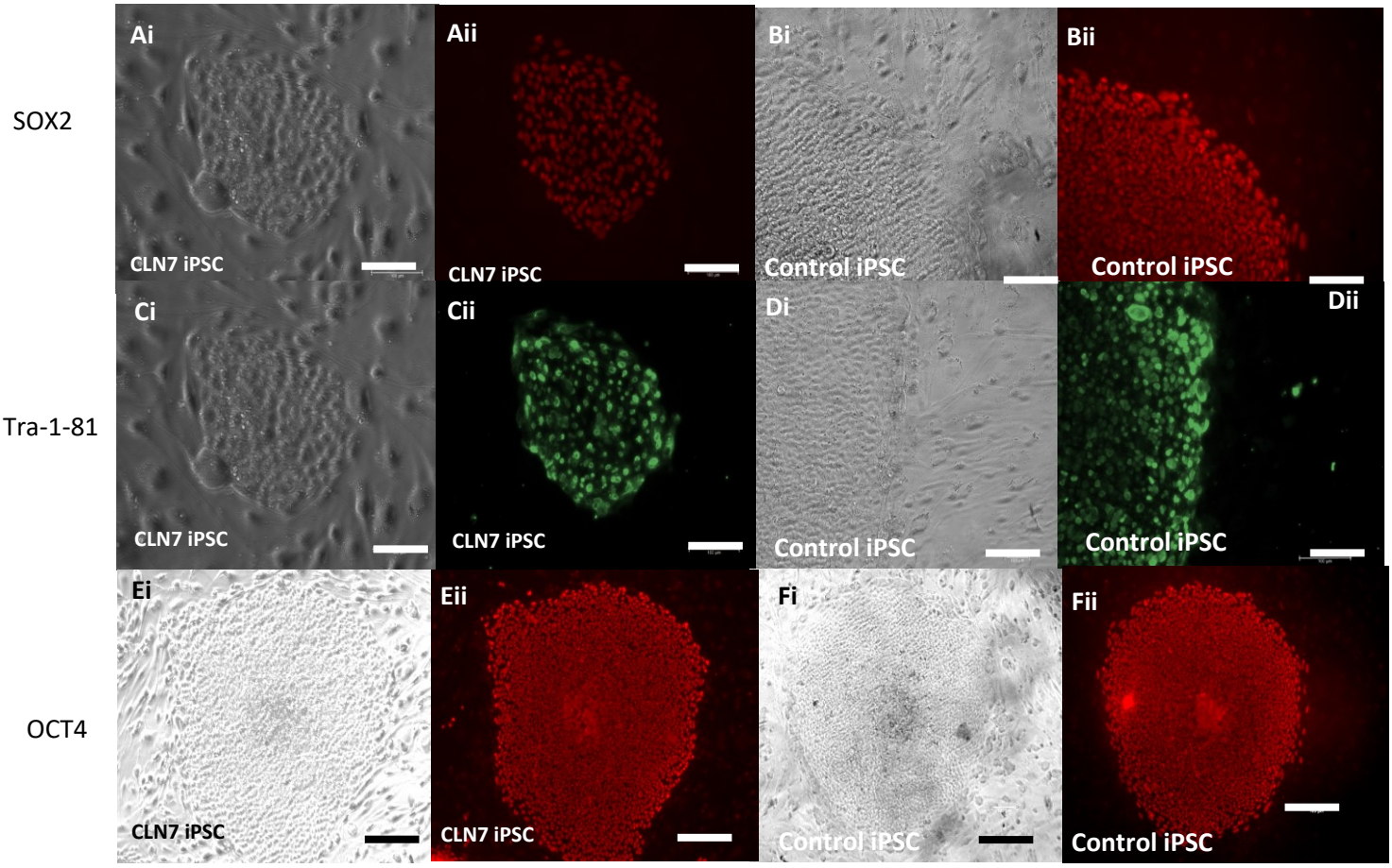

Figure 11: Immunostaining of iPSCs on MEFs

Figure 11: ICC of Pluripotency Markers in CLN7 iPSCs

Figure 11. Images depict immunocytochemistry images CLN7 474 and Control iPSCs probed for pluripotency markers SOX2, Tra 1-81 and OCT4. Images (A) display CLN7 474 iPSC on MEFs phase and emission image of SOX2 pluripotency marker at 600nm. (B) Displays control iPSC on MEFs phase and emission image of SOX2 pluripotency marker at 600nm. (C) images demonstrate CLN7 474 iPSC on MEFs phase and emission image of Tra-1-81 at 518nm. (D) images demonstrate Control iPSC on MEFs phase and emission image of Tra-1-81 at 518nm. (E) Depiction of CLN7 474 iPSC on MEFs phase and emission images probed for pluripotency marker, OCT4 at 600nm. (F) Images show control iPSC on MEFs, phase and emission images probed for pluripotency marker, OCT4 at 600nm. All images shown at x20 magnification, with 100µm scale bar.

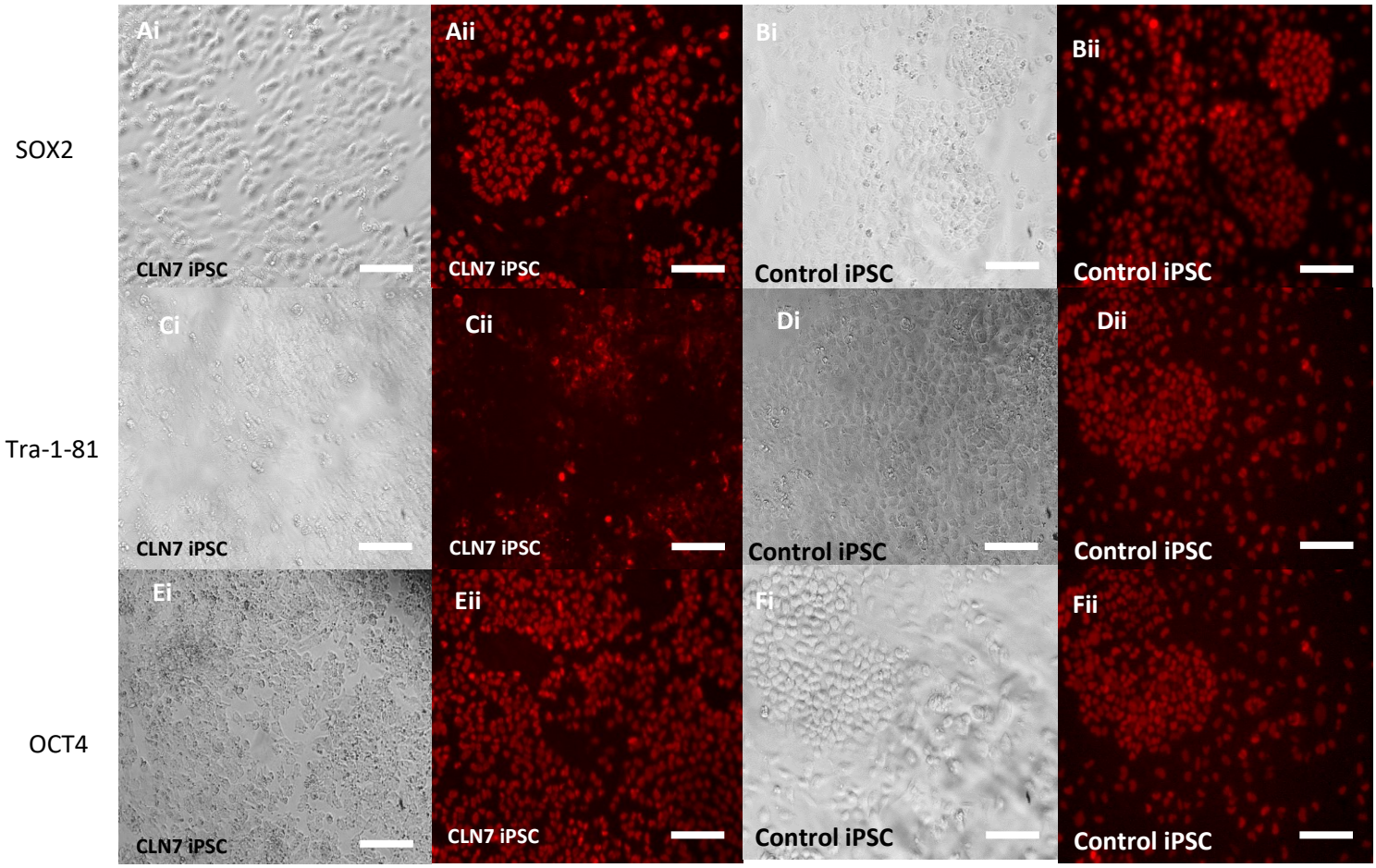

Figure 12: Immunostaining of Feeder Free iPSCs

Figure 12: ICC of Pluripotency Markers in Feeder Free CLN7 iPSCs

Figure 12. Images depict immunocytochemistry images CLN7 474 and Control iPSCs probed for pluripotency markers SOX2, Tra-1-81 and OCT4. Images (A) display feeder free CLN7 474 iPSC phase and emission image of SOX2 pluripotency marker at 600nm. (B) Displays control feeder iPSC phase and emission image of SOX2 pluripotency marker at 600nm. (C) images demonstrate feeder CLN7 474 iPSC phase and emission image of Tra-1-81 at 518nm. (D) images demonstrate feeder free Control iPSC phase and emission image of Tra-1-81 at 518nm. (E) Depiction of feeder free CLN7 474 iPSC phase and emission images probed for pluripotency marker, OCT4 at 600nm. (F) Images show feeder free control iPSC, phase and emission images probed for pluripotency marker, OCT4 at 600nm. All images shown at x20 magnification, with 100µm scale bar.

4.3 Analysis of CLN7 and Control iPSCs Show Negligible Differences in Metabolism

Following confirmation of successful generation of patient and control induced pluripotent stem cell lines, a variety of target genes were chosen in order to deduce any differences in metabolic profile of CLN7 iPSCs as well as subsequent differentiated NPCs (4.5) compared to that of controls. It was imperative to deduce the metabolic profile of CLN7 iPSCs in order to ascertain key changes that occur during differentiation and to confirm our hypothesis of a shift from oxidative phosphorylation of iPSCs to glycolysis in NPCs and more mature neuronal cells.

Metabolic markers; NFκB1, HO-1, PKM2, LDHA, HO-1, and UCP2 were investigated in order to deduce any metabolic shifts.

Figure 13 (below) demonstrates the relative expression of various markers related to inflammation and metabolism in CLN7 iPSCs compared to control iPSCs as well as Shef3 embryonic stem cells and HEK293 cells. The purpose is to ascertain key differences in metabolic traits of CLN7 and controls in the early stages of differentiation, in order to discern any differences as differentiation progresses. Our results show that there was no statistical significance between the relative expression of the inflammatory marker NFκB, in CLN7 iPSCs when compared to controls. There was also no statistical difference between the two iPSC lines and Shef3. The oxidative stress marker, HO-1, also demonstrated no statistical significance between the relative expression of CLN7 iPSCs and control iPSCs. However, it was found that both the iPSC lines showed a statistical difference in expression when compared to Shef3 cells, with an decrease in relative expression of 17-fold in Shef3 compared to control iPSC and 16.6-fold decrease in relative expression when compared to CLN7 iPSCs. CLN7 iPSCs demonstrated a significant increase in expression of glycolytic enzyme, PKM2 compared to both control iPSCs and Shef3 with a 4.3-fold and 5.4-fold increase in relative expression, respectively. No statistically significant difference was found between the relative expression of LDHA in CLN7 and control iPSCs, however, Shef3 displayed a 5-fold increase in relative expression compared to CLN7 iPSCs, determined to be statistically significant. The expression of UCP2 was significantly decreased in both

CLN7 iPSCs and Shef3 cells when compared to control iPSCs, with a decrease in relative expression of 14.9-fold and 20-fold respectively. There was no statistical difference in the relative expression of UCP2 in CLN7 iPSCs and Shef3 cells.

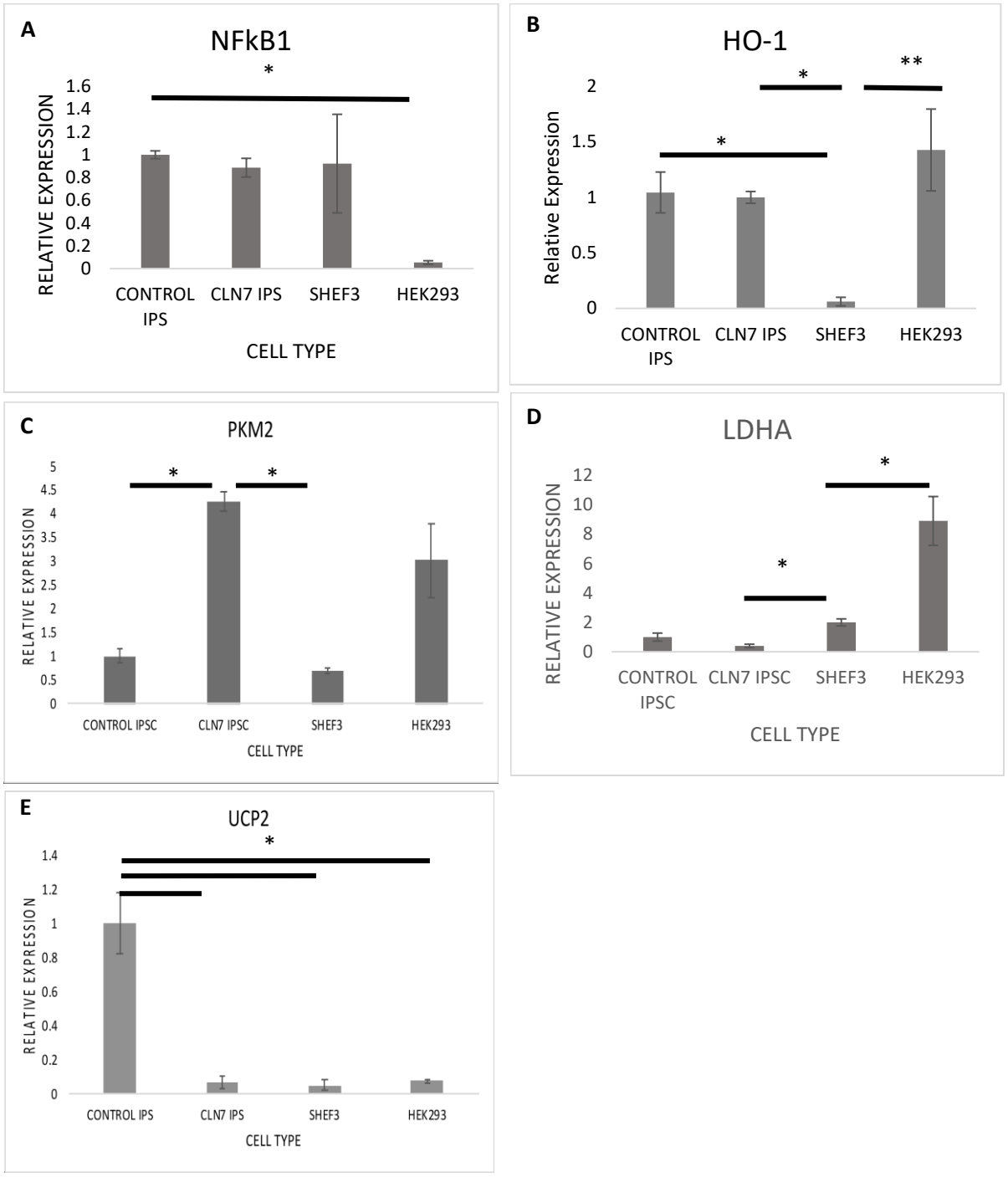

Figure 13: Metabolic Changes in CLN7 iPSCs Compared to Controls

Figure 13: Metabolic qPCR targets of iPSCs

Figure13: Differential expression of (A) NFκB, (B) HO-1, (C) PKM2, (D) LDHA, (E) UCP2 (n=3, three technical repeats) between CLN7 iPSCs against healthy iPSC as well as SHEF3 positive ESC controls and HEK293s. Subsequently, single factor ANOVAs were performed with post-hoc Tukey analysis performed in order to determine statistical significance between groups. Statistical differences were as followed; (A) No statistical differences between CLN7 iPSC and Control iPSCs, both iPSC types displayed no statistical difference to SHEF3 cells. A value of p=0.034 between Shef3 and HEK293s displaying significance. (B) No statistical differences between CLN7 iPSC and Control iPSCs were calculates. A value of p=0.026 was calculated between control iPSCs and SHEF3, whilst CLN7 iPSCs also displayed significant differences with a p=0.021 calculated. Shef3 cells and HEK293s share a strong significance calculated at p=0.007. (C) Control iPSC displayed significant differences to CLN7 iPSC with a p=0.048 calculated, whilst CLN7 iPSCs all displayed significant differences to Shef3 cell with a p=0.047 calculated. (D) CLN7 iPSCs displayed significant differences in expression when compared to both Shef3 and HEK29, with p-values of p=0.026 and p=0.038 calculated, respectively. (E) Control iPSCs displayed significant differences between each cell type with a p value of p=0.034, p=0.045 and p=0.039 respectively. Subsequently, error bars are calculated based on the standard error mean (SEM) of each sample.

4.4 Neural Differentiation and Specification

4.4.1 Neural Differentiation

Following successful reprogramming of NCL patient and healthy somatic cells to induced pluripotent stem cells, a neural differentiation protocol developed within the McKay lab was implemented in order to produce viable neural progenitor cells and neurons in order to successfully observe phenotypic changes of during neural development. In order to initiate neural differentiation, feeder free patient CLN7 and control iPSCs were subjected to a stepwise protocol which allowed for the minimization of induction of exogenous growth factors, thus encouraging differentiation of neuroectoderm. Figure 14 (below) demonstrates the sequential steps during neural differentiation. At day 0 feeder free CLN7 and control iPSCs were enzymatically dissociated through the use of TrypLE express and re-suspended in neural induction media containing enhanced FGF2 levels of 20ng/mL (see table 5). Within 24 hours neuroepithelial-like clusters (NECs) formed with highly proliferative characteristics. Following the formation of these epithelial clusters, on day 6, NECs were replated onto laminin coated plates until formation of neural rosettes. Following this, neural rosettes were disturbed using a 12-gauge syringe and once again replated until a neural progenitor cell monolayer formed. Once an NPC monolayer had fully formed and reached a desired confluency, cells were trypsinised, centrifuged and replated onto laminin coated dishes, resuspended in neural maturation media for terminal differentiation. Cells required a half media change every three days until formation of neurons.

Figures 15 and 16 demonstrate magnified images of the stages of neural differentiation outlined above, from maintain feeder free iPSCs to NPC monolayer formation. Both figures outline the same time points and stages categorized throughout (A-F) in CLN7 iPSCs (figure 15) and control iPSCs (figure 16). (A) 10x magnified image of maintenance of feeder-free iPSCs. (B) 20x magnified image of neuroepithelial layer. (C) neural rosette formation. (D) the expansion of neural progenitor cells as neurospheres. (E,F) monolayer formation and expansion of neural stem/progenitor cells.

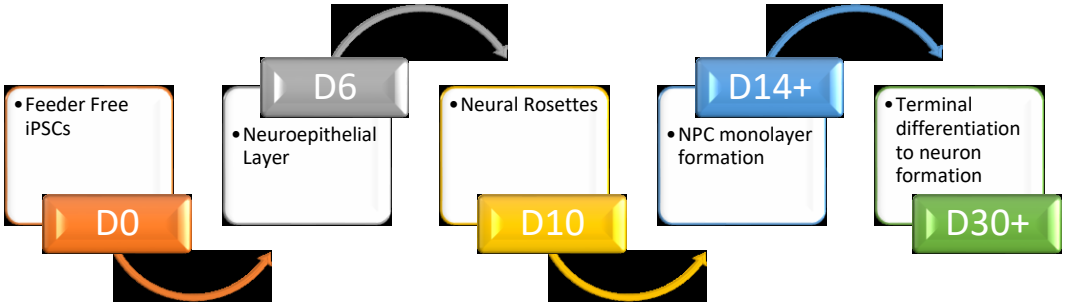

Figure 14: Neural Differentiation Protocol

Figure 14. A schematic depiction, demonstrating the stepwise protocol for neural differentiation.

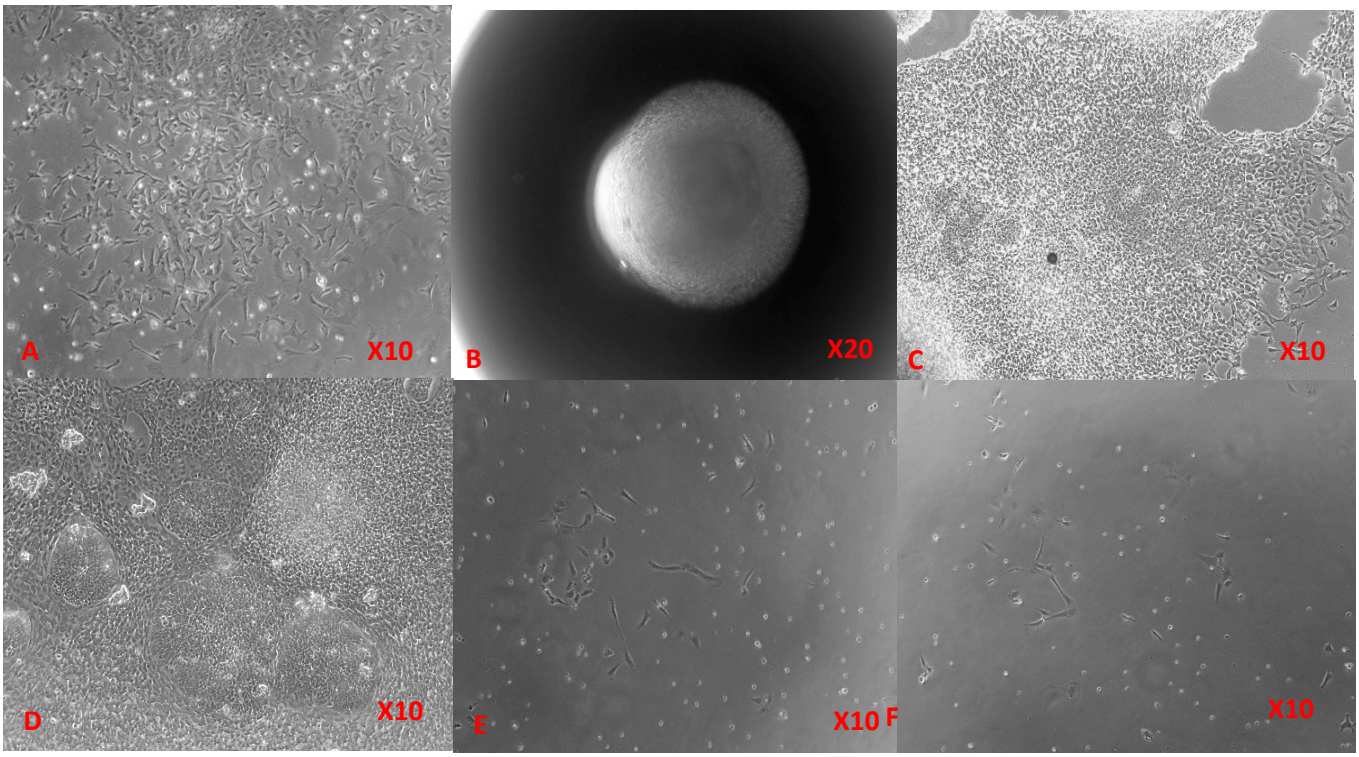

Figure 15: Stepwise neural differentiation of CLN7 patient iPSCs in vitro

Figure 15. Figure represents neural differentiation of CLN7 iPSCs.

(A) Feeder free iPSCs maintained in mTESR on matrigel covered plates, D0. **(B)** Increased magnification of neuroepithelial cells in suspension, d6. **(C)** Cells move towards formation of neuroepithelial rosettes cultured on laminin-coated plates, D7-10. **(D)** Expansion of neural progenitor cells in suspension as neurospheres. **(E, F)** Neural progenitor cells trypsinised and re-plated at a seeding density of ~50,000 cells, to move towards terminal differentiation.

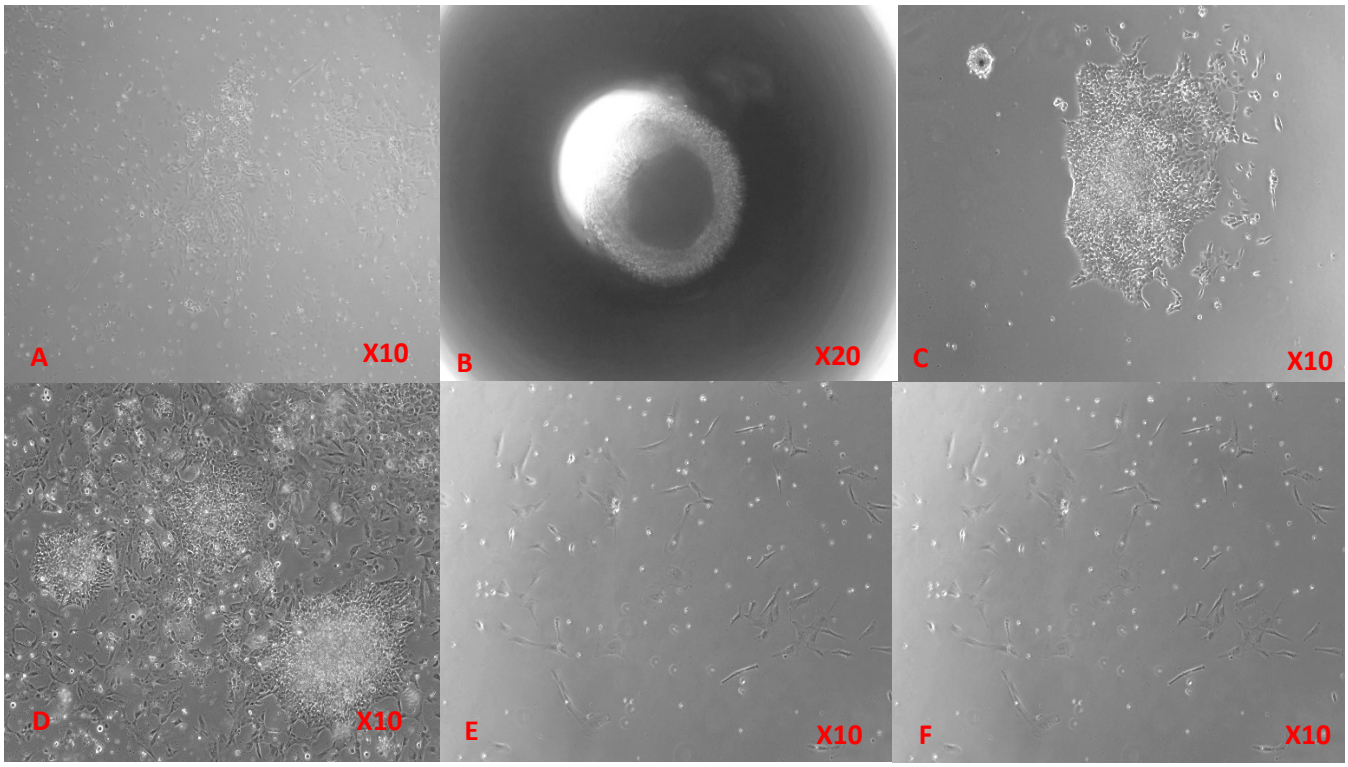

Figure 16: Stepwise neural differentiation of Control iPSCs in vitro.

Figure 16. Figure represents neural differentiation of Control iPSCs.

(A) Feeder free iPSCs maintained in mTESR on matrigel covered plates, D0. **(B)** Increased magnification of neuroepithelial cells in suspension, d6. (**C)** Cells move towards formation of neuroepithelial rosettes cultured on laminin-coated plates, D7-10. **(D)** Expansion of neural progenitor cells in suspension as neurospheres. **(E, F)** Neural progenitor cells trypsinised and re-plated at a seeding density of ~50,000 cells, to move towards terminal differentiation

4.4.2 CLN7 and Control NPCs Exhibit Loss in Pluripotent Markers and an Increase in Nestin

Following qualitative assessment of induced pluripotent stem cells, as well as qPCR analysis of various metabolic genes, quantitative PCR was implemented for further validation of the iPSCs using potency markers Sox2 and Lin28. This assessment also allowed for the comparison of differing potency markers for NCL patient lines (CLN7) in comparison to their wildtype counterparts, whilst allowing to compare against differentiated NPCs in order to validate successful differentiation towards NSCs/NPCs.

The protein Nestin is expressed extensively in the NPCs of normal adult brains and is said to be replaced by other neuron specific protein upon differentiation towards neuronal cells (Hendrickson *et al.*, 2011). Nestin is distributed within neural progenitor cells of the sub-ventricular zone of the lateral ventricle as well as within the subgranular zone of the denate gyrus as (Hendrickson *et al.*, 2011). The apparent presence of nestin within neuronal progenitor cells, whilst deregulated in neurons makes it an ideal target for identification of successful differentiation towards NPCs. Therefore, this made the gene a prime target as to confirm our cells as NPCs in conjunction with the loss of pluripotency markers.

Figures 17 and 18 (below) depict the differential expression of the pluripotency markers SOX2 and LIN28A in CLN7 and control NPCs in comparison with iPSC counterparts as well as Shef3 and HEK293 controls. Both figures show a statistically significant decrease in both pluripotency markers in CLN7 and control NPCs compared to their iPSC counterparts, with CLN7 iPSCs displaying a 73-fold increase in LIN28A expression and an 8-fold increase in SOX2 expression compared to NPC counterparts. Control iPSCs display a 46-fold increase in LIN28A expression and 173-fold increase in SOX2 expression when compared to NPC counterpart. In conjunction, figure 18 depicts the differential expression of neural stem/progenitor cell marker, Nestin. Figure 19 shows a significant increase in expression of the marker in both CLN7 and control NPCs compared to their iPSC counterparts, with a 15.5-fold and 3.7-fold increase in Nestin expression in control NPCs and CLN7 NPCs, respectively, compared to iPSC counterparts.

Expression of genes was determined via the implementation of relative expression. This method determines expression through comparing Ct values of target cells normalized to housekeeper, in our case PABC4 via ΔCT (mean of target CT – mean of housekeeper CT). The normalized Ct values are converted to relative expression utilizing the formula $2^{\Delta\Delta CT}$ with the values expressed relative to those of control iPSCs.

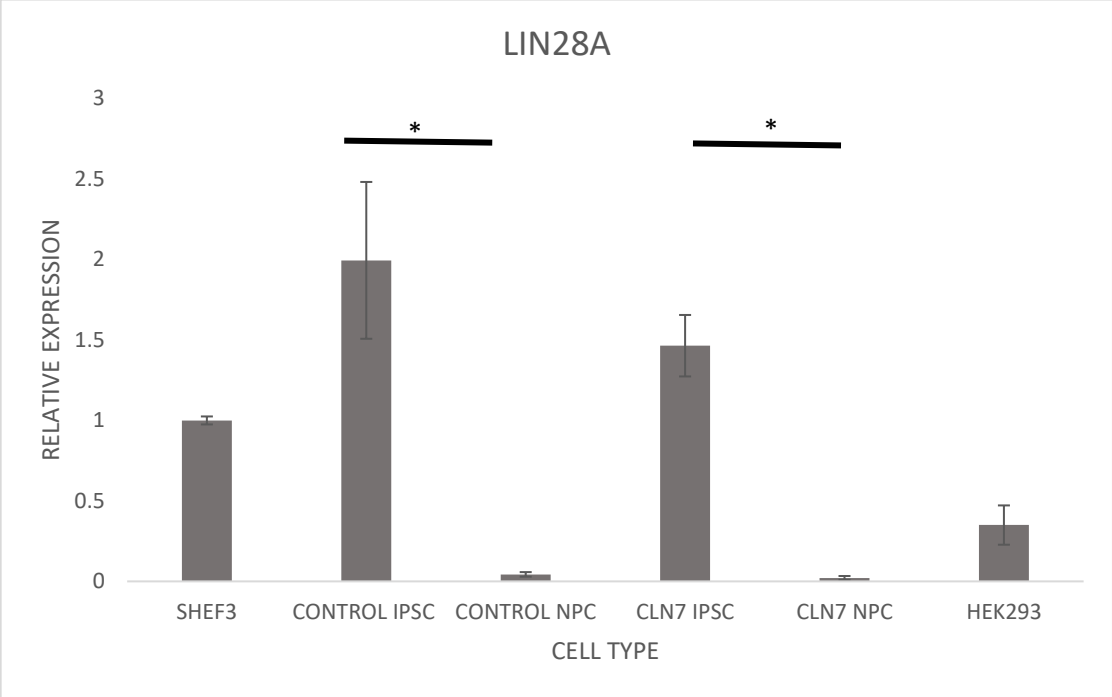

Figure 17: LIN28A qPCR Analysis in iPSCs and NPCs

Figure 17. Differential expression of LIN28A between CLN7 and Control iPSCs in comparison to neural progenitor cell counterparts as well as Shef3 embryonic stem cells and HEK293 cells. Relative expression was determined of CLN7 iPSCs against control cell. Subsequently single factor ANOVAs were performed with post-hoc Tukey analysis performed in order to determine statistical significance between groups. Analysis performed calculated a statistical difference between control iPSC and control NPC groups of p=0.025, with CLN7 iPSC and CLN7 NPC displaying a significance of p=0.049. The graph depicts the relative expression of three biological repeats with each repeat also involving three technical repeats. Subsequently, error bars are calculated based on the standard error mean (SEM) of each sample.

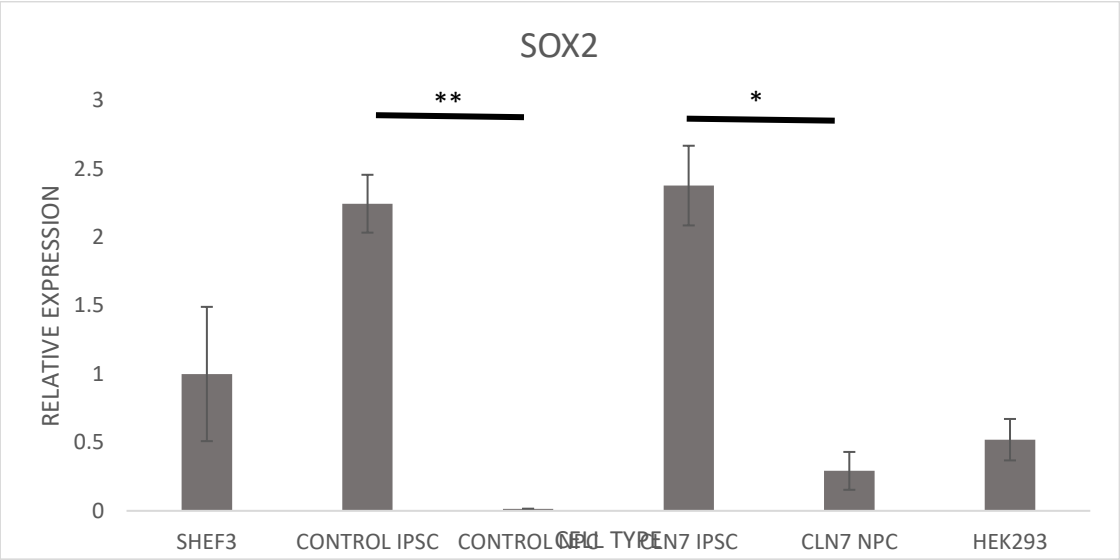

Figure 18: SOX2 qPCR Analysis in iPSCs and NPCs

Figure 18. Differential expression of SOX2 between CLN7 and Control iPSCs in comparison to neural progenitor cell counterparts as well as Shef3 embryonic stem cells and HEK293 cells. Relative expression was determined of CLN7 iPSCs against control cell. Subsequently, single factor ANOVAs were performed with post-hoc Tukey analysis performed in order to determine statistical significance between groups. Analysis performed calculated a statistical difference between control iPSC and control NPC groups of p=0.008, with CLN7 iPSC and CLN7 NPC displaying a significance of p=0.028 The graph depicts the relative expression of three biological repeats with each repeat also involving three technical repeats. Subsequently, error bars are calculated based on the standard error mean (SEM) of each sample.

NESTIN

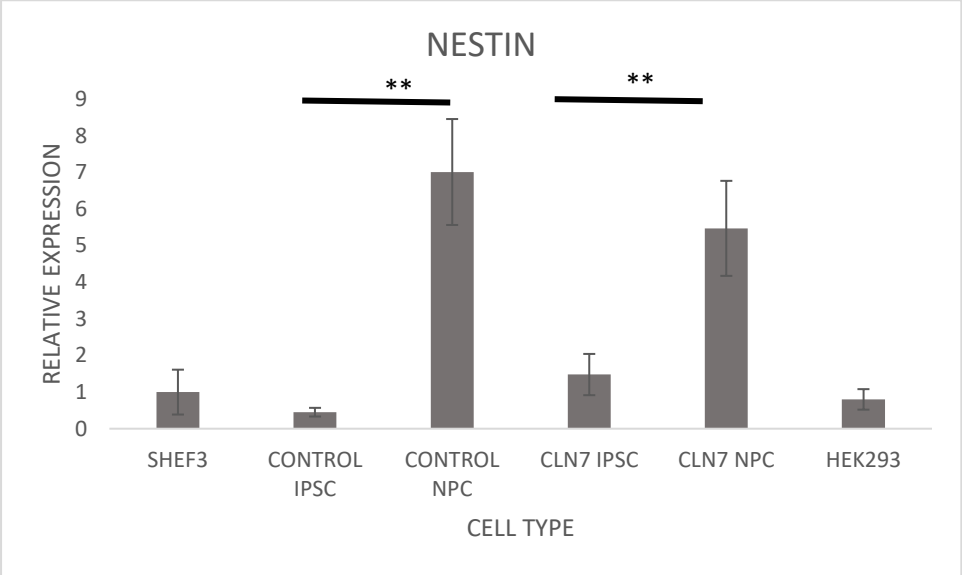

Figure 19: Nestin qPCR Analysis in iPSCs and NPCs

Figure 19. Differential expression of Nestin between CLN7 and Control iPSCs in comparison to neural progenitor cell counterparts as well as Shef3 embryonic stem cells and HEK293 cells. Relative expression was determined of CLN7 iPSCs against control cell. Subsequently, single factor ANOVAs were performed with post-hoc Tukey analysis performed in order to determine statistical significance between groups. Analysis performed calculated a statistical difference between control iPSC and control NPC groups of p=0.004, with CLN7 iPSC and CLN7 NPC displaying a significance of p=0.002 The graph depicts the relative expression of three biological repeats with each repeat also involving three technical repeats. Subsequently, error bars are calculated based on the standard error mean (SEM) of each sample.

The evident increase in expression of neural stem/progenitor cell marker, Nestin, in the CLN7 and control NPCs compared to iPSCs, whilst the expression of potency markers; SOX2 and LIN28A decreased, suggests successful differentiation to neural progenitor/stem cells. Our results show statistical significance in each target between our CLN7 and control NPCs with their corresponding iPSC cell line. Quantitative PCR was performed on the NPCs in order to ascertain any differences in metabolism. As previously aforementioned, iPSCs show negligible differences in metabolism, however, previous data has suggested that no phenotypic differences have been observed between CLN7 iPSCs and controls, with hypothesized disparities expected as the neural differentiation pathway continues.

4.5 CLN7 NPCs Show A Metabolic Shift Towards Glycolysis

We hypothesized that the neural progenitor cells of CLN7 would show a change in metabolic modality. Current literature shows that healthy NPCs move towards oxidative phosphorylation (OXPHOS) in order for complete differentiation towards neurons, which rely completely on OXPHOS to meet energy requirements. OXPHOS has been shown to cause an increase in oxidative stress through the increase in ROS production through oxygen free radicals, this led to the introduction of the human oxygenase (HO-1) marker to be implemented. HO-1 is an oxidative stress marker prevalent in circumstances of increased ROS production. ATP synthase is known to be the main energy source of metabolic pathways, with the marker relating to the fifth multi subunit OXPHOS complex. The enzyme synthesizes ATP derived from ADP within the mitochondrial matrix, utilizing energy provided by the proton electrochemical gradient. (Jonckheere, Smeitink and Rodenburg, 2012). Upregulation of ATP synthase relates to an increase in OXPHOS. In conjunction to this, an upregulation of Mitochondrial uncoupling protein 2 (UCP2) relates to an increase in OXPHOS. UCP2 is a member of the anion carrier proteins, the carriers are able to facilitate the transfer of anions from the inner mitochondrial membrane and the return transfer of protons from the outer to the inner mitochondrial membrane (Sreedhar *et al.*, 2017).

Moreover, the shift towards glycolysis was of great interest in the project as a shift towards this metabolic state would indicate cell dysfunction leading to less efficient energy production. The markers GLUT1, PKM2 and LDHA are all required in the various steps of glycolysis. Glucose Transporter 1 (GLUT1) is a uniporter protein found within mammalian cells that facilitates the transport of glucose across the plasma membrane and has been shown to regulate cell glycolysis in prostate cancer (Xiao *et al.*, 2018). The pyruvate kinase muscle isozyme M2 (PKM2) is a glycolytic limiting enzyme which catalyzes the final step in glycolysis of the transphosphorylation between phosphoenolpyruvate and adenosine diphosphate resulting in the formation of ATP and pyruvate (Dong *et al.*,

2016). The protein encoded by the LDHA gene catalyzes the conversion of L-lactate and NAD^+ to pyruvate and NADH in the final step of glycolysis, a key component in the regulation of glycolytic pathway (Jin *et al.*, 2017).

Inflammation of neuronal cells and NPCs has been shown to lead to a variety of neurodegenerative diseases. In order to ascertain whether there is an upregulation of inflammation in CLN7 NPCs and iPSCs, qPCR analysis of the NFkB1 pathway was undertaken. The nuclear factor, NFkB pathway has been shown to be a prototypical proinflammatory pathway due to its role in the expression of proinflammatory genes such as adhesion molecules, cytokines and chemokines (Lawrence, 2009).

Figure 20 (A-F) (below), demonstrates alterations in the metabolic profile of CLN7 NPCs compared to controls. CLN7 NPCs show an increase in expression of inflammatory marker, NFκB, with an increase in relative expression of 1.54-fold. A shift towards glycolysis is implied via the results as the glycolytic enzyme, PKM2, demonstrates an increase by 2.1-fold in relative expression in CLN7 NPCs compared to controls. Moreover, there is an increase in the relative expression in both ATP synthase and GLUT, with a 10.6-fold and 16.2-fold increase, respectively. The results indicate changes in oxidative stress and the antioxidant response in CLN7 NPCs, with 7.8-fold increase in the relative expression of SIRT1 in CLN7 NPCs compared to controls, however, there was decrease in expression of oxidative stress marker, HO-1. Control NPCs demonstrated a 5.9-fold increase in expression of HO-1 compared to CLN7 NPCs. All results obtained show statistical significance of $p<0.05$ (see legend).

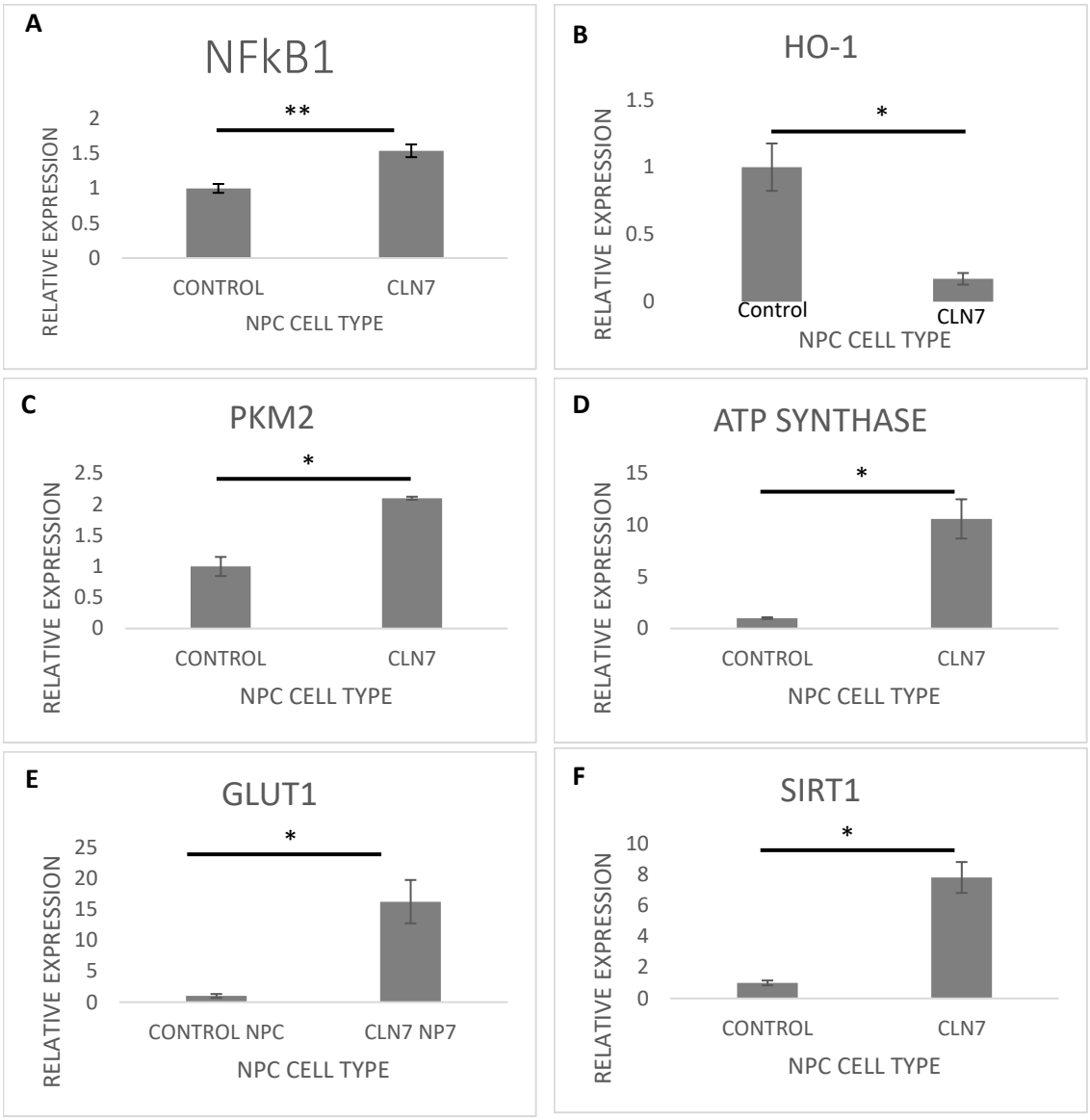

Figure 20: Metabolic Targets in NPCs

Figure 20. Differential expression of (A) NFκB, (B) HO-1, (C) PKM2, (D) ATP Synthase, (E) GLUT1 and (F) SIRT1 (n=3, three technical repeats) between CLN7 neural progenitor cells (NPCs) against healthy controls. Subsequently, Independent T-Tests were performed in order to determine statistical significance between the two cell types, with the following p values calculated; (A) p=0.008, (B) p=0.04, (C) p=0.02, (D) p=0.03, (E) p=0.04, (F) p=0.02. Subsequently, error bars are calculated based on the standard error mean (SEM) of each NPC sample.

Table 19: Summation of Gene Expression of Metabolic Targets in NPCs.

Target	Relative Expression of CLN7 NPCs compared to normalized control NPCs	Significance
NFκB	1.54	P=0.008
Ho-1	0.17	P=0.04
PKM2	2.1	P=0.02
ATP Synthase	10.6	P=0.03
GLUT1	16.2	P=0.04
SIRT1	7.8	P=0.02

4.6 CLN7 NPCs Show a Decrease in Autophagic Flux

The antibody p-p70 was normalized to p70 in order to provide an insight into the fold change in the upregulation of activated p70 in NPCs. As stated previously, accumulation of p62 is indicative of impaired autophagy. The protein, p70 is a downstream target of the mammalian target of rapamycin complex 1 (mTORC1) which is phosphorylated upon activation of the pathway. The mTORC1 pathway has been shown to be intrinsically linked to autophagy, with an upregulation in mTORC1 resulting in a downregulation of autophagy. An accumulation of p70 and activated p-p70 is indicative of alteration in autophagic flux.

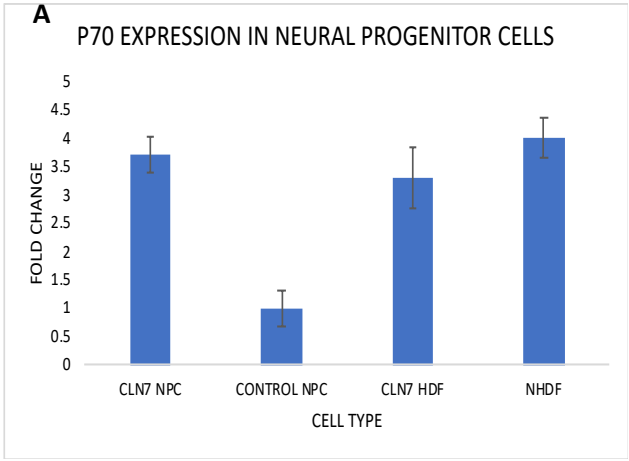

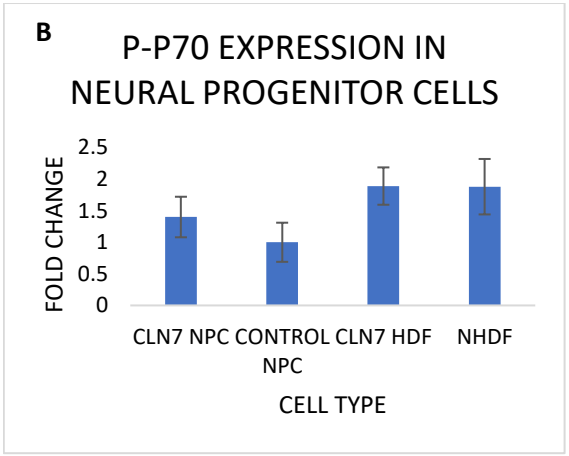

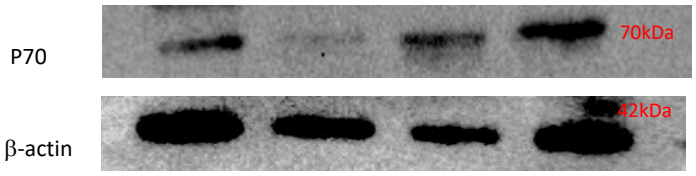

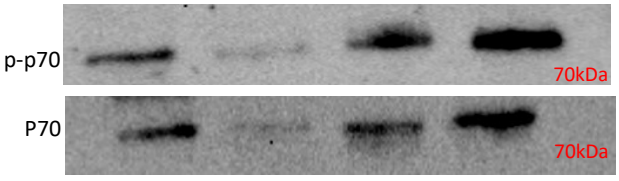

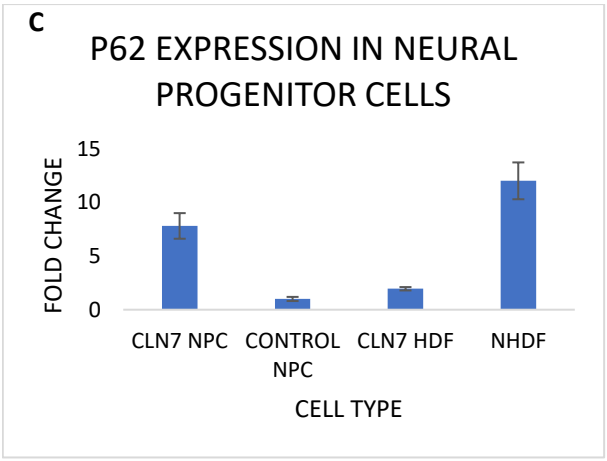

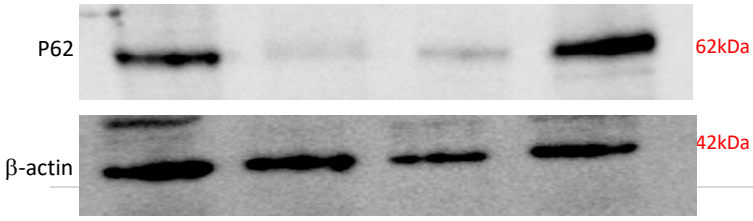

Figure 21: Western Blot analysis of autophagy related proteins to monitor changes of autophagic flux in CLN7 NPCs compared to Controls

Figure 21: Western Blot Analysis of Autophagic flux in CLN7 NPCs compared to Controls, Figure 42. Western blot analysis of changes in (A) P70 normalised to β-actin housekeeper, (B) p-p70 with expression normalised against p70 and (C) p62 normalised to β-actin housekeeper. 20µg of each sample was loaded and electrophoresed along a 10% SDS-PAGE acrylamide gel at 90v for 1.5-2 hours. Figure represents densitometry analysis of western blots performed via Image J. Results show normalised expression to β-actin/p70 (stated), from which fold change was calculated in CLN7 neural progenitor cells relative to Control NPCs as well as analysis of CLN7 HDF and NHDF controls. The image represents western blot experiment carried out with three technical repeats for quality control purposes.

Figure 21 (A-C) demonstrates the accumulation of proteins related to an impairment of autophagy in CLN7 NPCs compared to control NPCs. Analysis was conducted against CLN7 HDFs and control nHDFs in order to ascertain any differences in accumulation of target proteins as differentiation progresses. Western blot analysis shows a 3.8-fold increase in mTOR target, p70, in CLN7 NPCs compared to control NPCs. However, CLN7 HDFs and nHDFs show little differences in p70 expression between each other, with a 3.3-fold and 4-fold increase respectively. Phosphorylated p70 (p-p70), displays a 1.4-fold increase in expression in CLN7 NPCs compared to controls, whereas CLN7 HDFs and nHDFs displayed a near identical expression, with a fold increase of 1.89 and 1.88 respectively. Impairment of autophagy has been linked to increased p62 accumulation, our results show a 7.8-fold increase in p62 levels in CLN7 NPCs compared to those of control counterparts, conversely, CLN7 HDFs show a decrease in p62 levels compared to nHDFs with a fold-change of 1.95 and 12, respectively, obtained.

The results are indicative of an accumulation of proteins intrinsically linked with impaired autophagy and defective lysosomal breakdown in neural progenitor cells. The results also indicate that this is not apparent in HDF CLN7 cell when compared against healthy controls, suggesting that changes in autophagic flux are only observable the further down the differentiation pathway, as with observing changes in metabolic shift.

4.7 Terminal Differentiation of CLN7 474 NPCs

Once patient CLN7 and control cells had differentiated into neural progenitor cells, they underwent terminal differentiation on laminin coated plates. There are current issues with neural differentiation in obtaining both high yield and purity of neurons due to various factors with neural differentiation protocol robustness. Due to extenuating circumstances, issues arose when terminally differentiating both CLN7 and control NPCs. Due to this, only CLN7 474 NPCs were able to terminally differentiate to neurons. The cells were cultured for a further 28 days in neural maturation media until mature neurons had formed. Figure 21 (below) depicts microscopic image at magnification of x10 of initial formation of CLN7 neurons derived from CLN7 474 neural stem/progenitor cell via neural differentiation protocol.

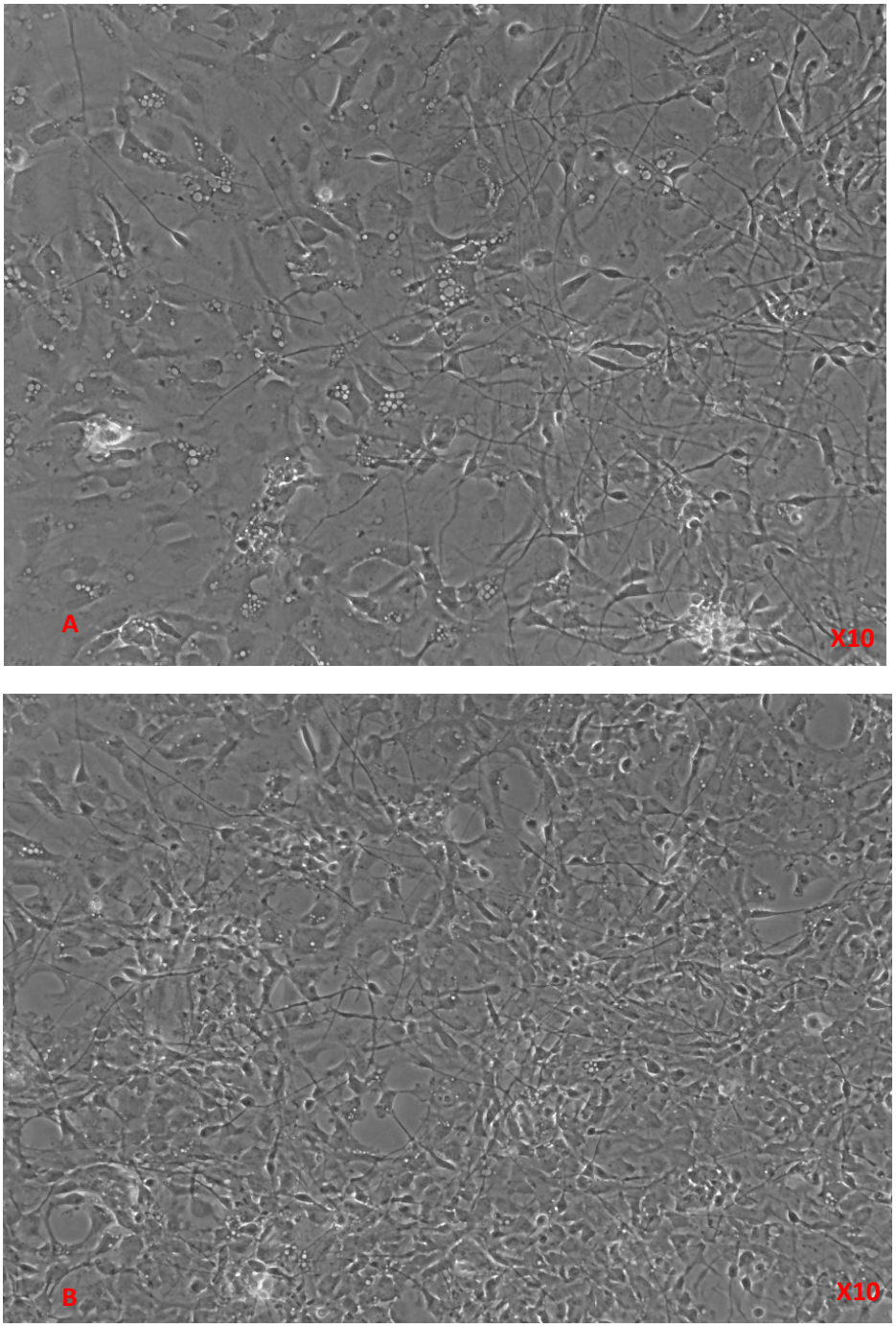

Figure 22: Terminal differentiation of CLN7 patient NPCs derived from iPSCs.

Figure 22. Figure depicts final stage of neural differentiation protocol of CLN7 NPCs.

(A,B) Images taken of CLN7 derived neurons produced through a stepwise neural differentiation protocol. NPCs were seeded at a density of ~50,000 cells and cultured on laminin-coated plates in neural maturation media until formation of mature neuronal cells.

4.7.1 CLN7 Neurons Exhibit Accumulation of Autophagic Related Proteins

Immunocytochemistry was implemented in order to assess p62 and LAMP1 accumulation within neuronal vesicles as well as known neural marker, β-III-Tubulin, and mitochondrial marker, Mitotracker Red. Cells were also incubated with DNA stain, DAPI, in order to visualize nucleus of the neuronal cells. Images shown below are that of CLN7 patient derived neuronal cells due to technical issues in terminal differentiation of controls. Immunocytochemistry was performed on neurons utilizing the Autophagic markers p62 and LAMP1. Lysosomes acts as degradation hubs for autophagic and endocytic components in order to maintain cellular homeostasis, essential for neuronal cell survival and function (Huynh *et al.*, 2007). LAMP1 is distributed throughout autophagic and endolysosomal organelles and is degraded upon activation of autophagic pathways. LAMP1 is routinely used as am autophagic marker, with an accumulation of the protein related to impaired autophagy (Eskelinen, 2006). The presence of the protein within the CLN7 neurons is an indicator of autophagic arrest. As well as LAMP1, the protein p62 has been established as a marker of impaired autophagy through extensive studies. The protein acts as a receptor for autophagy and a scaffold for the degradation of ubiquitin cargos. Although the protein aids in the delivering of deleterious products to autolysosomes for degradation, p62 itself is also degraded during the process (Katsuragi, Ichimura and Komatsu, 2015). An accumulation of the protein within neuronal peripherals has been used in previous research as an autophagic impairment marker.

Figures 23 and 24 demonstrate ICC staining of CLN7 474 neurons, probed for p62 (red) and LAMP1 (green). Images show accumulation of p62 within the vesicles of the neurons and LAMP1 in the axons of the neurons, indicative of accumulation and storage of autophagy related proteins within the patient neurons. With neurons stained with nuclear stain, DAPI (blue) in order to visualize nuclei of the various neuronal cells.

B-III-tubulin is a member of the tubulin family and is one of the two core protein families (alpha and beta tubulins) that is able to heterodimerize and assemble to form microtubules (Katsetos *et al.*, 2003). The protein has

been established to be expressed is neurons primarily and involved in neurogenesis and axon guidance with maintenance properties (Dráberová *et al.*, 2008). Immunocytochemistry utilizing this marker was imperative in order to confirm successful differentiation to neurons.

Figure 26 depicts ICC staining for B-III-tubulin in CLN7 474 neurons. The image shows positive staining result (red) within the axons of the neurons, a good indication of successful differentiation to neurons from neural stem/progenitor cells.

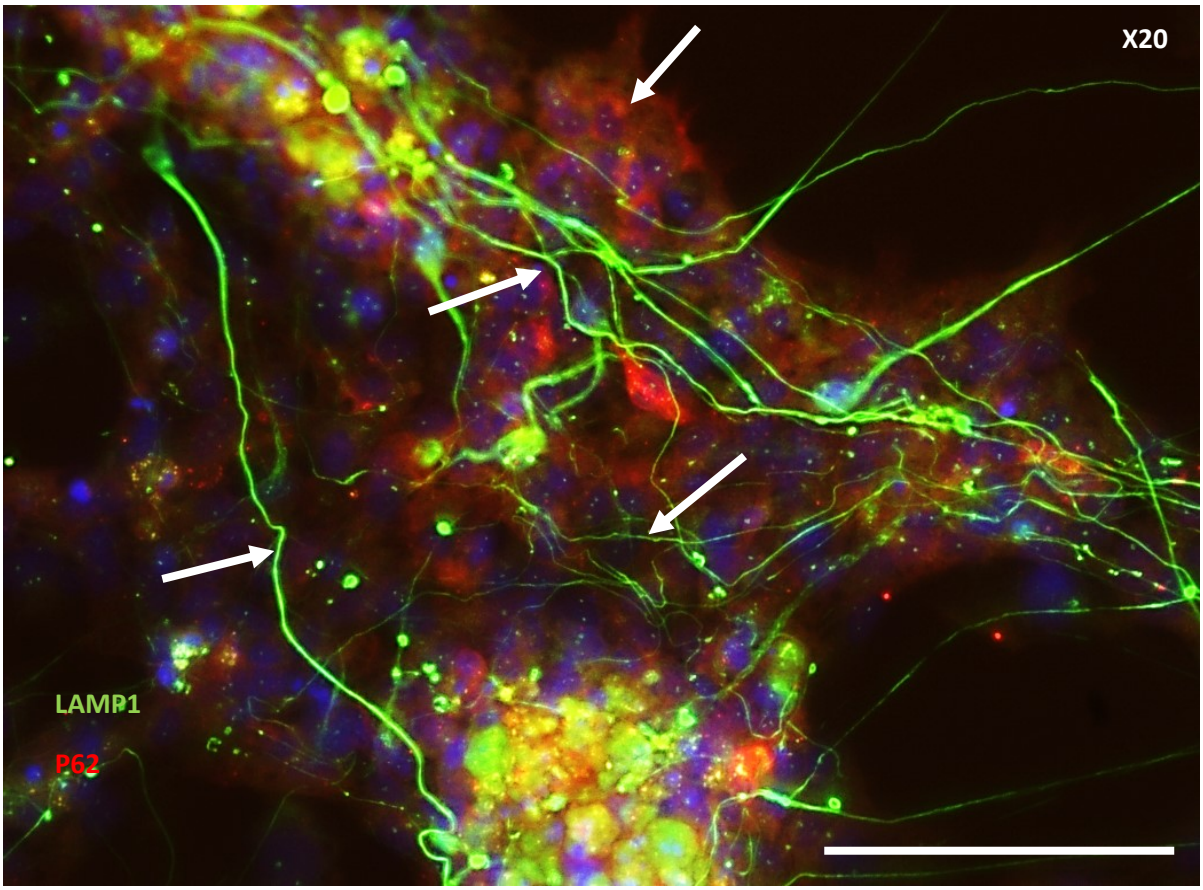

Figure 23: CLN7 Neuronal Cells ICC Dual Stain of p62 and LAMP1:

Figure 23. Immunocytochemistry image produced depicts CLN7 neurons developed through terminal differentiation of neural progenitor cells. Neuronal cells were incubated with LAMP1 (green) and p62 (red) primary antibody at a dilution of 1:200 for a minimum of ~12 hours at 4^{O}C, followed by the incubation of Alexa Fluor 488 rabbit (emission 519nm) and Alexa Fluor 568 mouse (emission 601nm) secondary antibodies, respectively. Following this, cells were also incubated with DNA stain, DAPI (emission 453nm) in order to visualize nucleus. Arrows show the accumulation of LAMP1 (green) in the axons of the neurons, whilst arrows directed towards p62 (red) display accumulation within vesicles, an indicator of impaired autophagy. Images shown at x20 magnification, whilst scale bar displayed at 100μm.

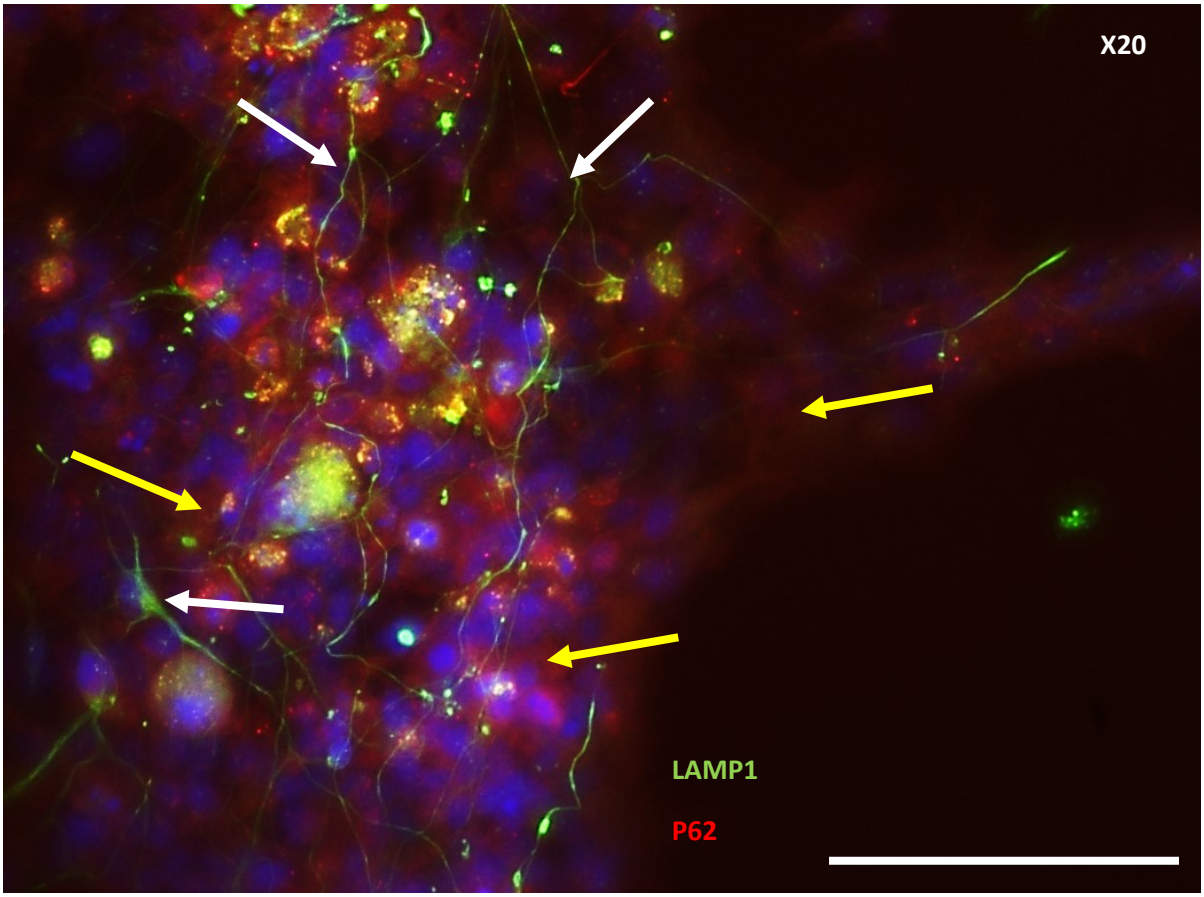

Figure 24: p62 & Lamp1 ICC Staining of Neuronal Cells

Figure 24. Immunocytochemistry image produced depicts CLN7 neurons developed through terminal differentiation of neural progenitor cells. Neuronal cells were incubated with LAMP1 (green) and p62 (red) primary antibody at a dilution of 1:200 for a minimum of ~12 hours at 4^{O}C, followed by the incubation of Alexa Fluor 488 rabbit (emission 519nm) and Alexa Fluor 568 mouse (emission 601nm) secondary antibodies. Following this, cells were also incubated with DNA stain, DAPI (emission 453nm) in order to visualize nucleus. White arrows show the accumulation of LAMP1 (green) in the axons of the neurons, whilst yellow arrows directed towards p62 (red) display accumulation within vesicles, an indicator of impaired autophagy. Images shown at x20 magnification, whilst scale bar displayed at 100μm.

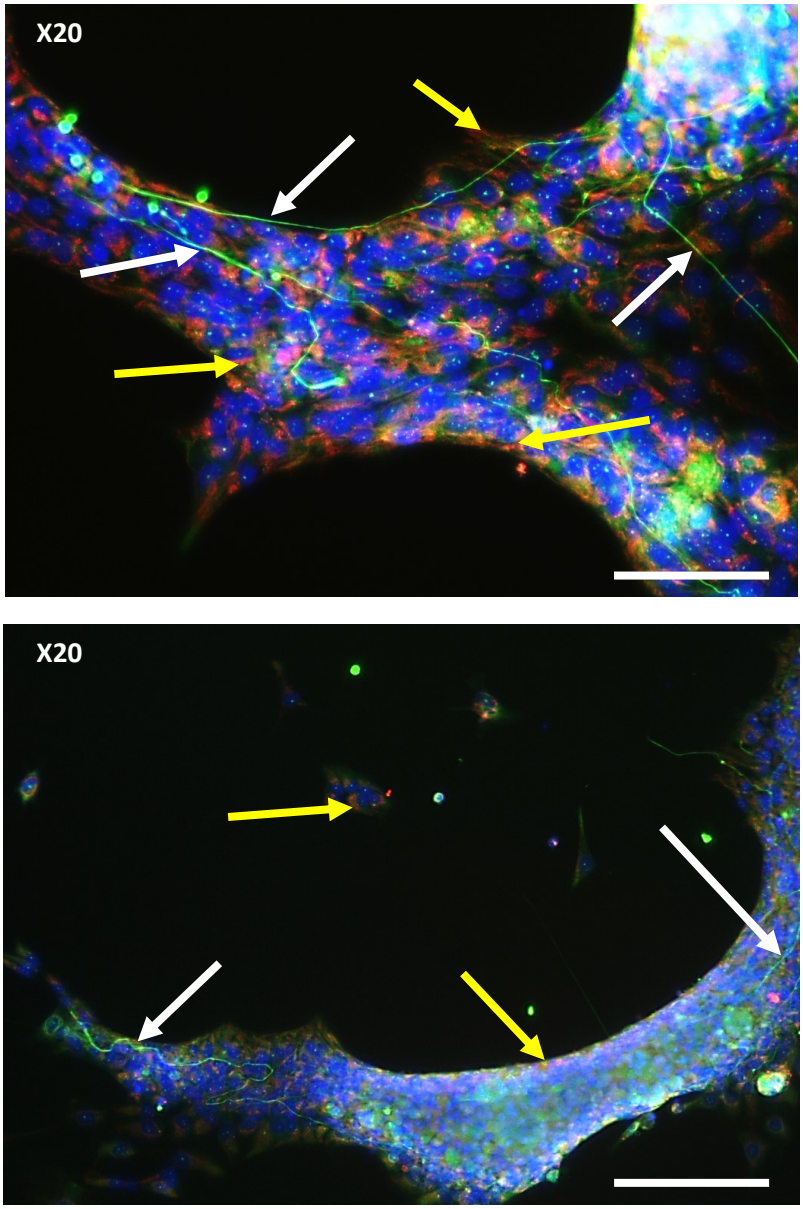

Figure 25: MitoTracker & Lamp1 ICC Staining of Neuronal Cells

Figure 25. Immunocytochemistry image produced depicts CLN7 neurons developed through terminal differentiation of neural progenitor cells. Neuronal cells were incubated with LAMP1 (green) and at a dilution of 1:200 for a minimum of ~12 hours at $4^{O}C$, followed by the incubation of Alexa Fluor 488 rabbit secondary antibody (emission 519nm) in addition to incubation of MitoTracker (red) (emission 644nm), in order to assess mitochondria utilizing mitochondrial membrane potential. Following this, cells were also incubated with DNA stain, DAPI (emission 453nm) in order to visualize nucleus. White arrows show the accumulation of LAMP1 (green) in the axons of the neurons, whilst yellow arrows directed towards MitoTracker (red) within mitochondria. Images shown at x20 magnification, whilst scale bar displayed at 100μm.

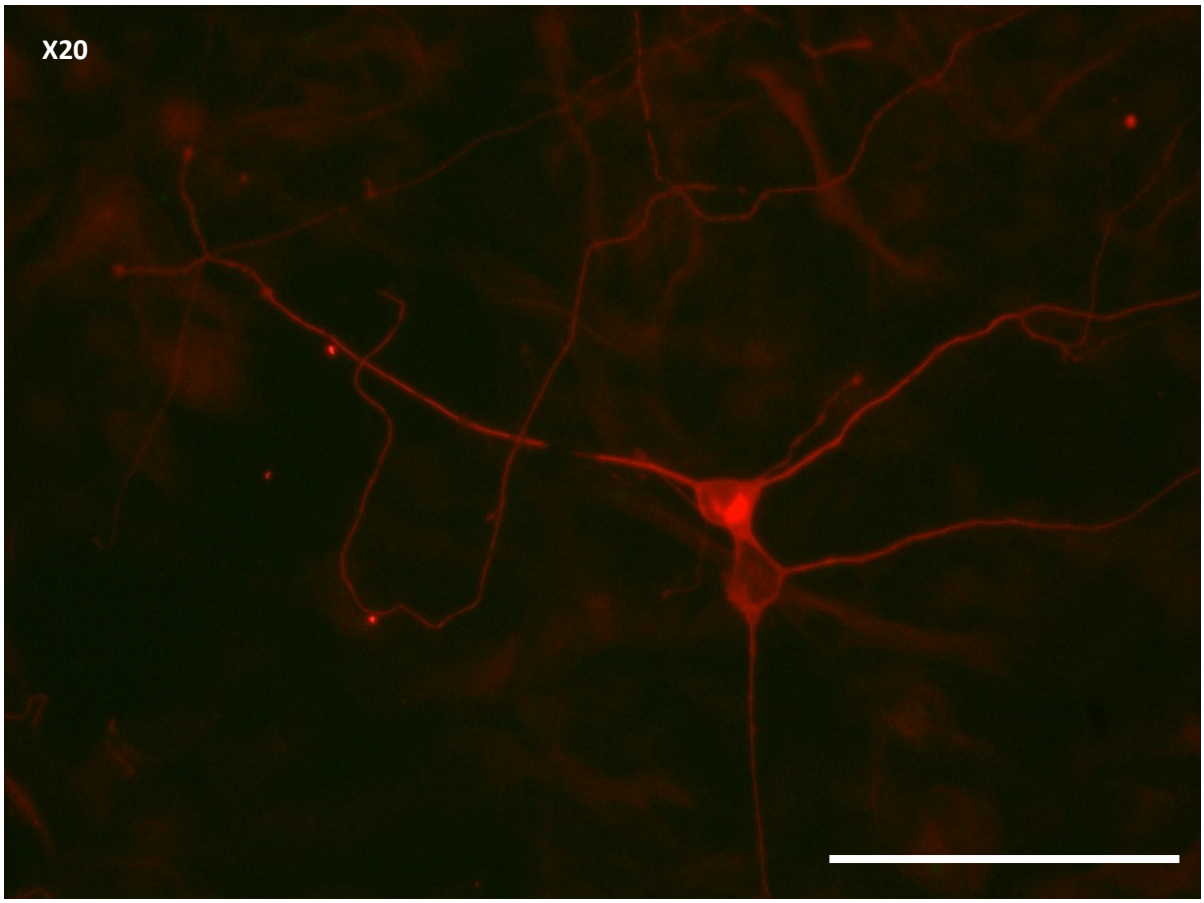

Figure 26: B-III-tubulin ICC Staining of Neuronal Cells

Figure 26. Immunocytochemistry image produced depicts CLN7 neurons developed through terminal differentiation of neural progenitor cells. Neuronal cells were incubated with neural marker, β-III-tubulin at a dilution of 1:200 for a minimum of ~12 hours at $4^{O}C$, followed by the incubation of Alexa Fluor 568 mouse secondary antibody (emission 601nm) at a dilution of 1:500. Images shown at x20 magnification, whilst scale bar displayed at 100μm.

5.0 Discussion

The aim of this project was to utilize current techniques and technologies in neural differentiation to successfully produce neural progenitor cells and neurons via differentiation of patient CLN7 induced pluripotent stem cells and controls. The purpose of developing these cells was to deduce phenotypic changes between CLN7 and controls and thus infer any differences in autophagic function. Our feeder free CLN7 and control iPSCs, provided by the McKay lab, were subjected to a stepwise neural differentiation protocol, which encouraged the differentiation and proliferation of neuroectoderm through minimizing the exposure to exogenous growth factors. Once neural progenitor cells were cultured during differentiation, both RNA and protein were extracted in order to undergo molecular analysis through techniques such as; western blot analysis, RT-PCR and qPCR in order to deduce the accumulation of specific proteins and expression of various genes.

5.1 Successful Derivation of iPSCs Through Somatic Reprogramming

The results indicate the successful development of neural progenitor cells in both CLN7 and control cells as well as successful differentiation to neurons of the patient CLN7 cells. Western blot, qPCR and RT-PCR analysis show clear differences in gene expression and protein accumulation between the two cell lineages. As previously stated, there is limited information regarding CLN7 disease and the mechanisms involved in disease progression through maturation of neural cells. The data produced indicates significant differences in accumulation of autophagy related proteins and the expression of various genes related to metabolism, oxidative stress and inflammation in CLN7 NPCs, whilst CLN7 iPSCs displayed expression of the various genes comparable to healthy controls.

Prior to the implementation of neural differentiation, the induced pluripotent stem cells of both and CLN7 and control cell lines were validated for pluripotency markers via immunocytochemistry and RT-PCR. The presence of pluripotency markers Sox2, Tra-1-81 and Oct4 was

confirmed in both feeder iPSCs (iPSCs on MEFs) and feeder free iPSCs. RT-PCR was able to qualitatively assess the gene expression of pluripotency markers Oct4, Nanog and Lin28A as well as E-cadherin, a key regulator of pluripotency and self-renewal in iPSCs and embryonic stem cells. Through this assessment, it could be deduced that the CLN7 and control iPSCs displayed gene expression of these markers, which was akin to those of embryonic stem cells. The data collected from both immunocytochemistry and RT-PCR demonstrated validated iPSC lines with apparent pluripotency characteristics.

5.2 Successful Derivation of NPCs Confirmed by qPCR

The project aimed to deduce any differences in phenotype of neural progenitor cells of CLN7 compared to healthy counterparts. Successful derivation of NPCs was confirmed by qPCR analysis of pluripotency markers, LIN28A and SOX2 in NPCs compared to that of iPSCs. Data collected displayed a loss in the pluripotency markers through neural differentiation with LIN28A showing an increase in relative expression in CLN7 iPSCs and control iPSCs compared to their NPC counterparts, with a 73-fold and 50-fold increase respectively, with a statistical significance of $p=0.002$ and 0.02 respectively. There was also an increase in relative expression of SOX2 in iPSCs compared to their NPC counterparts. CLN7 iPSCs had 8-fold increase in expression levels with a strong statistical significance of $p=0.003$ whereas control iPSCs displayed a 124-fold increase in gene expression of SOX2, also displaying a strong statistical significance of $p=0.0005$.

The neural progenitor cell marker, Nestin was also utilized in order to evaluate differentiation efficacy. A 3.7-fold increase in relative gene expression of CLN7 NPCs compared to CLN7 iPSCs was observed with a statistical significance of 0.04. Indeed, control NPCs also displayed comparative levels of increase in relative gene expression with a 15.5-fold increase observed with a statistical significance of 0.01. The loss of pluripotency markers LIN28A and SOX2, coupled with the increase in NPC marker, Nestin, confirms the successful differentiation of iPSCs to NPCs in both CLN7 cells and healthy controls.

5.3 Upregulation in the Inflammatory Response in CLN7 NPCs and Neuronal Cells

It was apparent there was an increase in gene expression of NFkB1 in CLN7 neural progenitor cells, with a 1.54 times upregulated expression in CLN7 NPCs compared to that of control NPCs with a strong significance of p=0.008. The nuclear factor, NFkB pathway has been extensively researched in relation to the inflammatory response. This pathway has long been considered a prototypical proinflammatory signaling pathway, this has been evident during the activation of this pathway by the tumor necrosis factor α (TNFα) and proinflammatory cytokines, e.g. interleukin 1 (IL-1) (Lawrence, 2009). The inflammatory response is characterized by the coordinated activation of various signaling pathways, such as that of NFkB which has been shown to exist through the activation of both canonical and alternative pathways (Liu *et al.*, 2017).

In addition, extensive research has shown that the scaffold protein and autophagy receptor, p62, activates the NFkB pathway (Katsuragi, Ichimura and Komatsu, 2015). p62/SQSTM1 (hereafter p62) is an evolutionary conserved, stress-inducible, cellular protein among multicellular organisms. P62 has been reported to act as a receptor for autophagic cargo via interactions with ubiquitinated proteins and LC3 (Liu *et al.*, 2016). P62 distribution is found within the cytoplasm, but also localizes in the nucleus, autophagosomes and lysosomes (Chen *et al.*, 2014). Research has demonstrated that p62 is degraded during autophagy, in NCL patients, a significant accumulation of p62 has been observed due to an impairment of this physiological process, preceded by the formation of p62 and ubiquitin positive aggregate structures (Mohammed *et al.*, 2017). The adaptor protein, p62, plays a critical role in selective autophagy and demonstrates multiple domains (see figure 3), including the ubiquitinated-associated domain (UBA), which results in the formation of dimers that are destabilised by ubiquitin binding (Katsuragi, Ichimura and Komatsu, 2015). As well as its role in autophagy, p62 acts as a scaffold protein in NFkB activation. The inflammatory pathway is activated via the binding of p62 with atypical PRKC, RIPK1 (receptor (TNFRSF)- interacting serine-threonine

kinase 1) or tumour necrosis-associated factor 6 (TRAF6) through the PB1, zinc finger (ZZ) or TRAF6 (TB) domains respectively (see figure 19) (Katsuragi, Ichimura and Komatsu, 2015).

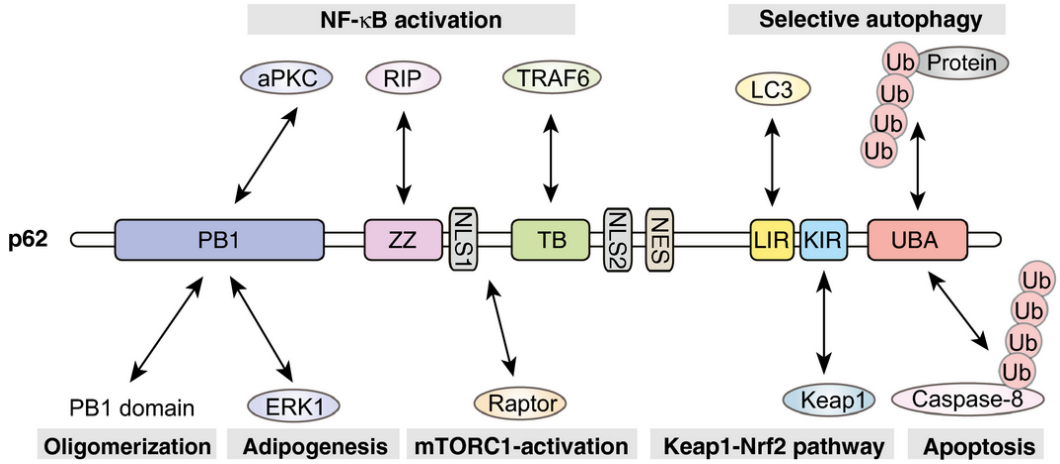

Figure 27: p62 domains

Figure 26. A representation of the domain structures of p62 and its binding partners. P62 and Keap1 are able to interact via the KIR and LC3 is able to recognise p62 via the LIR. Atypical PKC (aPKC) and ERK1 interact with p62 via the PB1 domain, which is able to self-oligomerize and form hetero-oligomers with other proteins, which contain a PB1 domain. The ZZ domain associates with RIP and TRAF6-binding domain (TB) interacts with TRAF6. TRAF6, RIP and aPKC are thought to be involved in NF-kB activation, mediated by p62. The interaction between ERK and p62 is thought to negatively regulate adipogenesis (Katsuragi et al.,

5.4 Autophagic Flux is Reduced in CLN7 Neural progenitor and Neuronal Cells

In addition to qPCR analysis of NFkB1 expression, western blot analysis was implemented in order to give a semi-quantitative assessment of p62 accumulation in CLN7 NPCs compared to that of the control NPCs. There was an apparent increase in p62 accumulation in progenitor cells of CLN7 when compared to that of control, healthy NPCs when analyzed through western blot analysis, with a 7.8-fold increase observed in CLN7 NPCs. Immunocytochemistry also displayed a clear accumulation of p62 within the peripherals of the CLN7 derived neurons. P62 and its accumulation within neural cells has been shown to be indicative of impaired autophagy, an inducible development within CLN7 and neuronal ceroid Lipofuscinoses patients (Steenhuis *et al.*, 2010). Autophagy is an evolutionary conserved catabolic pathway, vital for its necessity in physiological processes, at the forefront is in which long-lived proteins and damaged organelles are

delivered to lysosomes for degradation in order to maintain energy homeostasis (Johansen and Lamark, 2011). Autophagy arises when the sequestered proteins and organelles forming an autophagosome fuse with a lysosome in order to degrade the cargo (Ganley *et al.*, 2011).

The impairment of autophagy in the CLN7 affected NPCs is supported further through the accumulation of p70 and phosphorylated p70 (p-p70) with a fold increase in CLN7 NPCs of 3.8 and 1.4 respectively. The protein, p70 S6 kinase is a downstream target of the mammalian target of rapamycin (mTOR) that is phosphorylated upon activation of the mTORC1 pathway (Magnuson, Ekim and Fingar, 2012) (Xiao *et al.*, 2009). The atypical serine/threonine kinase, mTOR, is a member of the phosphoinositide 3-kinase related kinase family (PI3K) (Laplante and Sabatini, 2012). Interactions between mTOR and various proteins results in the formation of two distinct complexes; mTOR complex 1 (mTORC1) and mTOR complex 2 (mTORC2), these distinct complexes demonstrate differing upstream inputs, downstream outputs and sensitivities to rapamycin (Figure 4) (Katsuragi, Ichimura and Komatsu, 2015). Both of these complexes are similar in size, with mTORC1 having six known protein components whereas mTORC2 contains seven (Laplante and Sabatini, 2012). The mTORC1 complex is activated via amino acids on the surface of lysosomes, where the assembly of Rag proteins, Rheb, Ragulator, v-ATPase and putative amino acid sensors occurs (Figure 5). The subunit of mTORC1, Raptor, was identified as a p62-interacting protein with both Raptor and RagC/D shown to be able to interact with p62. This interaction is shown to be amino acid-dependent, with an increase in amino acid levels leading to the translocation onto lysosomes (Katsuragi, Ichimura and Komatsu, 2015). A recent study showed that amino acid stimulation lead to the ubiquitination of mTOR through K63-linkage via TRAF6. This interaction has been shown to be p62 dependent, resulting in the mTORC1 activation on the lysosome being regulated via the K63-ubiquitinated mTOR. However, the mechanisms in which the enhancement of TRAF6 activity via amino acids occur is poorly understood. These interactions for mTORC1 activation suggest that p62 is a pivotal adaptor in this mechanism (Katsuragi, Ichimura and Komatsu, 2015).

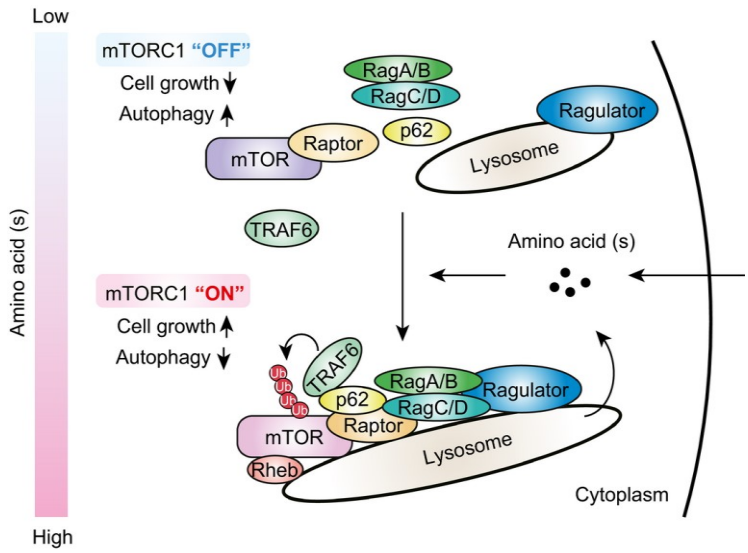

Figure 28: p62 and mTORC1

Figure 27. Depiction of the signalling functions of p62 in the activation of mTORC1 pathway, with Raptor, RagC and TRAF6 components on the lysosomal membrane. K63-ubiquitination of mTOR via TRAF6 promotes the activation of mTORC1. This activation results in the phosphorylation of S6K and ULK1/2, which in turn induces protein synthesis and supresses autophagy. The interactions occur in an amino acid-dependent manner; however, the amino acid level does not influence localisation of p62 on lysosomes (Katsuragi et al., 2015)

Impairment of autophagy can be further inferred through the accumulation of lysosomal associated membrane protein 1 (LAMP1) within the CLN7 derived neurons depicted through immunocytochemistry. Lysosomes are responsible for the degradation of deleterious waste products and fuse with autophagosomes during autophagy in order to from autolysosomes for vesicle breakdown and degradation (Brandenstein *et al.*, 2016). LAMP1 is a major protein component of the lysosomal membrane, being a type I transmembrane protein with a C-terminal cytoplasmic tail, luminal and transmembrane domain (Eskelinen, 2006). LAMP1 is considered an autophagic marker with accumulation of the protein attributed to autophagy impairment (Huynh *et al.*, 2007). The immunocytochemistry data collected shows clearly, the distribution of the protein and its accumulation within the axons of CLN7 affected neurons.

Although the results obtained through western blot analysis and immunocytochemistry indicate the validation of impaired autophagy within the CLN7 neural progenitor cells and further differentiated neurons, our techniques possess certain limitations. Further

western blot analysis for the accumulation of LAMP1 and LC3-II would have provided further evidence and corroborated the immunocytochemistry data. Also, as previously stated, due to unforeseen circumstances immunocytochemistry data shown only depicts immunostaining of CLN7 neurons due to issues with terminal differentiation of control NPCs.

5.5 CLN7 NPCs Show a Metabolic Shift Towards Glycolysis

Neurons have been shown to rely heavily on oxidative phosphorylation (OXPHOS) in order to meet energy demands, with studies showing the shift in glycolysis to OXPHOS in NPCs is tightly coupled to differentiation of neurons (Ito and Suda, 2014). Dysfunction within mitochondria leading to impaired oxidative phosphorylation has been shown to be frequent within neurological conditions and leads to neurodegeneration due to insufficient ATP production (Chen *et al.*, 2008) (Hüttemann *et al.*, 2007). The loss of lactate dehydrogenase (LDHA) coupled with a switch in pyruvate kinase gene splicing from PKM2 to PKM1 is shown to denote the transition from glycolysis in neural progenitor cells to OXPHOS in neuronal cells (Steenhuis *et al.*, 2010). Although studies have shown that NPCs are less reliant on OXPHOS than neurons, it has been shown that the progenitor cells display a reduction in glycolytic consumption in order to differentiate towards neurons (Ivanov *et al.*, 2014). CLN7 derived and control neural progenitor cells were analysed using a variety of metabolic and glycolytic markers in order to ascertain key differences in cellular metabolism. Our results indicate a shift towards glycolysis opposed to oxidative phosphorylation in CLN7 NPCs as well as an upregulation in the gene expression of CLN7 iPSCs compared to control iPSCs.

The glycolytic limiting enzyme, pyruvate kinase muscle catalyses glycolysis by the irreversible transphosphorylation between adenosine diphosphate and phosphoenolpyruvate (PEP) resulting in the production of pyruvate and ATP. This reaction leads to the induction of glycolysis (PKM2) or oxidative phosphorylation via alternative splicing of the PKM gene's primary RNA transcript (PKM1) (Ito and Suda, 2014). PKM1 and PKM2 possess differences in activity and tissue expression with PKM1 being constitutively active in tissues of the muscle and brain, including neurons. Conversely, PKM2 is expressed in anabolic functioning tissues such as proliferating and cancerous cells (Gu *et al.*, 2016).

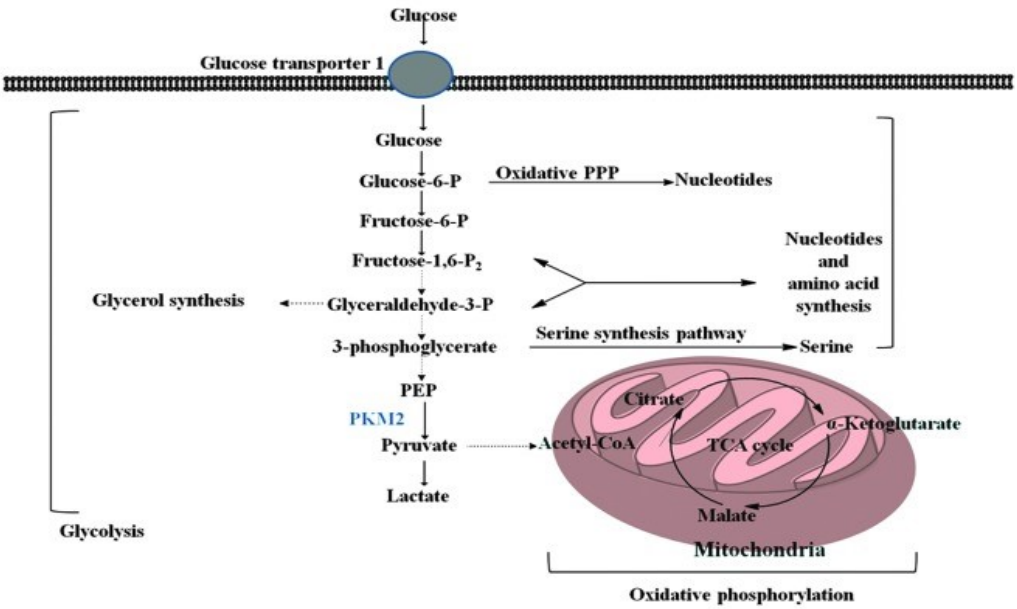

Figure 29: Regulation of PKM2

Figure 28. The regulation of the metabolic pathway via PKM2. This pyruvate kinase isoform is less active and thus this decreased enzymatic activity in the cytoplasm promotes the accumulatio of upstream glycolytic targets and subsequently converts them into the anabolic pathway (Ito and Suda, 2014).

It has been demonstrated in cancer cells that mTOR induces the Warburg effect, a cells apparent preference of glycolysis over oxidative phosphorylation through the induction of PKM2 as well as other glycolytic enzymes (Ito and Suda, 2014). There was an increase in expression of PKM2 in CLN7 NPCs of 2.1 compared to control counterparts with a significance of 0.02 indicating CLN7 patient derived neural progenitor cells favour glycolysis. This notion was further supported by an increase in expression of glucose transporter 1 (GLUT1) with 16.2-fold increase in its relative expression compared to that of controls with a significance of p=0.04.

Oxidative phosphorylation consists of five multimeric complexes responsible for the formation of the mitochondrial respiratory chain (Koopman *et al.*, 2013). This results in the transfer of electrons from reducing equivalents to water, thus forming the proton gradient across the inner mitochondrial membrane, utilised by the F_1F_0 ATPase in order to drive ATP synthesis (Pattappa *et al.*, 2013). Although this system is more efficient in the production of ATP within neural cells, OXPHOS generates reactive oxygen species (ROS) within the electron transport chain, thus leading to an increase in oxidative stress (Ivanov

et al., 2014) (Schieber and Chandel, 2014). Our study found that there was an upregulation of the oxidative stress marker, HO-1 in control NPCs compared to CLN7 NPCs. Indeed, HO-1 was 5.9 times more highly expressed in control NPCs with a significance of p=0.04. This result further supports the notion that CLN7 NPCs undergo a metabolic shift towards glycolysis whilst controls move towards OXPHOS for successful differentiation to neurons.

Although our results are indicative of a metabolic shift towards to glycolysis, it is limited through utilising qPCR as its primary source of data collection. To further support the notion of a metabolic shift towards glycolysis, future efforts should utilise existing technologies in the Agilent SeahorseXF Analyzer. Capable of measuring glucose uptake and lactate excretion into the surrounding media, the analyser is capable is of measuring glycolytic flux in cells in culture. The XF instrument measures the acidification rate directly, and reports this as the extracellular acidification rate (ECAR). Firstly, cells are incubated in glycolysis stress test medium without glucose or pyruvate, ECAR us then measured (Agilent Technologies, 2017). The first injection saturates the medium with glucose. The cell catabolise glucose via the glycolytic pathway to pyruvate, producing ATP, NADH, H_2O and H^+. Extrusion of protons into surrounding media causes accelerated increase in ECAR (reported as the rate of glycolysis under basal conditions). (Agilent Technologies, 2017) Oligomycin is then injected (ATP synthase inhibitor) and shifts energy production to glycolysis, subsequent increase in ECAR revealing the cellular maximum glycolytic capacity. Finally, 2-deoxy-glucose (2DG) is injected (a glucose analog), inhibiting glycolysis via competitive-binding to glucose hexokinase (first enzyme in the glycolytic pathway) (Agilent Technologies, 2017).Resultant decrease in ECAR confirms that ECAR produced in the experiment is due to glycolysis, difference between glycolytic capacity and glycolysis rate defines glycolytic reserve. The corroboration from possible glycolytic flux data, would potentially generate greater support for our hypothesis and support further our current data.

5.6 Upregulation of SIRT1 to Combat Oxidative Stress

The NAD+ dependent deacetylase, Sirt1, has been shown to play various roles in cellular processes such as; metabolism, cell survival and adaption to cellular stress as well as autophagy induction (Salminen, Kaarniranta and Kauppinen, 2013). SIRT1 has been extensively studied in vitro in endothelial cell dysfunction and its effect on oxidative

stress, with the complex able to produce an antioxidant response by modulating the expression of oxidative stress protection genes, however the mechanisms in which SIRT1 facilitates this response is largely unknown (Salminen, Kaarniranta and Kauppinen, 2013) (Chang and Guarente, 2014). Subsequently studies into understanding its antioxidant effect have been explored with research demonstrating that the transcription factors FoxO3a and PGC-1α induce this response (Chan *et al.*, 2017). Studies regarding autophagy have demonstrated that increased ROS production and subsequent increase in oxidative stress induce autophagy (Ou *et al.*, 2014) (Liemburg-Apers *et al.*, 2015). ROS are highly reactive molecules that are produced as a byproduct via cellular metabolism. An increase in ROS production due to dysregulation or disease leads to oxidative stress when ROS formation exceeds antioxidant response (Schieber and Chandel, 2014). Oxidative stress has been shown to result in the accumulation of autophagosomes through signal transduction regulation via ROS signaling (Liemburg-Apers *et al.*, 2015). As previously stated, HO-1 expression is significantly decreased in CLN7 NPCs, indicating a decrease in ROS production with a 7.8-fold increase in SIRT1 expression in CLN7 NPCs also shown. This indicates that SIRT1 overexpression in the CLN7 NPCs is resulting in an antioxidant response, this reduction in oxidative stress, confirmed by downregulation in HO-1 may be resulting in a reduction in autophagosome accumulation and trafficking leading to an impairment of autophagy.

As previously mentioned, CLN7 is thought to share sequence homologies with the major superfamily of active transporters (Kousi *et al.*, 2009). Neuronal ceroid lipofuscinosis disorders are characterized by the accumulation of lysosomal storage material- lipofuscin, composed of subunit c of mitochondrial ATP synthase (Cárcel-Trullols, Kovács and Pearce, 2015). CLN7 neural progenitor cells were shown to have a 10.6-fold increase in ATP synthase expression with a statistical significance of 0.03. ATP synthase catalyzes the terminal step of oxidative phosphorylation and synthesizes ATP from adenosine diphosphate (ADP) and $P_{i.}$ Proton translocation (Junge and Nelson, 2015). This increase in CLN7 NPCs would suggest that there is an increase in OXPHOS; however, our data contradicts this notion. Therefore, it could be inferred that this increase in ATP synthase could be due to mitochondrial dysfunction, resulting in the signal to transduce and overexpress ATP synthase in these CLN7 NPCs (Inoue *et al.*, 2010). As these NPCs favor glycolysis, ATP synthase accumulates and is unable to be degraded due to impaired autophagy as shown in previous results. This would lead to an accumulation in storage

material within neural progenitors and resulting neurons, with lipofuscin shown to be composed of subunit c of mitochondrial ATP synthase, which implies this could be the mechanism behind the accumulation of this material.

Our results are indicative of an antioxidant response in CLN7 NPCs, shown to be confirmed by a decrease in the expression of HO-1, compared to control NPCs. However, as with our aforementioned data displaying a metabolic shift towards glycolysis, our data is limited by qPCR being the primary source of data. In order to confirm our results, further oxidative stress experiments should be performed in order to confirm our results. The SeahorseXF Analyzer Mitostress kit by Agilent, is capable of measuring mitochondrial function, by directly measuring oxygen consumption rate (OCR) with the assay providing insight into mitochondrial dysfunction and functional differences between cell types. The assay performs functional analysis through the use of built in injection ports in order to add modulators of respiration (Oligomycin, Carbonyl cyanide-4 (trifluoromethoxy) phenylhydrazone (FCCP), Rotenone and Antimycin) into the cell wall during the assay to reveal parameters of mitochondrial function (Agilent Technologies, 2019). Oligomycin is first injected, inhibiting ATP synthase, impacting/decreasing the electron flow through the electron transport chain (ETC), thus reducing mitochondrial respiration or OCR, linked to ATP production (Agilent Technologies, 2019). FCCP is then injected, collapsing the proton gradient, disrupting the mitochondrial membrane potential. Thus, electron flow through ETC is uninhibited and oxygen consumption reaches maximum. FCCP-stimulate OCR can then be used to calculate spare respiratory (ability of cell to respond increased energy demand or under stress) capacity (defined as; difference between maximal respiration and basal respiration) (Agilent Technologies, 2019). Lastly, rotenone and antimycin A (a complex III inhibitor) are injected, shutting down mitochondrial respiration and allowing nonmitochondrial respiration driven by processes outside the mitochondria to be calculated (Agilent Technologies, 2019).

5.7 Impaired Autophagy Lead to an Upregulation of the NFκB Pathway, Resulting In a Decrease In ROS Production

The results obtained indicate the activation of both the mTORC1 and NFkB pathway in CLN7 patients via sequestered p62 accumulation. The protein p62 has been proven to be an NFkB agonist through its binding with atypical PRKC, RIPK1 (receptor (TNFRSF)- interacting serine-threonine kinase 1) or tumour necrosis-associated factor 6 (TRAF6) through the PB1,

zinc finger (ZZ) or TRAF6 (TB) domains respectively (Katsuragi, Ichimura and Komatsu, 2015). The accumulated p62 is also able to interact and upregulate the mTOR pathway, with both Raptor and RagC/D shown to be able to interact with p62 (Duran *et al.*, 2011). This interaction leads to the phosphorylation of the downstream target, p70 S6 kinase resulting in a downregulation of autophagy (Xiao *et al.*, 2009). The results produced indicate the importance of p62 and its intrinsic link in both autophagy impairment and increase in inflammation. Upregulation in inflammation within neural cells has proven to be a key component of neurodegeneration in biomedical research, thus this upregulation could be a key component of the degeneration in CLN7 patients including motor and cognitive regression due to neuronal cell death via the inflammatory response (Aktas *et al.*, 2007).

Our results are indicative of an increase in the antioxidant response in CLN7 NPCs with significant decrease in ROS production. ROS production is known to either stimulate or repress NFkB activity depending on phase and context (Lingappan, 2018). Nuclear factor-kappa B (NFkB) modulates the gene expression of a variety of cellular processes, such as; the innate immune response, cell proliferation, apoptosis and stress responses to a variety of toxic stimuli (Hayden and Ghosh, 2004). Under conditions, in which cellular production of ROS overwhelms the antioxidant response, a state of oxidative stress is induced (Kim *et al.*, 2015). The NFkB pathway is known to possess anti-oxidant roles in conditions of oxidative stress. Evidence suggests NFkB plays a protective role, under oxidative stress conditions via inhibiting ROS accumulation (Djavaheri-Mergny *et al.*, 2004). Results have previously shown that inhibiting NFkB results in an increase in TNFα-induced ROS production, lipid peroxidation and protein oxidation (Djavaheri-Mergny *et al.*, 2004). ROS signalling can trigger apoptosis depending on the severity of the oxidative stress, NFkB targets genes promoting cell survival via attenuation of ROS (Vallabhapurapu and Karin, 2009). One of the ways by which NFkB affect ROS levels, is by increased levels of antioxidant genes, such as Manganese Superoxide Dismutase (MnSOD) (Kairisalo *et al.*, 2007). The mitochondrial enzyme, MnSOD

protects cells from oxidative stress via conversion of O_2^- into H_2O_2 (Morgan and Liu, 2011). Previous studies into human endothelial cells have shown SIRT1 promotes the regulation of MnSOD expression, whilst increasing oxidative stress resistance (Zhang *et al.*, 2017).

ROS signalling has also been shown to play a complex intrinsic role in glycolytic activity (Kondoh *et al.*, 2007). Increased mitochondrial ROS production is observed in various pathological conditions, a hallmark of the groups of diseases is enhanced glycolytic activity with low oxidative phosphorylation (Liemburg-Apers *et al.*, 2015). A study found that in conditions of increased ROS production, mitochondria converted to the glycolytic pathway in order to reduce mitochondrial ROS levels (Liemburg-Apers *et al.*, 2015). Although conditions may favour glucose-stimulated ROS production, elevated levels of ROS may also be counterbalanced by endogenous antioxidant systems in conjunction with shift towards glycolysis (Liemburg-Apers *et al.*, 2015).

As previously stated, our results suggest a metabolic shift towards glycolysis of CLN7 NPCs as shown in 5.5. This change in the metabolic profile of the CLN7 NPCs resulted in an increase in ROS production, thus increase in oxidative stress. However, our results show CLN7 NPCs have significant decrease in HO-1 expression compared to healthy controls, with an increase in SIRT1 expression of 7.8-fold. Previous studies have found that in addition to a shift to glycolysis, a cell's endogenous antioxidant response system may counterbalance the increase in ROS. This notion is supported by the increase in SIRT1 in CLN7 NPCs by 7.8-fold when compared to control NPCs. In conjunction, CLN7 NPCs display a 1.54-fold increase in NFkB expression than that of controls, with NFkB known to produce antioxidant effects by acting upon MnSOD and inhibiting ROS production.

6.0 Future Work

The results from the project allow for the deduction of differences in metabolism and autophagic flux in CLN7 neural progenitor cells compared to controls. The results show promising progression into understanding the mechanisms and pathogenesis of CLN7 disease, however the data provides a strong foundation for further research. Although the production of CLN7 neurons was successful during the project there were issues regarding cell death in terminal differentiation. Currently, most neural differentiation protocols are time consuming and inefficient, future research should aim to drastically improve the efficiency of the protocols.

Our results demonstrated a metabolic shift towards glycolysis in neural progenitor cells of CLN7 compared to controls; however, it was not clear the mechanisms in which this occurred. This clearly shows the need for additional research into the relationship between OXPHOS and glycolysis in CLN7 NPCs and subsequent neuronal cells. A suggested method for measuring the rate of glycolysis within our CLN7 NPCs compared against controls would be to measure the glucose uptake and lactate production of each cell type using our in-house Agilent, SeahorseXF Analyzer. Glycolytic flux of a cell in culture can be measured via the measurement of glucose uptake and the excretion of lactate into the surrounding media. This further analysis would be of great use in providing further insight into the metabolic shift of CLN7 NPCs.

As well as measuring glycolytic flux, the SeahorseXF Analyzer is capable of measuring oxidative stress in cell in culture. The Seahorse XF Cell Mito Stress Kit is optimized for assessing mitochondrial function, with multiple parameters obtained in one assay such as; basal respiration, ATP production-coupled respiration, maximal and reserve capacities and non-mitochondrial respiration. The analysis provides insights into mitochondrial dysfunction and permits investigation into functional differences between cell types. Our results suggest an increase in SIRT1 as a response to oxidative stress, Seahorse oxidative stress analysis would be of great use to support our results.

We were able to deduce differences in autophagic flux through the utilization of western blot, further analysis into accumulation into proteins such as microtubule-associated protein light chain-II (LC3-II) and LAMP1 would be of great use in providing further evidence of autophagic impairment.

7.0 Appendix

7.1 Terminal differentiation of CLN7 NPCs

Figure 30: Terminal differentiation images of CLN7 NPCs.

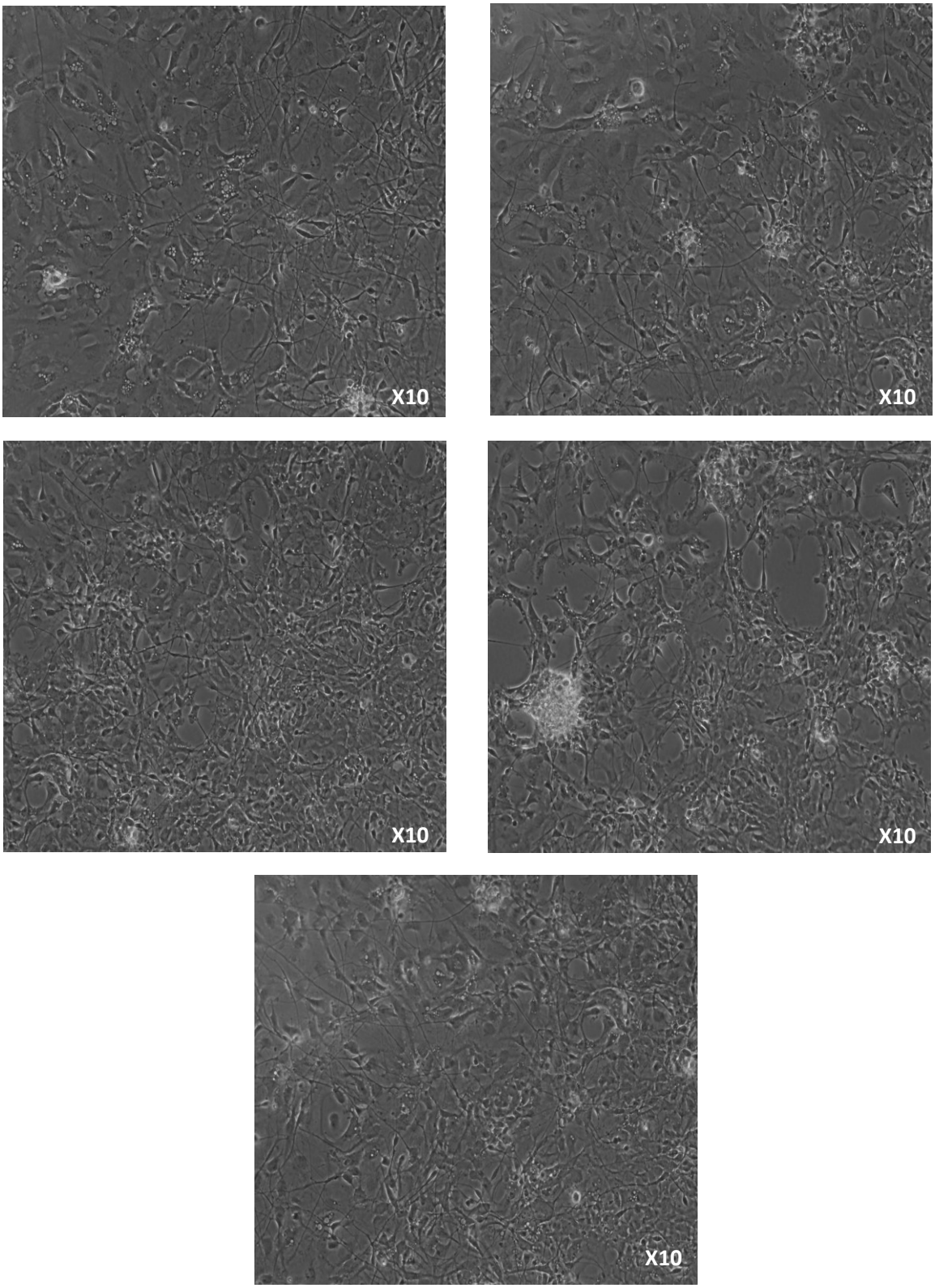

7.2 RT-PCR Analysis of NPCs

Prior to qPCR analysis, RT-PCR was implemented initially in order to qualitatively assess differences in expression of various genes in CLN7 NPCs compared to controls. Once data had been collected, quantitative PCR was implemented for a more accurate measurement of gene expression. Images below depict results obtained.

Table 20: RT-PCR Primers

Target	**Forward Primer**	**Reverse Primer**
Endogenous OCT4	GCGATCAAGCAGCGACT	TTCACCTTCCCTCCAACC
Endogenous SOX2	CATGTCCCAGCACTACCAGA	GGGTTTTCTCCATGCTGTTT
Endogenous LIN28	TGTCCAAATGCAAGTGAG	GCAGGTTGTAGGGTGATTCC
Nanog	TTTGTGGGCCTGAAGAAAACT	AGGGCTGTCCTGAATAAGCAG
E-cadherin	TGCCCAGAAAATGAAAAAG	GTGTATGTGGCAATGCGTTC
GAPDH	ATGTTCGTCATGGGTGTGAA	GGTGCTAAGCAGTTGGTGGT
GLUT1	AACTCTTCAGCCAGGGTCCAC	CACAGTGAAGATGATGAAGAC
SIRT1	TAGCCTTGTCAGATAAGGAAGGA	ACAGCTTCACAGTCAACTTTGT
Nestin	GGCAGCGTTGGAACAGAG	CATCTTGAGGTGCGCCAGCT
RN18S1	ACACGGACAGGATTGACAGA	GGACATCTAAGGGCATCACAG

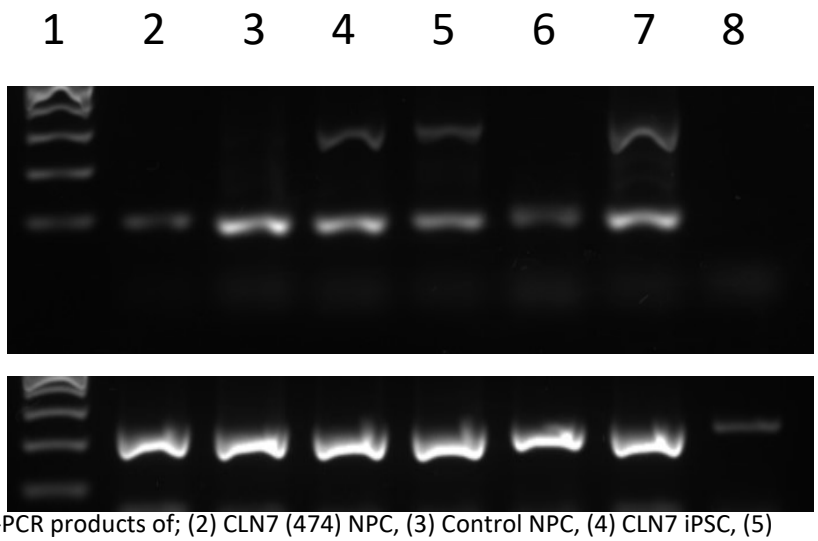

Figure depicts RT-PCR products of; (2) CLN7 (474) NPC, (3) Control NPC, (4) CLN7 iPSC, (5) Control iPSC, (6) HEK293, (7) Shef3 ESC and (8) No-RT ran along a 2% agarose gel supplemented with GelRed at 15V for 1 hour for qualitative analysis of GAPDH marker. Secondary image displays PCR product of RN18S1 housekeeper.

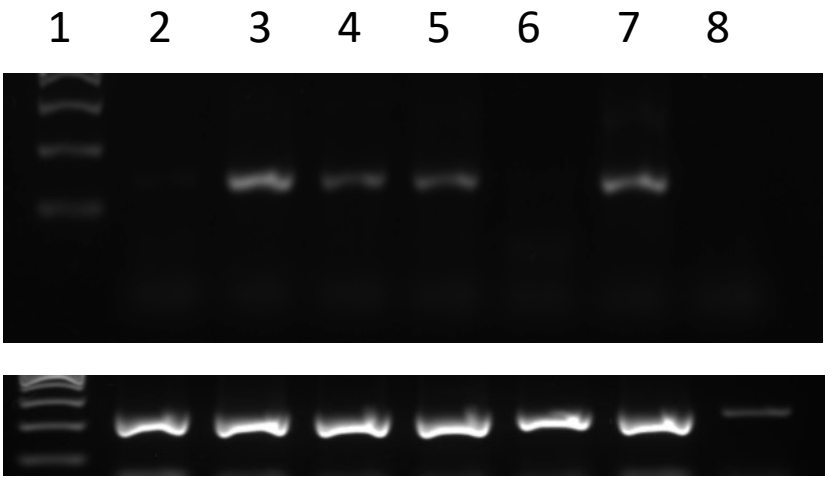

Figure depicts RT-PCR products of; (2) CLN7 (474) NPC, (3) Control NPC, (4) CLN7 iPSC, (5) Control iPSC, (6) HEK293, (7) Shef3 ESC and (8) No-RT ran along a 2% agarose gel supplemented with GelRed at 15V for 1 hour for qualitative analysis of GLUT1 marker. Secondary image displays PCR product of RN18S1 housekeeper.

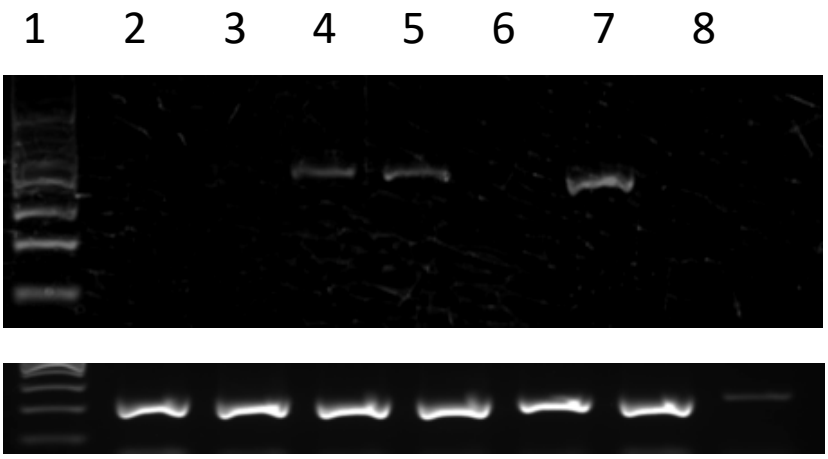

Figure depicts RT-PCR products of; (2) CLN7 (474) NPC, (3) Control NPC, (4) CLN7 iPSC, (5) Control iPSC, (6) HEK293, (7) Shef3 ESC and (8) No-RT ran along a 2% agarose gel supplemented with GelRed at 15V for 1 hour for qualitative analysis of OCT4 pluripotency marker. Secondary image displays PCR product of RN18S1 housekeeper.

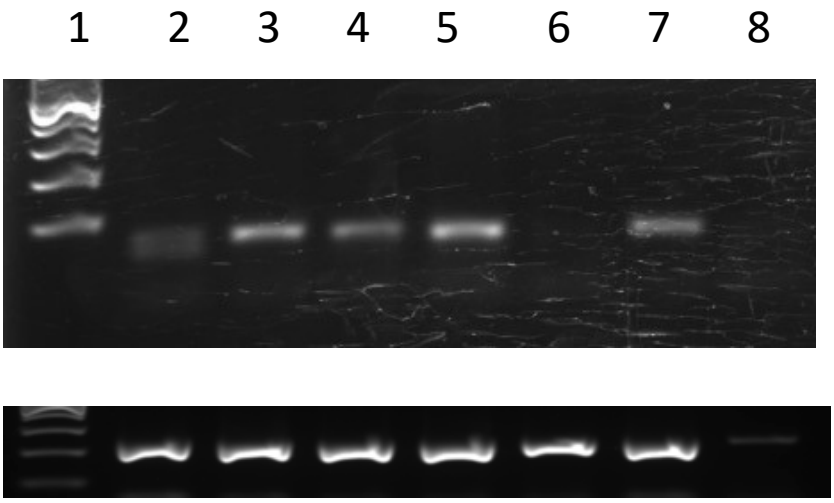

Figure depicts RT-PCR products of; (2) CLN7 (474) NPC, (3) Control NPC, (4) CLN7 iPSC, (5) Control iPSC, (6) HEK293, (7) Shef3 ESC and (8) No-RT ran along a 2% agarose gel supplemented with GelRed at 15V for 1 hour for qualitative analysis of LIN28 pluripotency marker. Secondary image displays PCR product of RN18S1 housekeeper.

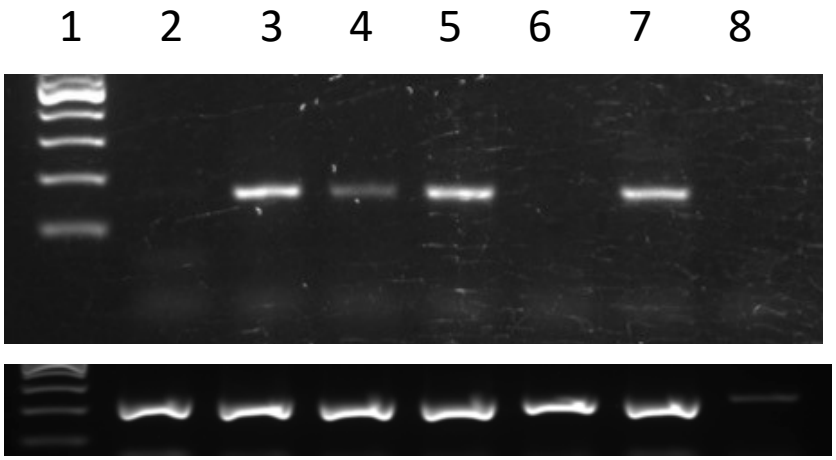

Figure depicts RT-PCR products of; (2) CLN7 (474) NPC, (3) Control NPC, (4) CLN7 iPSC, (5) Control iPSC, (6) HEK293, (7) Shef3 ESC and (8) No-RT ran along a 2% agarose gel supplemented with GelRed at 15V for 1 hour for qualitative analysis of SOX2 pluripotency marker. Secondary image displays PCR product of RN18S1 housekeeper.

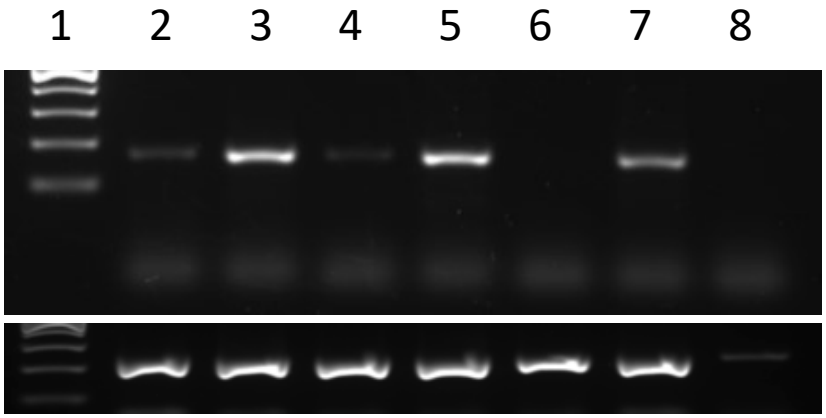

Figure depicts RT-PCR products of; (2) CLN7 (474) NPC, (3) Control NPC, (4) CLN7 iPSC, (5) Control iPSC, (6) HEK293, (7) Shef3 ESC and (8) No-RT ran along a 2% agarose gel supplemented with GelRed at 15V for 1 hour for qualitative analysis of Nanog marker. Secondary image displays PCR product of RN18S1 housekeeper.

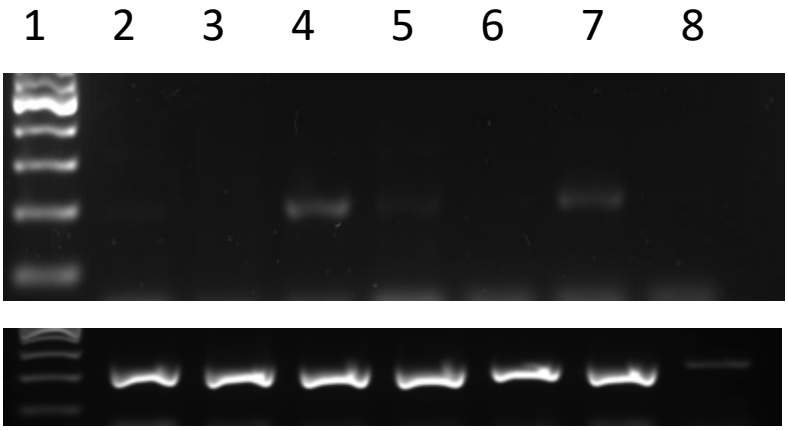

Figure depicts RT-PCR products of; (2) CLN7 (474) NPC, (3) Control NPC, (4) CLN7 iPSC, (5) Control iPSC, (6) HEK293, (7) Shef3 ESC and (8) No-RT ran along a 2% agarose gel supplemented with GelRed at 15V for 1 hour for qualitative analysis of E-cadherin marker. Secondary image displays PCR product of RN18S1 housekeeper.

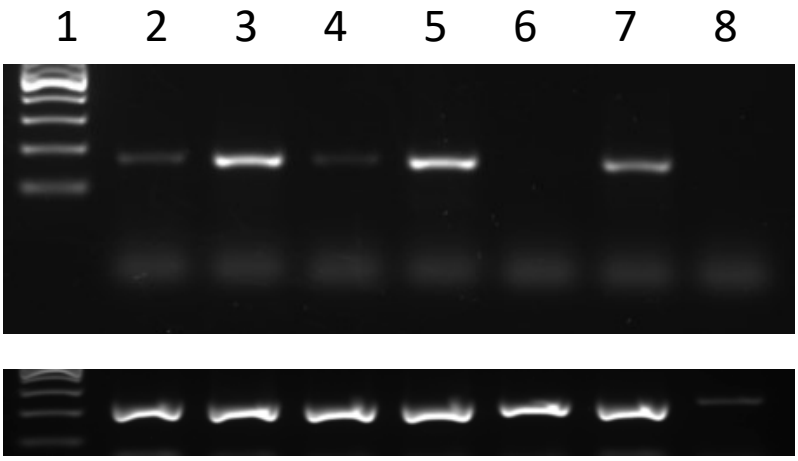

Figure depicts RT-PCR products of; (2) CLN7 (474) NPC, (3) Control NPC, (4) CLN7 iPSC, (5) Control iPSC, (6) HEK293, (7) Shef3 ESC and (8) No-RT ran along a 2% agarose gel supplemented with GelRed at 15V for 1 hour for qualitative analysis of Nestin marker. Secondary image displays PCR product of RN18S1 housekeeper.

LDHA

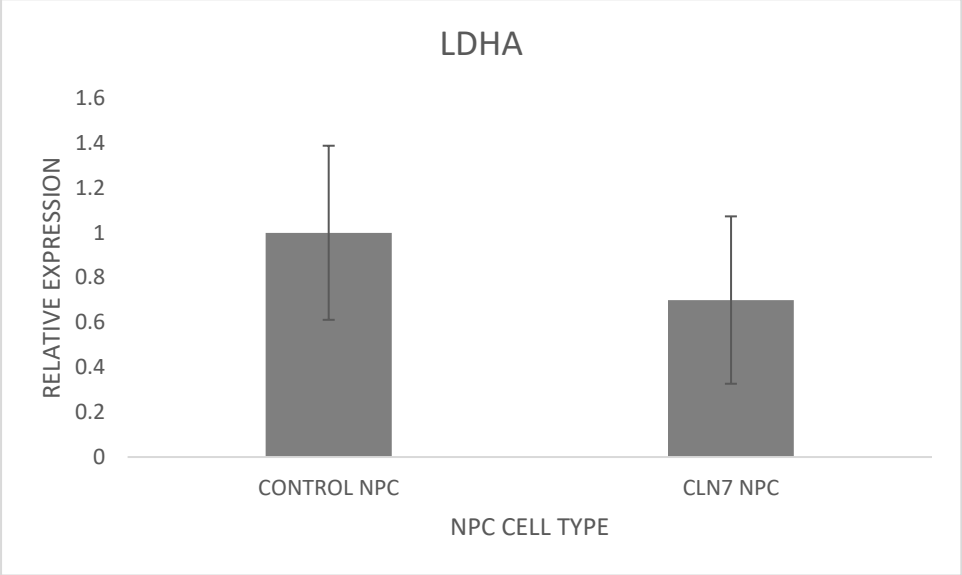

Figure 32: qPCR Analysis of LDHA in NPCs

Figure 31. Differential expression of LDHA between CLN7 neural progenitor cells (NPCs) in comparison to healthy counterpart. Relative expression was determined of CLN7 NPCs against control cell. Subsequently an Independent T-Test was performed in order to determine significance between the two cell types, in which a value of p=0.34 was obtained, displaying no significance between the two data sets. The graph depicts the relative expression of three biological repeats with each repeat also involving three technical repeats. Subsequently, error bars are calculated based on the standard error mean (SEM) of each NPC sample.

UCP2

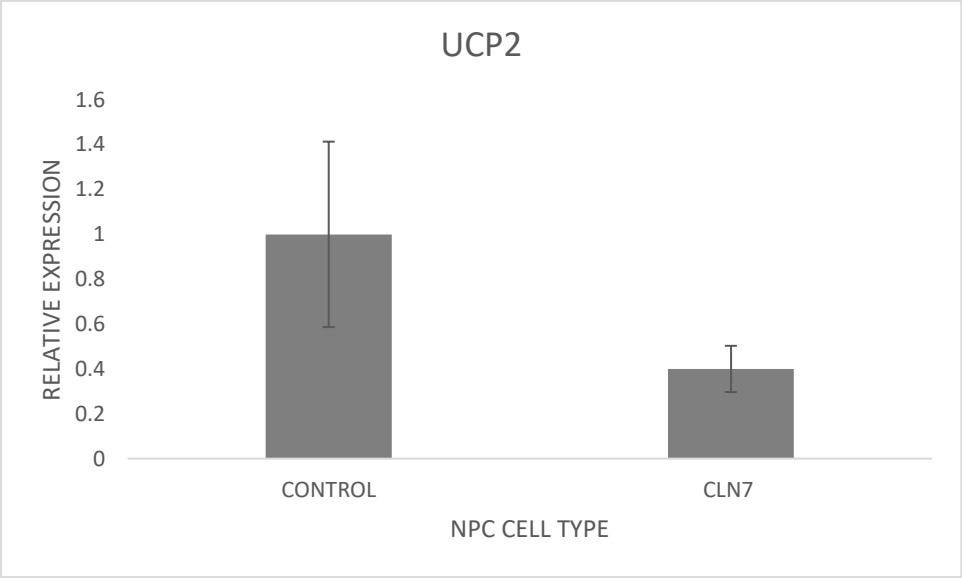

Figure 33: qPCR Analysis of UCP2 in NPCs

Figure 32. Differential expression of the metabolic stress marker, UCP2 between CLN7 neural progenitor cells (NPCs) in comparison to healthy counterpart. Relative expression was determined of CLN7 NPCs against control cell. Subsequently an Independent T-Test was performed in order to determine significance between the two cell types, in which a value of p=0.23 was obtained, displaying no significance between the two data sets. The graph depicts the relative expression of three biological repeats with each repeat also involving three technical repeats. Subsequently, error bars are calculated based on the standard error mean (SEM) of each NPC sample.

GLUT1

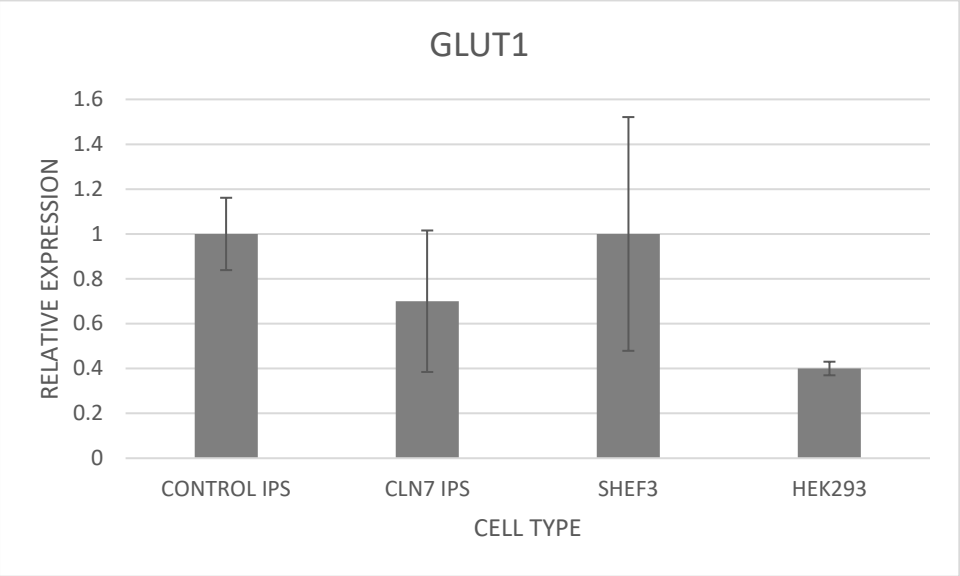

Figure 34: qPCR Analysis of GLUT1 in iPSCs

Figure 33. Differential expression of GLUT1 between CLN7 induced pluripotent stem cells in comparison to healthy counterpart control iPSC as well as Shef3 embryonic stem cells and HEK293 cells. Subsequently, single factor ANOVAs were performed with post-hoc Tukey analysis performed in order to determine statistical significance between groups. It was determined there was no statistical differences between CLN7 iPSCs and controls with a value of p=0.58 obtained, displaying no significance between the two data sets. Conversely, no statistical difference was found between control iPSCs and Shef3 with p=0.067 calculated, CLN7 to Shef3 was calculated at p=0.063 also displaying statistical significance. The graph depicts the relative expression of three biological repeats with each repeat also involving three technical repeats. Subsequently, error bars are calculated based on the standard error mean (SEM) of each iPSC sample.

SIRT1

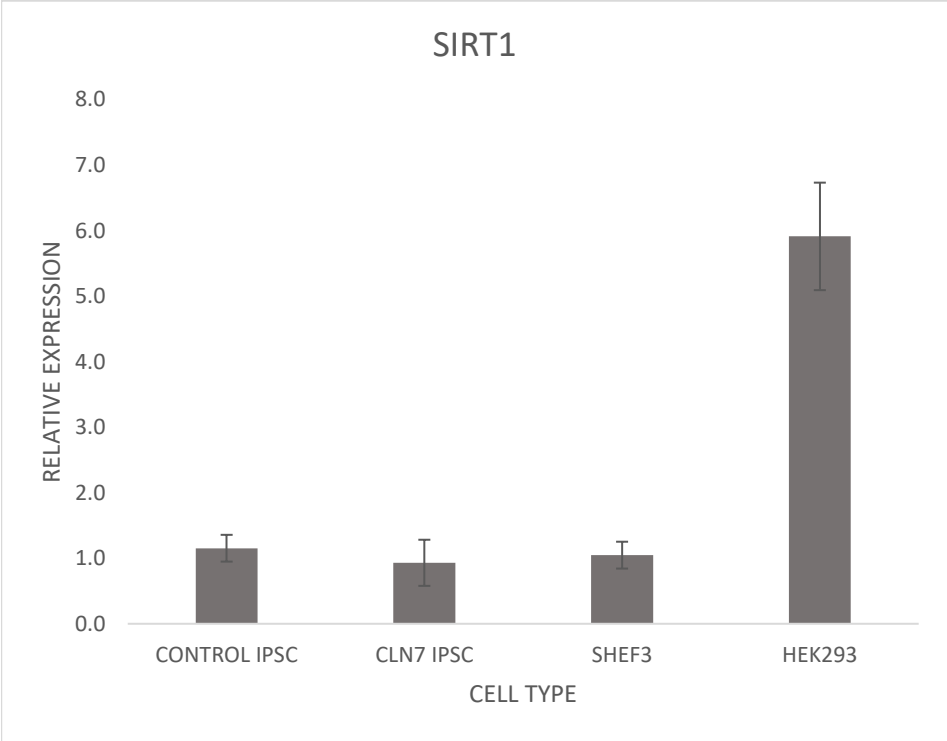

Figure 35: qPCR Analysis of SIRT1 in iPSCs

Figure 34. Differential expression of SIRT1 between CLN7 induced pluripotent stem cells in comparison to healthy counterpart control iPSC as well as Shef3 embryonic stem cells and HEK293 cells. Subsequently, single factor ANOVAs were performed with post-hoc Tukey analysis performed in order to determine statistical significance between groups. It was determined there was no statistical differences between CLN7 iPSCs and controls with a value of p=0.24 obtained, displaying no significance between the two data sets. Conversely, no statistical difference was found between control iPSCs and Shef3 with p=0.52 calculated, CLN7 to Shef3 was calculated at p=0.43 also displaying statistical significance. The graph depicts the relative expression of three biological repeats with each repeat also involving three technical repeats. Subsequently, error bars are calculated based on the standard error mean (SEM) of each iPSC sample.

7.3 Western Blot Technical Repeats

Figure 36: Western Blot Technical Repeats

Technical Repeats for p70:

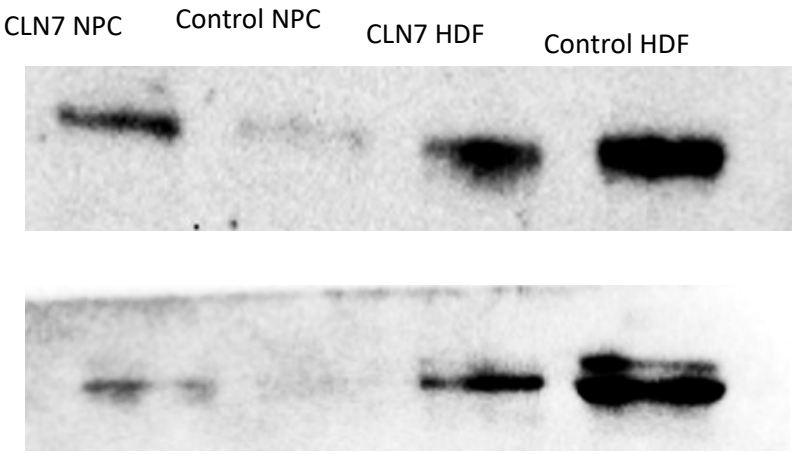

Technical Repeats for p-p70:

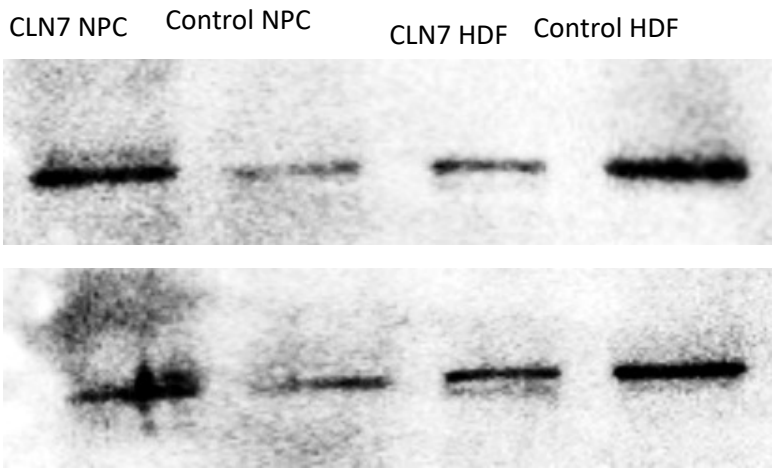

Technical Repeats for β-actin:

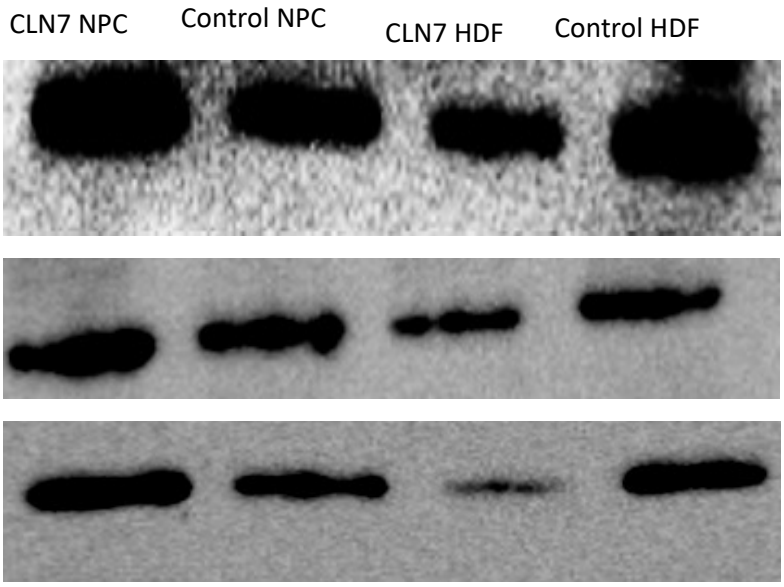

Technical Repeats for p62:

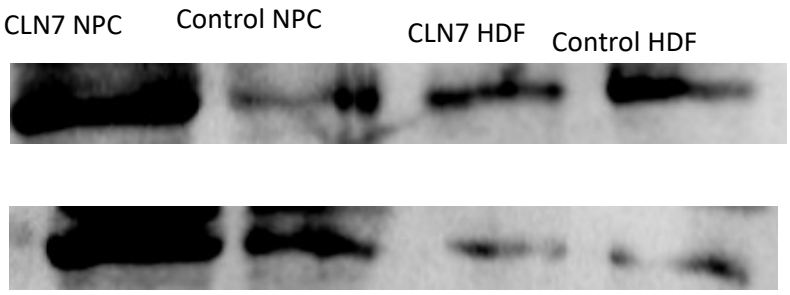

7.4 qPCR Primers

Table 21: qPCR primer set

Target	Forward Primer	Reverse Primer	Am siz
LIN28A	AGCGCAGATCAAAAGGAGACA	CCTCTCGAAAGTAGGTTGGCT	18
SOX2	GACCAGCTCGCAGACCTACAT	TGGAGTGGGAGGAAGAGGTA	15
NESTIN	GGCAGCGTTGGAACAGAG	CATCTTGAGGTGCGCCAGCT	16
NFkB1	TGCCAACAGATGGCCCATAC	TGTTCTTTTCACTAGAGCCACCA	12
HO-1	CGGGACCTGACTGACTACC	TGAAGGTAGTTTCGTGCATGC	29
PKM2	ATGTCGAAGCCCCATAGTGAA	TGGGTGGTGAATCAATGTCCA	11
UCP2	CCCCGAAGCCTCTACAATGG	CTGAGCTTGGAATCGGACCTT	21
ATP SYNTHASE	CTTGACCTTCTTTGCGGCTC	CGCACGGACAGCATCTTTG	10
GLUT1	AACTCTTCAGCCAGGGTCCAC	CACAGTGAAGATGATGAAGAC	14
LDHA	ATGGCAACTCTAAAGGATCAGC	CCAACCCCAACAACTGTAATCT	86
SIRT1	AAGTTGACTGTGAAGCTGTACG	TGCTACTGGTCTTACTTTGAGGG	21
PABC4	GCTCAGGGAAGGCCTCCAT	GAGCGCTCAGCAGCAGCAACAG	26

7.5 Supplementary Immunocytochemistry for Neuronal Cells

Figure 37: Supplementary ICC Data for Neuronal Cells

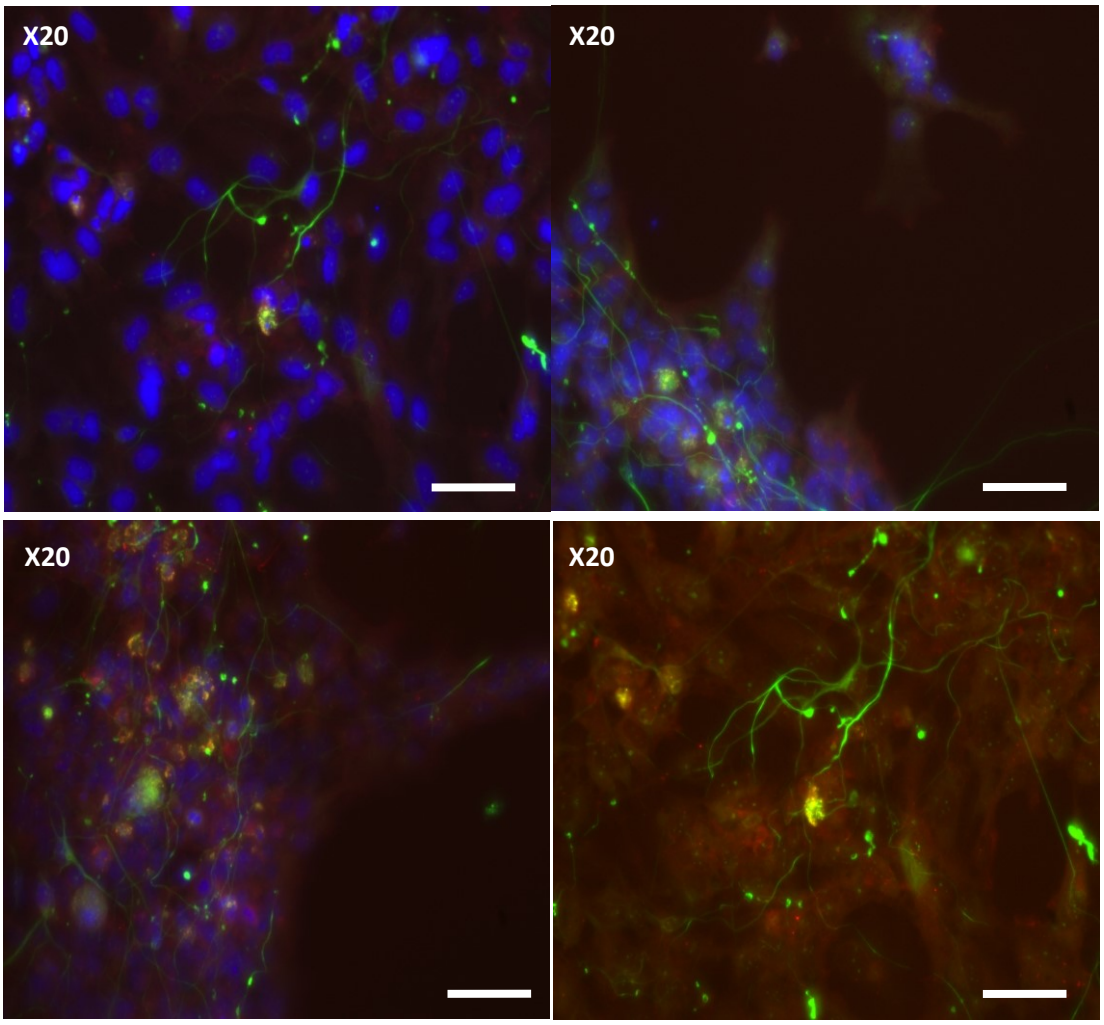

Supplementary immunocytochemistry images produced depicts CLN7 neurons developed through terminal differentiation of neural progenitor cells. Neuronal cells were incubated with LAMP1 (green) and p62 (red) primary antibody at a dilution of 1:200 for a minimum of ~12 hours at 4^{O}C, followed by the incubation of Alexa Fluor rabbit and mouse secondary antibodies, respectively. Following this, cells were also incubated with DNA stain, DAPI in order to visualize nucleus. Arrows show the accumulation of LAMP1 (green) in the axons of the neurons, whilst arrows directed towards p62 (red) display accumulation within vesicles, an indicator of impaired autophagy. Images shown at x20 magnification, whilst scale bar displayed at 100μm.

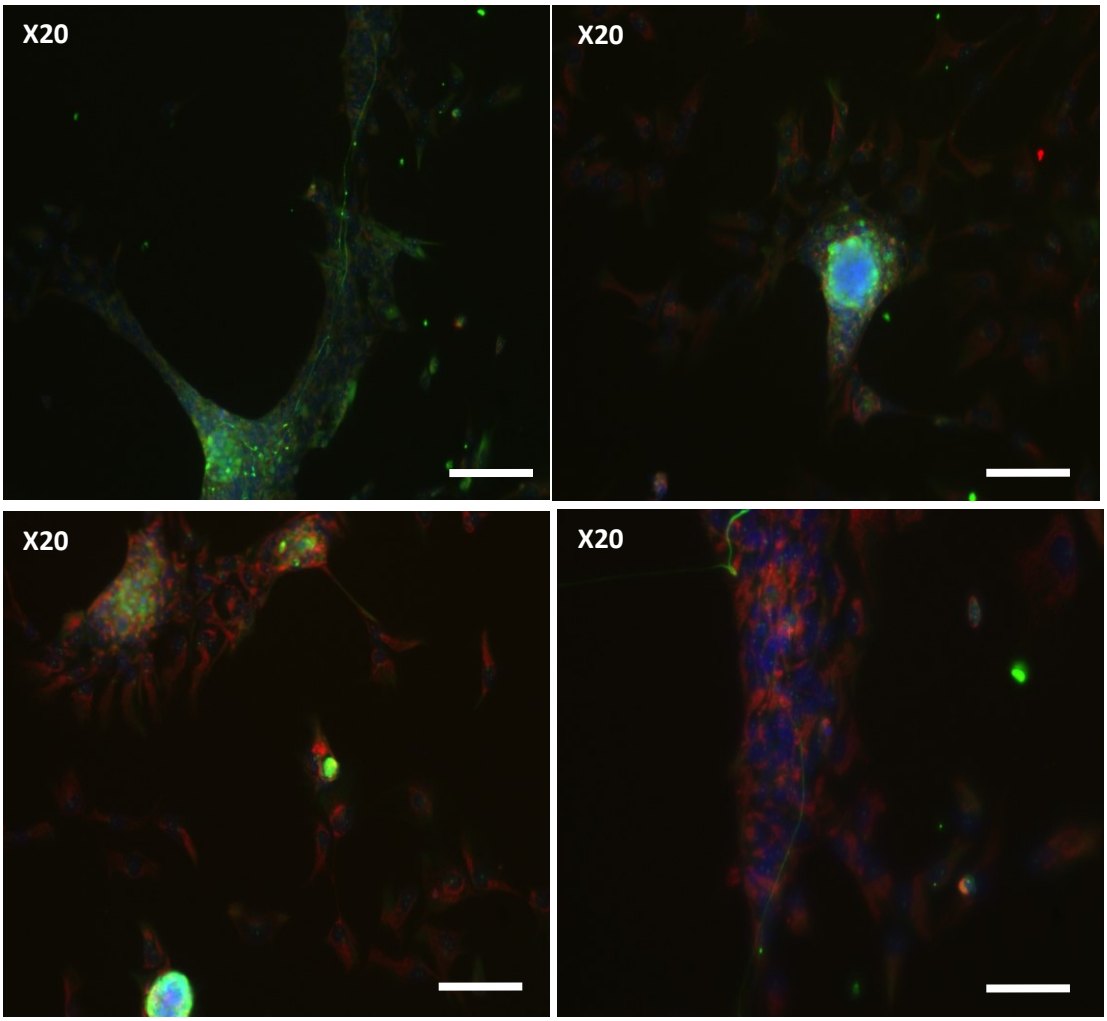

Supplementary immunocytochemistry images produced depicts CLN7 neurons developed through terminal differentiation of neural progenitor cells. Neuronal cells were incubated with LAMP1 (green) and at a dilution of 1:200 for a minimum of ~12 hours at $4^{O}C$, followed by the incubation of Alexa Fluor rabbit secondary antibody in addition to incubation of MitoTracker (red), in order to assess mitochondria utilizing mitochondrial membrane potential. Following this, cells were also incubated with DNA stain, DAPI in order to visualize nucleus. White arrows show the accumulation of LAMP1 (green) in the axons of the neurons, whilst yellow arrows directed towards MitoTracker (red) within mitochondria. Images shown at x20 magnification, whilst scale bar displayed at 100μm.

8.0 References

Aberg, L. *et al.* (1998) 'Atypical juvenile neuronal ceroid liposfuscinosis with granular osmiophilic deposit-like inclusions in the autonomic nerve cells of the gut wall', *Acta Neuropathologica*. doi: 10.1007/s004010050803.

Agilent Technologies (2017) *Agilent Seahorse XF Glycolysis Stress Test Kit*. Available at: https://www.agilent.com/cs/library/usermanuals/public/XF_Glycolysis_Stress_Test_Kit_User_Guide.pdf (Accessed: 15 April 2019).

Agilent Technologies (2019) *Seahorse XF Cell Mito Stress Test Kit*. Available at: https://www.agilent.com/cs/library/usermanuals/public/XF_Cell_Mito_Stress_Test_Kit_User_Guide.pdf (Accessed: 16 April 2019).

Aktas, O. *et al.* (2007) 'Neuronal damage in brain inflammation', *Archives of Neurology*. doi: 10.1001/archneur.64.2.185.

Anderson, G. W. *et al.* (2006) 'Diagnosis of neuronal ceroid lipofuscinosis (Batten disease) by electron microscopy in peripheral blood specimens', in *Ultrastructural Pathology*. doi: 10.1080/01913120500406566.

Bennett, M. J. and Rakheja, D. (2013) 'The neuronal ceroid-lipofuscinoses', *Developmental Disabilities Research Reviews*. doi: 10.1002/ddrr.1118.

Brandenstein, L. *et al.* (2016) 'Lysosomal dysfunction and impaired autophagy in a novel mouse model deficient for the lysosomal membrane protein Cln7', *Human Molecular Genetics*. doi: 10.1093/hmg/ddv615.

Cárcel-Trullols, J., Kovács, A. D. and Pearce, D. A. (2015) 'Cell biology of the NCL proteins: What they do and don't do', *Biochimica et Biophysica Acta - Molecular Basis of Disease*. doi: 10.1016/j.bbadis.2015.04.027.

Chan, S. H. *et al.* (2017) 'SIRT1 inhibition causes oxidative stress and inflammation in patients with coronary artery disease', *Redox Biology*. doi: 10.1016/j.redox.2017.05.027.

Chang, H. C. and Guarente, L. (2014) 'SIRT1 and other sirtuins in metabolism', *Trends in Endocrinology and Metabolism*. doi: 10.1016/j.tem.2013.12.001.

Chen, C.-T. *et al.* (2008) 'Coordinated changes of mitochondrial biogenesis and antioxidant enzymes during osteogenic differentiation of human mesenchymal stem cells', *Stem cells (Dayton, Ohio)*. doi: 10.1634/stemcells.2007-0509.

Chen, S. *et al.* (2014) 'Targeting SQSTM1/p62 Induces Cargo Loading Failure and Converts Autophagy to Apoptosis via NBK/Bik', *Molecular and Cellular Biology*, 34(18), pp. 3435–3449.

D'Aiuto, L. *et al.* (2014) 'Large-scale generation of human ipsc-derived neural stem cells/early neural progenitor cells and their neuronal differentiation', *Organogenesis*. doi: 10.1080/15476278.2015.1011921.

Danyukova, T. *et al.* (2018) 'Loss of CLN7 results in depletion of soluble lysosomal proteins and impaired mTOR reactivation', *Human Molecular Genetics*. doi: 10.1093/hmg/ddy076.

Djavaheri-Mergny, M. *et al.* (2004) 'NF-κB activation prevents apoptotic oxidative stress via an increase of both thioredoxin and MnSOD levels in TNFα-treated Ewing sarcoma cells', *FEBS Letters*. doi: 10.1016/j.febslet.2004.10.082.

Dong, G. *et al.* (2016) 'PKM2 and cancer: The function of PKM2 beyond glycolysis (Review)', *Oncology Letters*. doi: 10.3892/ol.2016.4168.

Dráberová, E. *et al.* (2008) 'Class III β-tubulin is constitutively coexpressed with glial fibrillary acidic protein and nestin in midgestational human fetal astrocytes: Implications for phenotypic identity', *Journal of Neuropathology and Experimental Neurology*. doi: 10.1097/NEN.0b013e31816a686d.

Drozd, A. M. *et al.* (2015) 'Generation of human iPSCs from cells of fibroblastic and epithelial origin by means of the oriP/EBNA-1 episomal reprogramming system', *Stem Cell Research and Therapy*. doi: 10.1186/s13287-015-0112-3.

Duran, A. *et al.* (2011) 'P62 Is a Key Regulator of Nutrient Sensing in the mTORC1 Pathway', *Molecular Cell*. doi: 10.1016/j.molcel.2011.06.038.

Eskelinen, E. L. (2006) 'Roles of LAMP-1 and LAMP-2 in lysosome biogenesis and autophagy', *Molecular Aspects of Medicine*. doi: 10.1016/j.mam.2006.08.005.

Ganley, I. G. *et al.* (2011) 'Distinct Autophagosomal-Lysosomal Fusion Mechanism Revealed by Thapsigargin-Induced Autophagy Arrest', *Molecular Cell*. doi: 10.1016/j.molcel.2011.04.024.

Ge, H. *et al.* (2015) 'Poly-L-ornithine promotes preferred differentiation of neural stem/progenitor cells via ERK signalling pathway', *Scientific Reports*. doi: 10.1038/srep15535.

Ge, H. *et al.* (2016) 'Poly-L-ornithine enhances migration of neural stem/progenitor cells via promoting α-Actinin 4 binding to actin filaments', *Scientific Reports*. doi: 10.1038/srep37681.

Geraets, R. D. *et al.* (2016) 'Moving towards effective therapeutic strategies for Neuronal Ceroid Lipofuscinosis', *Orphanet Journal of Rare Diseases*. doi: 10.1186/s13023-016-0414-2.

Getty, A. L. and Pearce, D. A. (2011) 'Interactions of the proteins of neuronal ceroid lipofuscinosis: Clues to function', *Cellular and Molecular Life Sciences*. doi: 10.1007/s00018-010-0468-6.

Gu, W. *et al.* (2016) 'Glycolytic Metabolism Plays a Functional Role in Regulating Human Pluripotent Stem Cell State', *Cell Stem Cell*. doi: 10.1016/j.stem.2016.08.008.

Han, X. *et al.* (2017) 'Efficient and Fast Differentiation of Human Neural Stem Cells from Human Embryonic Stem Cells for Cell Therapy', *Stem Cells*. Available at: https://www.ncbi.nlm.nih.gov/pmc/articles/PMC5624175/.

Hayden, M. S. and Ghosh, S. (2004) 'Signaling to NF-kappaB.', *Genes & development*. doi: 10.1101/gad.1228704.

Hendrickson, M. L. *et al.* (2011) 'Expression of nestin by neural cells in the adult rat and human brain', *PLoS ONE*. doi: 10.1371/journal.pone.0018535.

Hu, K. (2014) 'All Roads Lead to Induced Pluripotent Stem Cells: The Technologies of iPSC Generation', *Stem Cells and Development*. doi: 10.1089/scd.2013.0620.

Hüttemann, M. *et al.* (2007) 'Regulation of mitochondrial oxidative phosphorylation through cell signaling', *Biochimica et Biophysica Acta - Molecular Cell Research*. doi: 10.1016/j.bbamcr.2007.10.001.

Huynh, K. K. *et al.* (2007) 'LAMP proteins are required for fusion of lysosomes with phagosomes', *EMBO Journal*. doi: 10.1038/sj.emboj.7601511.

Inoue, S.-I. *et al.* (2010) 'Mitochondrial respiration defects modulate differentiation but not proliferation of hematopoietic stem and progenitor cells', *FEBS Letters*. doi: 10.1016/j.febslet.2010.06.036.

Ito, K. and Suda, T. (2014) 'Metabolic requirements for the maintenance of self-renewing stem cells', *Nature Reviews Molecular Cell Biology*. doi: 10.1038/nrm3772.

Ivanov, A. I. *et al.* (2014) 'Glycolysis and oxidative phosphorylation in neurons and astrocytes during network activity in hippocampal slices', *Journal of Cerebral Blood Flow and Metabolism*. doi: 10.1038/jcbfm.2013.222.

Jin, L. *et al.* (2017) 'Phosphorylation-mediated activation of LDHA promotes cancer cell invasion and tumour metastasis', *Oncogene*. doi: 10.1038/onc.2017.6.

Johansen, T. and Lamark, T. (2011) 'Selective autophagy mediated by autophagic adapter proteins', *Autophagy*. doi: 10.4161/auto.7.3.14487.

Jonckheere, A. I., Smeitink, J. A. M. and Rodenburg, R. J. T. (2012) 'Mitochondrial ATP synthase: Architecture, function and pathology', *Journal of Inherited Metabolic Disease*. doi: 10.1007/s10545-011-9382-9.

Junge, W. and Nelson, N. (2015) 'ATP Synthase', *Annual Review of Biochemistry*. doi: 10.1146/annurev-biochem-060614-034124.

Junying, Y. *et al.* (2009) 'Human induced pluripotent stem cells free of vector and transgene sequences', *Science*. doi: 10.1126/science.1172482.

Kairisalo, M. *et al.* (2007) 'X-linked inhibitor of apoptosis protein increases mitochondrial antioxidants through NF-κB activation', *Biochemical and Biophysical Research Communications*. doi: 10.1016/j.bbrc.2007.09.115.

Katsetos, C. D. *et al.* (2003) 'Class III β-tubulin isotype: A key cytoskeletal protein at the crossroads of developmental neurobiology and tumor neuropathology', *Journal of Child Neurology*. doi: 10.1177/088307380301801205.

Katsuragi, Y., Ichimura, Y. and Komatsu, M. (2015) 'p62/SQSTM1 functions as a signalling hub and an autophagy adaptor', *FEBS Journal*, 282(24), pp. 4672–4678.

Kim, G. H. *et al.* (2015) 'The Role of Oxidative Stress in Neurodegenerative Diseases', *Experimental Neurobiology*. doi: 10.5607/en.2015.24.4.325.

Kollmann, K. *et al.* (2013) 'Cell biology and function of neuronal ceroid lipofuscinosis-related proteins', *Biochimica et Biophysica Acta - Molecular Basis of Disease*. doi: 10.1016/j.bbadis.2013.01.019.

Kondoh, H. *et al.* (2007) 'Protection from oxidative stress by enhanced glycolysis; a possible mechanism of cellular immortalization', *Histology and Histopathology*.

Koopman, W. J. H. *et al.* (2013) 'OXPHOS mutations and neurodegeneration', *EMBO Journal*. doi: 10.1038/emboj.2012.300.

Kousi, M. *et al.* (2009) 'Mutations in CLN7/MFSD8 are a common cause of variant late-infantile neuronal ceroid lipofuscinosis', *A Journal of Neurology*, 132(3), pp. 810–819.

Laplante, M. and Sabatini, D. M. (2012) 'MTOR signaling in growth control and disease', *Cell*. doi: 10.1016/j.cell.2012.03.017.

Lawrence, T. (2009) 'The nuclear factor NF-kappaB pathway in inflammation.', *Cold Spring Harbor perspectives in biology*. doi: 10.1101/cshperspect.a001651.

Levine, B. and Kroemer, G. (2008) 'Autophagy in the Pathogenesis of Disease', *Cell*. doi: 10.1016/j.cell.2007.12.018.

Liemburg-Apers, D. C. *et al.* (2015) 'Interactions between mitochondrial reactive oxygen species and cellular glucose metabolism', *Archives of Toxicology*. doi: 10.1007/s00204-015-1520-y.

Lingappan, K. (2018) 'NF-κB in oxidative stress', *Current Opinion in Toxicology*. doi: 10.1016/j.cotox.2017.11.002.

Liu, T. *et al.* (2017) 'NF-κB signaling in inflammation', *Signal Transduction and Targeted Therapy*. doi: 10.1038/sigtrans.2017.23.

Liu, W. J. *et al.* (2016) 'p62 links the autophagy pathway and the ubiqutin-proteasome system

upon ubiquitinated protein degradation', *Cellular and Molecular Biology Letters*. doi: 10.1186/s11658-016-0031-z.

Lunt, S. Y. and Vander Heiden, M. G. (2011) 'Aerobic Glycolysis: Meeting the Metabolic Requirements of Cell Proliferation', *Annual Review of Cell and Developmental Biology*. doi: 10.1146/annurev-cellbio-092910-154237.

Magnuson, B., Ekim, B. and Fingar, D. C. (2012) 'Regulation and function of ribosomal protein S6 kinase (S6K) within mTOR signalling networks.', *The Biochemical Journal*. doi: 10.1042/BJ20110892.

Malik, N. and Rao, M. S. (2013) 'A review of the methods for human iPSC derivation', in *Methods in Molecular Biology*. doi: 10.1007/978-1-62703-348-0_3.

Menon, S. *et al.* (2016) 'An overview of direct somatic reprogramming: The ins and outs of iPSCs', *International Journal of Molecular Sciences*. doi: 10.3390/ijms17010141.

Mohammed, A. *et al.* (2017) 'in vivo localization of the neuronal ceroid lipofuscinosis proteins, CLN3 and CLN7, at endogenous expression levels', *Neurobiology of Disease*. doi: 10.1016/j.nbd.2017.03.015.

Morgan, M. J. and Liu, Z. G. (2011) 'Crosstalk of reactive oxygen species and NF-κB signaling', *Cell Research*. doi: 10.1038/cr.2010.178.

Natunen, S. *et al.* (2011) 'The binding specificity of the marker antibodies Tra-1-60 and Tra-1-81 reveals a novel pluripotency-associated type 1 lactosamine epitope', *Glycobiology*. doi: 10.1093/glycob/cwq209.

Ou, X. *et al.* (2014) 'SIRT1 positively regulates autophagy and mitochondria function in embryonic stem cells under oxidative stress', *Stem Cells*. doi: 10.1002/stem.1641.

Pattappa, G. *et al.* (2013) 'Continuous and Uninterrupted Oxygen Tension Influences the Colony Formation and Oxidative Metabolism of Human Mesenchymal Stem Cells', *Tissue Engineering Part C: Methods*. doi: 10.1089/ten.tec.2011.0734.

Quistgaard, E. M. *et al.* (2016) 'Understanding transport by the major facilitator superfamily (MFS): Structures pave the way', *Nature Reviews Molecular Cell Biology*. doi: 10.1038/nrm.2015.25.

Rakheja, D. and Bennett, M. J. (2018) 'Neuronal ceroid-lipofuscinosis', *Translational Science of Rare Diseases*, 3(2), pp. 83–95.

Saier, M. H. *et al.* (1999) 'The major facilitator superfamily.', *J. Mol. Microbiol. Biotechnol.* doi: 10.1002/14651858.CD003747.pub2.Heparin.

Salminen, A., Kaarniranta, K. and Kauppinen, A. (2013) 'Crosstalk between oxidative stress and SIRT1: Impact on the aging process', *International Journal of Molecular Sciences*. doi: 10.3390/ijms14023834.

Schieber, M. and Chandel, N. S. (2014) 'ROS function in redox signaling and oxidative stress', *Current Biology*. doi: 10.1016/j.cub.2014.03.034.

Sharifi, A. *et al.* (2010) 'Expression and lysosomal targeting of CLN7, a major facilitator superfamily transporter associated with variant late-infantile neuronal ceroid lipofuscinosis', *Human Molecular Genetics*. doi: 10.1093/hmg/ddq381.

Siintola, E. *et al.* (2007) 'The Novel Neuronal Ceroid Lipofuscinosis Gene MFSD8 Encodes a Putative Lysosomal Transporter', *The American Journal of Human Genetics*. doi: 10.1086/518902.

Simsek, T. *et al.* (2010) 'The distinct metabolic profile of hematopoietic stem cells reflects their location in a hypoxic niche', *Cell Stem Cell*. doi: 10.1016/j.stem.2010.07.011.

Sreedhar, A. *et al.* (2017) 'UCP2 overexpression enhanced glycolysis via activation of PFKFB2 during skin cell transformation', *Oncotarget*. doi: 10.18632/oncotarget.20762.

Sridharan, R. and Plath, K. (2008) 'Illuminating the Black Box of Reprogramming', *Cell Stem Cell*. doi: 10.1016/j.stem.2008.03.015.

Steenhuis, P. *et al.* (2010) 'Lysosomal targeting of the CLN7 membrane glycoprotein and transport via the plasma membrane require a dileucine motif', *Traffic*. doi: 10.1111/j.1600-0854.2010.01073.x.

Stepanenko, A. A. and Dmitrenko, V. V. (2015) 'HEK293 in cell biology and cancer research: Phenotype, karyotype, tumorigenicity, and stress-induced genome-phenotype evolution', *Gene*. doi: 10.1016/j.gene.2015.05.065.

Takahashi, K. *et al.* (2007) 'Induction of Pluripotent Stem Cells from Adult Human Fibroblasts by Defined Factors', *Cell*. doi: 10.1016/j.cell.2007.11.019.

Takahashi, K. *et al.* (2014) 'Induction of pluripotency in human somatic cells via a transient state resembling primitive streak-like mesendoderm', *Nature Communications*. doi: 10.1038/ncomms4678.

Takubo, K. *et al.* (2013) 'Regulation of glycolysis by Pdk functions as a metabolic checkpoint for cell cycle quiescence in hematopoietic stem cells', *Cell Stem Cell*. doi: 10.1016/j.stem.2012.10.011.

Tang, Y., Yu, P. and Cheng, L. (2017) 'Current progress in the derivation & therapeutic application of neural stem cells', *Cell Death and Disease*. doi: 10.1038/cddis.2017.504.

Thelen, M. *et al.* (2012) 'Disruption of the autophagy-lysosome pathway is involved in neuropathology of the nclf mouse model of neuronal ceroid lipofuscinosis', *PLoS ONE*. doi: 10.1371/journal.pone.0035493.

Vallabhapurapu, S. and Karin, M. (2009) 'Regulation and Function of NF-κB Transcription Factors in the Immune System', *Annual Review of Immunology*. doi: 10.1146/annurev.immunol.021908.132641.

Wang, L. *et al.* (2013) 'LC3 fluorescent puncta in autophagosomes or in protein aggregates can be distinguished by FRAP analysis in living cells', *Autophagy*. doi: 10.4161/auto.23814.

Xiao, H. *et al.* (2018) 'GLUT1 regulates cell glycolysis and proliferation in prostate cancer', *Prostate*. doi: 10.1002/pros.23448.

Xiao, L. *et al.* (2009) 'The role of mTOR and phospho-p70S6K in pathogenesis and progression of gastric carcinomas: An immunohistochemical study on tissue microarray', *Journal of Experimental and Clinical Cancer Research*. doi: 10.1186/1756-9966-28-152.

Zeineddine, D. *et al.* (2014) 'The Oct4 protein: more than a magic stemness marker', *Am J Stem Cells*.

Zhang, J. *et al.* (2016) 'LIN28 Regulates Stem Cell Metabolism and Conversion to Primed Pluripotency', *Cell Stem Cell*. doi: 10.1016/j.stem.2016.05.009.

Zhang, S. (2014) 'Sox2, a key factor in the regulation of pluripotency and neural differentiation', *World Journal of Stem Cells*. doi: 10.4252/wjsc.v6.i3.305.

Zhang, W. *et al.* (2017) 'Sirt1 Inhibits Oxidative Stress in Vascular Endothelial Cells', *Oxidative Medicine and Cellular Longevity*. doi: 10.1155/2017/7543973.

Zhao, X. and Moore, D. (2018) 'Neural stem cells: developmental mechanisms and disease modeling', *Cell and Tissue Research*, 371(1), pp. 1–6.